THE CHEMICAL AND MECHANICAL BEHAVIORS OF

POLYMER / REACTIVE METAL SYSTEMS UNDER HIGH STRAIN RATES

A Dissertation
Presented to
The Academic Faculty

By

Yubin Shen

In Partial Fulfillment
of the Requirements for the Degree
Doctor of Philosophy in
Polymer, Textile and Fiber Engineering

School of Polymer, Textile and Fiber Engineering
Georgia Institute of Technology
December 2012

THE CHEMICAL AND MECHANICAL BEHAVIORS OF

POLYMER / REACTIVE METAL SYSTEMS UNDER HIGH STRAIN RATES

Approved by:

Dr. Karl I. Jacob, Advisor
School of Material Science and Engineering
Georgia Institute of Technology

Dr. Donggang Yao
School of Material Science and Engineering
Georgia Institute of Technology

Dr. Fred L. Cook, Co-advisor
School of Material Science and Engineering
Georgia Institute of Technology

Dr. Arun M. Gokhale
School of Material Science and Engineering
Georgia Institute of Technology

Dr. Naresh N. Thadhani,
Co-advisor
School of Material Science and Engineering
Georgia Institute of Technology

Date Approved: 07/17/2012

To my lost youth.

ACKNOWLEDGEMENTS

My seven years' Ph.D. program has been the longest single period of time I have spent during my academic career, yet it has been worth it not only because of the tiny achievements I have obtained or the knowledge I have gained, but more importantly, the concepts I have gained through my personal experience: the progress of studies comes from hard work, and is retarded by frivolities; wise decisions are made after thorough consideration, and destroyed by random ones.

The completion of this work contains a lot of guidance and support from professors, friends and family members, to whom I would like to express my sincere appreciation: I express my gratitude to my principle thesis advisor, Dr. Karl Jacob, for providing me the great opportunity to take part in this interesting project and the flexible research environment for me to explore unknowns. I am thankful to his invaluable advice, guidance, and constant support in my research. I also thank Dr. Naresh Thadhani for access to the High-Strain-Rate Laboratory to conduct experiments that formed the main part of this thesis work. I have learned a great deal from my many discussions with him. I also thank my other committee members, Dr. Fred Cook, Dr. Donggang Yao and Dr. Arun Gokhale, for their precious suggestions and feedback.

In addition, I am also grateful to Dr. Siwei Du for providing me training on the Taylor impact test, and to Dr. Jiyun Yang for helping with the set up and analysis on the SHPB test.

I am also thankful to my former and current group members, my friends and classmates, research scientists who have trained me with test instruments, professors and

staff members in the former PTFE department, for their direct or indirect help both academically and philosophically during my Ph.D. study.

Finally, my deepest thanks and love extend to my parents, parents-in law, and especially my husband, Qing Lan, for their trust and unselfish support in my life.

TABLE OF CONTENTS

DEDICATION.....I

ACKNOWLEDGEMENTS.....II

LIST OF TABLES.....IX

LIST OF FIGURES.....X

LIST OF SYMBOLS AND ABBREVATIONS.....XVIII

SUMMARY.....XXI

CHAPTERS

I. INTRODUCTION.....1

1.1 Motivation and Objectives.....1

1.2 Scope of Study.....3

II. BACKGROUND.....5

2.1 Fundamentals of Wave Propagation.....5

2.1.1 Elastic Wave and Plastic Wave.....5

2.1.2 Shock Wave.....6

2.2 High Strain Rate Measurement.....9

2.2.1 Split Hopkinson Bar Test.....10

2.2.2 Taylor Impact Test.....13

2.2.3 Plate Impact Test.....16

2.3 Mechanical Responses of Polymers Under High Strain Rates.....17

2.3.1 Mechanical Behaviors of Different Polymers Under High Strain Rates 18

2.3.2 Explanations for the Mechanical Behaviors of Polymers Under High Strain Rates....21

2.4 Shock-Initiated Transformation....23

2.4.1 Shock-Initiated Phase Transformation....23

2.4.2 Shock-Initiated Chemical Reaction....25

2.5 Constitutive Models for Polymers Under High Strain Rates....28

2.5.1 Hutchings Model....29

2.5.2 Johnson-Cook Model....30

2.5.3 Zerilli-Armstrong Model....32

2.5.4 Mulliken and Boyce Model....33

2.5.5 Modified Johnson-Cook Model....34

III. POLYTETRAFLUOROETHYLENE (PTFE) 7A / TITANIUM (TI) COMPOSITE SYSTEM....36

3.1 Materials....36

3.2 Fabrication and Processing of PTFE 7A / Ti Composite....37

3.3 PTFE 7A / Ti Composite Configurations....39

3.4 Characterization of PTFE 7A / Ti Composite....45

3.4.1 Thermal Analyses....45

3.4.2 XRD Identification After Heating....47

3.4.3 Quasi-Static Compression Test....51

3.4.4 SHPB Test....53

3.4.5 Post-SHPB Characterization by XRD Analysis....55

3.5 Summary....57

IV. EXPERIMENTAL INVESTIGATION OF TAYLOR IMPACT TEST ON PTFE 7A / TI COMPOISTE.....59

4.1 Overview.....59

4.2 Experimental.....60

4.3 Results and Discussion.....61

4.3.1 PTFE 7A (51 wt%) / Ti (49 wt%) Composite (Batch #1) with Non-Uniform Distribution.....63

4.3.1.1 Medium Dimension Samples.....63

4.3.1.2 Small and Even Smaller Dimension Samples.....67

4.3.2 PTFE 7A (51 wt%) / Ti (49 wt%) Composite (Batch #2) with Uniform Distribution.....69

4.3.2.1 Medium Dimension Samples.....69

4.3.2.2 Small and Even Smaller Dimension Samples.....74

4.3.2.3 Large Dimension Samples.....76

4.3.3 PTFE 7A (32.4 wt%) / Ti (67.6 wt%) Composite (Batch #3) with Equal Volume Composition.....78

4.3.3.1 Medium Dimension Samples.....79

4.3.3.2 Small and Even Smaller Dimension Samples.....82

4.3.3.3 Large Dimension Samples.....84

4.3.4 Film reduction (House Method) Analysis.....87

4.3.4.1 House Method.....87

4.3.4.2 Film Reduction Analysis on Large Dimension Samples.....89

4.3.5 Comparison of Taylor Impact Test Results on PTFE 7A / Ti with Different Impact Velocities, Sample Dimensions and Sample Configurations.....99

4.3.5.1 Impact-Initiated Reaction.....99

4.3.5.2 The Effect of Impact Velocity on the Impact-Initiated Reaction 102

4.3.5.3 The Effect of Sample Dimension on the Impact-Initiated Reaction.....103

4.3.5.4 The Effect of Sample Configuration on the Impact-Initiated Reaction.....105

4.4 Summary.....109

V. COMPUTATIONAL ANALYSIS OF TAYLOR IMPACT TEST ON PTFE 7A / TI COMPOISTE.....110

5.1 Constitutive Modeling.....110

5.2 Results and Analysis.....118

5.2.1 Simulation Results of Large Dimension Samples.....118

5.2.2 Discussions.....133

5.3 Summary.....135

VI. MICROSTRUCTURAL COMPUTATIONAL ANALYSIS OF THE EFFECT OF CONFIGURATION ON PTFE 7A / TI IMPACT-INITIATED REACTION.....136

6.1 Overview.....136

6.2 Approach.....136

6.3 Constitutive Models and Input Parameters.....139

6.4 Results and Analysis.....141

6.4.1 Simulation Results of Batch #1 Sample.....142

6.4.2 Simulation Results of Batch #2 Sample.....146

6.4.3 Simulation Results of Batch #3 Sample.....149

6.4.4 Discussions.....152

6.5 Summary.....156

VII. CONCLUSIONS.....158

7.1 Summary of Work.....158

7.2 Work Significance.....161

7.3 Recommendations for Future Work.....162

APPENDIX A.....164

APPENDIX B.....169

APPENDIX C.....173

REFERENCES.....177

LIST OF TABLES

2.1 A comparison between shock-induced and shock-assisted chemical reaction.....26

3.1 Typical property data for Teflon® PTFE 7A.....37

3.2 Typical property data for Titanium powders.....37

3.3 Sample sizes of four different dimensions.....38

3.4 Density and %TMD of the PTFE 7A / Ti composite in three batches.....38

3.5 The lattice parameters of the PTFE 7A / Ti composite reaction product after heating at different heating rates.....50

4.1 Summary of the Taylor impact test results.....62

4.2 Comparison of the reactivity and critical axial / areal strains among three batches of PTFE 7A / Ti composite (medium dimensions) at 200 m/s and 300 m/s impact velocities.....107

5.1 Constants obtained from the SHPB test at the strain rate around 2500 s^{-1}.....112

5.2 Constants obtained from the Instron test at the strain rate of 0.01 s^{-1}.....113

5.3 Parameters in the modified Johnson-Cook model for the PTFE 7A / Ti composite.....114

5.4 Input material parameters for the PTFE 7A / Ti composite.....118

5.5 Input sample dimensions for the PTFE 7A / Ti composite from Batch #2, large dimension.....118

6.1 Input material parameters for PTFE 7A.....139

6.2 Input material parameters for Ti.....140

6.3 Input material parameters for the Copper projectile.....141

6.4 Material constants of the Johnson-Cook constitutive model for the Copper projectile.....141

6.5 Model setups for the PTFE 7A / Ti microstructural simulation.....142

LIST OF FIGURES

2.1 A schematic illustration of $P - V$ Hogoniot curve for solid and porous materials.....8

2.2 Hugoniot data (a) U_p *vs.* U_s and (b) V/V_0 *vs.* P for polystyrene.....9

2.3 A schematic illustration of the main parts in the SHPB test.....10

2.4 The stress *vs.* strain curves of the PTFE 7A sample at the strain rate of 2250 s^{-1} extracted from the SHPB test.....12

2.5 The detailed schematic view of plastic and elastic wave propagation during the Taylor impact test.....14

2.6 The calculation results and experimental data of $\frac{L_1}{L}$ $(and\ \frac{L_1-X}{L})$ *vs.* $\frac{\rho U^2}{\sigma_{yd}}$ for steel from Taylor impact test.....15

2.7 A schematic diagram of the plate impact test.....17

2.8 Maximum stress *vs.* strain rate at 21 ℃ for polycarbonate.....19

2.9 Flow stress at 5% strain *vs.* strain rate for PEEK and Nylatron.....20

2.10 Flow stress at 10% strain *vs.* strain rate for polyethylene.....20

2.11 (a) PTFE crystalline phase transition behaviors under different temperature and pressure conditions; (b) stress *vs.* strain curves of PTFE at compression and tension modes.....24

2.12 Maxwell-Weichert model description with linear viscoelasticity plus thermal activation non-linear viscoplasticity.....33

2.13 One-dimensional interpretation of the Mulliken and Boyce constitutive model.....34

3.1 SEM images of Ti and PTFE 7A powders after pressing and PTFE 7A / Ti composite from three batches.....40

3.2 DTA curves of PTFE 7A and PTFE 7A / Ti composite at three different heating rates (2 ℃/min, 10 ℃/min, and 50 ℃/min).....45

3.3 XRD patterns of PTFE 7A / Ti composite collected after DTA test at three different heating rates (2 ℃/min, 10 ℃/min, and 50 ℃/min).....47

3.4 The crystal structure of TiC_x and the variation of the lattice parameter of TiC_x with stoichiometry.....49

3.5 Stress *vs.*strain curves obtained from Instron test for PTFE 7A and PTFE 7A / Ti composite with strain rate ranging from 0.0001 to 0.1 s^{-1} (Batch #2).....51

3.6 The experimental setup for SHPB test in compression mode.....53

3.7 Stress *vs.* strain curves obtained from the SHPB test for PTFE 7A, PTFE 7A / Ti composite and comparison plots for the two systems at the strain rate of ~ 3100 s^{-1} 54

3.8 XRD analyses of post-SHPB samples for PTFE 7A and PTFE 7A / Ti composite under different compression pressures.....56

4.1 Schematic diagram of the Taylor impact test setup.....60

4.2 Consecutive images of the Taylor impact test on PTFE 7A / Ti composite (Batch #1, medium size), V_i = 308 m/s, the exposure time t_{exp} = 500 ns, and the interframe time t_{int} = 2 μs.....64

4.3 Consecutive images of the Taylor impact test on PTFE 7A / Ti composite (Batch #1, medium size), V_i = 188.73m/s, t_{exp} = 500ns, and t_{int} = 2 μs.....64

4.4 Consecutive images of the Taylor impact test on PTFE 7A / Ti composite (Batch #1, medium size), V_i = 135.1m/s, t_{exp} = 500ns, and t_{int} = 2 μs.....64

4.5 Consecutive images of the Taylor impact test on PTFE 7A / Ti composite (Batch #1, medium size), V_i = 117.94m/s, t_{exp} = 500ns, and t_{int} = 2.5 μs (first 13 frames), t_{int} = 3 μs(last 3 frames).....65

4.6 Axial strain and areal strain *vs.* image sequence of the PTFE 7A / Ti composite (Batch #1) under four different impact velocities.....66

4.7 Ignition time *vs.* kinetic energy based on Taylor impact test at five different impact velocities (Batch #1).....67

4.8 Consecutive images of Taylor impact test on the PTFE 7A / Ti composite (Batch #1, small size), V_i=309.2m/s, t_{exp}=500ns, and t_{int}=1.5 μs.....68

4.9 Consecutive images of Taylor impact test on the PTFE 7A / Ti composite (Batch #1, even smaller size), V_i=~300m/s, t_{exp}=500ns, and t_{int}=1.5 μs.....68

4.10 Consecutive images of Taylor impact test on the PTFE 7A / Ti composite (Batch #2, medium size), V_i=395.5m/s, t_{exp}=500ns, and t_{int}=1 μs.....69

4.11 Consecutive images of Taylor impact test on the PTFE 7A / Ti composite (Batch #2, medium size), V_i = 304.41 m/s, t_{exp} = 500 ns, and t_{int} = 1.5 μs.....70

4.12 Consecutive images of Taylor impact test on PTFE 7A / Ti composite (Batch #2, medium size), V_i=200.96m/s, t_{exp}=500ns, and t_{int}=1.75 μs.....70

4.13 Consecutive images of Taylor impact test on PTFE 7A / Ti composite (Batch #2, medium size), V_i=100.17m/s, t_{exp}=500ns, and t_{int}=2.5 μs.....70

4.14 Axial strain and areal strain *vs.* image sequence of PTFE 7A / Ti composite (Batch #2) under three different impact velocities.....72

4.15 Ignition time *vs.* kinetic energy based on Taylor impact test at three different impact velocities (Batch #2).....73

4.16 Consecutive images of Taylor impact test on PTFE 7A / Ti composite (Batch #2, small size), V_i=198.67m/s, t_{exp}=500ns, and t_{int}=1.75 μs.....74

4.17 Consecutive images of Taylor impact test on PTFE 7A / Ti composite (Batch #2, small size), V_i=99.44m/s, t_{exp}=500ns, and t_{int}=2.5 μs.....74

4.18 Consecutive images of Taylor impact test on PTFE 7A / Ti composite (Batch #2, even smaller size), V_i=203.04m/s, t_{exp}=500ns, and t_{int}=1.75 μs.....75

4.19 Consecutive images of Taylor impact test on PTFE 7A / Ti composite (Batch #2, even smaller size), V_i=101.68m/s, t_{exp}=500ns, and t_{int}=2.5 μs.....75

4.20 Consecutive images of Taylor impact test on PTFE 7A / Ti composite (Batch #2, large size), V_i=495.61m/s, t_{exp}=500ns, and t_{int}=1 μs.....76

4.21 Consecutive images of Taylor impact test on PTFE 7A / Ti composite (Batch #2, large size), V_i=406.44m/s, t_{exp}=500ns, and t_{int}=2 μs.....76

4.22 Consecutive images of Taylor impact test on PTFE 7A / Ti composite (Batch #2, large size), V_i=282.56m/s, t_{exp}=500ns, and t_{int}=1.5 μs.....77

4.23 Consecutive images of Taylor impact test on PTFE 7A / Ti composite (Batch #2, large size), V_i=201.01m/s, t_{exp}=500ns, and t_{int}=1.5 μs.....77

4.24 Consecutive images of Taylor impact test on PTFE 7A / Ti composite (Batch #2, large size), V_i=112.38m/s, t_{exp}=500ns, and t_{int}=2 μs.....77

4.25 Consecutive images of Taylor impact test on PTFE 7A / Ti composite (Batch #3, medium size), V_i=408.44m/s, t_{exp}=500ns, and t_{int}=1 μs.....79

4.26 Consecutive images of Taylor impact test on PTFE 7A / Ti composite (Batch #3, medium size), V_i=281.32m/s, t_{exp}=500ns, and t_{int}=1.5 μs.....79

4.27 Consecutive images of Taylor impact test on PTFE 7A / Ti composite (Batch #3, medium size), V_i=204.59m/s, t_{exp}=500ns, and t_{int}=1.75 μs.....80

4.28 Consecutive images of Taylor impact test on PTFE 7A / Ti composite (Batch #3, medium size), V_i=88.99m/s, t_{exp}=500ns, and t_{int}=2.5 μs.....80

4.29 Axial strain and areal strain *vs.* image sequence of PTFE 7A / Ti composite (Batch #3) under four different impact velocities.....81

4.30 Ignition time versus kinetic energy based on Taylor impact test at four different impact velocities (Batch #3).....82

4.31 Consecutive images of Taylor impact test on PTFE 7A / Ti composite (Batch #3, small size), V_i=201.44m/s, t_{exp}=500ns, and t_{int}=1.75 μs.....83

4.32 Consecutive images of Taylor impact test on PTFE 7A / Ti composite (Batch #3, small size), V_i=91.08m/s, t_{exp}=500ns, and t_{int}=2.5 μs.....83

4.33 Consecutive images of Taylor impact test on PTFE 7A / Ti composite (Batch #3, even smaller size), V_i=204.11m/s, t_{exp}=500ns, and t_{int}=1.75 μs.....83

4.34 Consecutive images of Taylor impact test on PTFE 7A / Ti composite (Batch #3, even smaller size), V_i=100.64m/s, t_{exp}=500ns, and t_{int}=2.5 μs.....84

4.35 Consecutive images of Taylor impact test on PTFE 7A / Ti composite (Batch #3, large size), V_i=498m/s, t_{exp}=500ns, and t_{int}=0.75 μs.....85

4.36 Consecutive images of Taylor impact test on PTFE 7A / Ti composite (Batch #3, large size), V_i=399.02m/s, t_{exp}=500ns, and t_{int}=1 μs.....85

4.37 Consecutive images of Taylor impact test on PTFE 7A / Ti composite (Batch #3, large size), V_i=~300m/s, t_{exp}=500ns, and t_{int}=1.5 μs.....85

4.38 Consecutive images of Taylor impact test on PTFE 7A / Ti composite (Batch #3, large size), V_i=196.53m/s, t_{exp}=500ns, and t_{int}=1.5 μs.....86

4.39 Consecutive images of Taylor impact test on PTFE 7A / Ti composite (Batch #3, large size), V_i=90.95m/s, t_{exp}=500ns, and t_{int}=2 μs.....86

4.40 Specimen radius *vs.* axial position at three frame times.....88

4.41 Strain *vs.* axial position at three frame times.....88

4.42 Three frames selected for film reduction analysis at V_i = 112.38m/s (large dimension sample from Batch #2).....90

4.43 Film data analysis results for Batch #2 large dimension sample at V_i = 112.38m/s, (a) strain *vs.* axial position plots at three different times; (b) stress *vs.* strain curves at two intervals; (c) strain rate *vs.* strain curves at two intervals.....90

4.44 Three frames selected for film reduction analysis at V_i = 201.01m/s (large dimension sample from Batch #2).....91

4.45 Film data analysis results for Batch #2 large dimension sample at V_i = 201.01m/s, (a) strain *vs.* axial position plots at three different times; (b) stress *vs.* strain curves at two intervals; (c) strain rate *vs.* strain curves at two intervals.....91

4.46 Three frames selected for film reduction analysis at V_i = 282.56m/s (large dimension sample from Batch #2).....92

4.47 Film data analysis results for Batch #2 large dimension sample at V_i = 282.56m/s, (a) strain *vs.* axial position plots at three different times; (b) stress *vs.* strain curves at two intervals; (c) strain rate *vs.* strain curves at two intervals.....92

4.48 Three frames selected for film reduction analysis at V_i = 406.44m/s (large dimension sample from Batch #2).....93

4.49 Film data analysis results for Batch #2 large dimension sample at V_i = 406.44m/s, (a) strain *vs.* axial position plots at three different times; (b) stress *vs.* strain curves at two intervals; (c) strain rate *vs.* strain curves at two intervals.....93

4.50 Three frames selected for film reduction analysis at V_i = 90.95m/s (large dimension sample from Batch #3).....94

4.51 Film data analysis results for Batch #3 large dimension sample at V_i = 90.95m/s, (a) strain *vs.* axial position plots at three different times; (b) stress *vs.* strain curves at two intervals; (c) strain rate *vs.* strain curves at two intervals.....94

4.52 Three frames selected for film reduction analysis at V_i = *196.53*m/s (large dimension sample from Batch #3).....95

4.53 Film data analysis results for Batch #3 large dimension sample at V_i = 196.53m/s, (a) strain *vs.* axial position plots at three different times; (b) stress *vs.* strain curves at two intervals; (c) strain rate *vs.* strain curves at two intervals.....95

4.54 Three frames selected for film reduction analysis at V_i = ~ 300m/s (large dimension sample from Batch #3).....96

4.55 Film data analysis results for Batch #3 large dimension sample at V_i = ~300m/s, (a) strain *vs.* axial position plots at three different times; (b) stress *vs.* strain curves at two intervals; (c) strain rate *vs.* strain curves at two intervals.....96

4.56 Three frames selected for film reduction analysis at V_i = 399.02m/s (large dimension sample from Batch #3).....97

4.57 Film data analysis results for Batch #3 large dimension sample at V_i = 399.02m/s, (a) strain *vs.* axial position plots at three different times; (b) stress *vs.* strain curves at two intervals; (c) strain rate *vs.* strain curves at two intervals.....97

4.58 The sketch for Taylor impact test setup with sample attached onto anvil.....100

4.59 XRD patterns of post-impact product at V_i = ~200m/s (Batch #1).....101

4.60 Consecutive images of Taylor impact test on PTFE 7A / Ti composite of Batch #1 (a) medium dimension sample at V_i = 308m/s; (b) small dimension sample at V_i = 309m/s; (c) even smaller dimension sample at V_i = ~300m/s.....103

4.61 Consecutive images of Taylor impact test on PTFE 7A / Ti composite of Batch #2 (a) medium dimension sample at V_i = 201m/s, (b) small dimension sample at V_i = 199m/s, (c) even smaller dimension sample at V_i = 203m/s.....104

4.62 Consecutive images of Taylor impact test on PTFE 7A / Ti composite of Batch #3 (a) medium dimension sample at V_i = 205m/s; (b) small dimension sample at V_i = 201m/s; (c) even smaller dimension sample at V_i = 204m/s.....104

4.63 Comparison of consecutive images of Taylor impact test on PTFE 7A / Ti medium dimension composite (a) Batch #1 at V_i = 308m/s; (b) Batch #2 at V_i = 304m/s; (c) Batch #3 at V_i = 281m/s.....106

4.64 Comparison of consecutive images of Taylor impact test on PTFE 7A / Ti medium dimension composite (a) Batch #1 at V_i = 188.73m/s; (b) Batch #2 at V_i = 200.96m/s; (c) Batch #3 at V_i = 204.59m/s.....106

5.1 The experimental and fitted stress *vs.* strain curves of PTFE 7A / Ti composite at the strain rate of $2500s^{-1}$.....112

5.2 The experimental and fitted stress *vs.* strain curves of PTFE 7A / Ti composite at the strain rate of $0.01s^{-1}$.....113

5.3 The experimental and fitted stress *vs.* strain curves of PTFE 7A / Ti composite at the strain rate of $3600s^{-1}$.....115

5.4 The stress-strain-strain rate plane for PTFE 7A / Ti composite.....117

5.5 Simulation results of Taylor impact test at V_i = 112.38m/s (Batch #2).....119

5.6 Comparison plots of radius *vs.* axial position between experimental image and simulation results at 5 μs, V_i = 112.38m/s.....121

5.7 Comparison plots of radius *vs.* axial position between experimental image and simulation results at 15 μs, V_i = 112.38m/s.....121

5.8 Comparison plots of radius *vs.* axial position between experimental image and simulation results at 22.5 μs, V_i = 112.38m/s.....122

5. 9 Simulation results of Taylor impact test at V_i = 201.01m/s (Batch #2).....123

5.10 Comparison plots of radius *vs.* axial position between experimental image and simulation results at 6 μs, V_i = 201.01m/s.....125

5.11 Comparison plots of radius *vs.* axial position between experimental image and simulation results at 10 μs, V_i = 201.01m/s.....125

5.12 Comparison plots of radius *vs.* axial position between experimental image and simulation results at 18 μs, V_i = 201.01m/s.....126

5.13 Simulation results of Taylor impact test at V_i = 282.56m/s (Batch #2).....127

5.14 Comparison plots of radius *vs.* axial position between experimental image and simulation results at 6 μs, V_i = 282.56m/s.....129

5.15 Comparison plots of radius *vs.* axial position between experimental image and simulation results at 10 μs, V_i = 282.56m/s.....129

5.16 Simulation results of Taylor impact test at V_i = 406.44m/s (Batch #2).....131

5.17 Comparison plots of radius *vs.* axial position between experimental image and simulation results at 2.5 μs, V_i = 406.44m/s.....132

5.18 Comparison plots of radius *vs.* axial position between experimental image and simulation results at 5 μs, V_i = 406.44m/s.....132

5.19 Comparison plots of radius *vs.* axial position between experimental image and simulation results at 7.5 μs, V_i = 406.44m/s.....133

6.1 SEM image, binary image and vectorized image of three batches.....138

6.2 Stress vs. strain plots at various strain rates for PTFE material at 296K.....139

6.3 The stress-strain-strain rate plan for Ti material with twinning effect at 296K.....140

6.4 Microstructural simulation results of Taylor impact test at V_i = 200m/s (Batch #1) 142

6.5 Microstructural simulation results of Taylor impact test at V_i = 200m/s (Batch #2) 146

6.6 Microstructural simulation results of Taylor impact test at V_i = 200m/s (Batch #3) 149

6.7 Comparison of microstructural simulation results on Batch #1 and Batch #2.....153

C.1 The schematic diagram of binary image and the relation between pixel coordinate and node coordinate.....174

LIST OF SYMBOLS AND ABBREVIATIONS

PTFE	Polytetrafluorethylene. Used in the current work as one of the composite components.
$u(x, t)$	Displacement of the particle location at position x and time t. Used in one dimensional wave propagation equation.
C_0	Longitudinal (dilatational) wave velocity, also called the bulk sound velocity.
F	Function describing the shape of the pulse propagating in the positive direction
G	Function describing the shape of the pulse propagating in the negative direction
V_p	Plastic wave velocity
U_s	Shock wave front velocity
U_p	Compressed particle velocity
EOS	Equation of State
SHPB	Split Hopkinson Pressure Bar
ε_i	Incident strain. Used in SHPB test.
ε_r	Reflected strain. Used in SHPB test.
ε_t	Transmitted strain. Used in SHPB test.
$\dot{\varepsilon}$	Strain rate
V_c	Critical impact velocity, below which the deformation is purely elastic
σ_{yd}	Yield stress in Taylor's theory
VISAR	Velocity Interferometer System for Any Reflector

PVDF	Polyvinylidene Difluoride
PC	Polycarbonate
PET	Polyethylene Terephthalate
PMMA	Polymethylmethacrylate
PEEK	Polyetheretherketone
Nylatron	A tradename for a Nylon 6, 6 derivative
DSC	Differential Scanning Calorimetry
PE	Polyethylene
HDPE	High Density Polyethylene
SIC	Strain-Induced Crystallization
PS	Polystyrene
BCC	Body-Centered Cubic
HCP	Hexagonal Close Packed
FCC	Face-Centered Cubic
Y	Yield stress in Hutchings model
ε_y	Yield strain in Hutchings model
σ	Von Mises flow stress in Johnson-Cook model
ε^p	Plastic strain
$\Delta\sigma_G$	Short-ranged thermally activated barriers in Zeriili-Armstrong model
$\Delta\sigma_G{}'$	Long-ranged athermal barriers in Zerilli-Armstrong model
σ_{JCP}	Von Mises effective stress in modified Johnson-Cook model
TMD	Theoretical Maximum Density
SEM	Scanning Electron Microscope

DTA	Differential Thermal Analysis
XRD	X-Ray Diffraction
a	Lattice parameter
x	C/Ti ratio in TiC_x compound
V_i	Impact velocity of Taylor impact test in current work
t_{exp}	Exposure time of camera setting in current work
t_{int}	Interframe time of camera setting in current work
C_v	Specific heat capacity
FEA	Finite Element Analysis

SUMMARY

As one category of energetic materials, impact-initiated reactive materials are able to release a high amount of stored chemical energy under high strain rate impact loading, and are used extensively in civil and military applications. In general, polymers are introduced as binder materials to trap the reactive metal powders inside, and also act as an oxidizing agent for the metal ingredient. Since critical attention has been paid on the metal / metal reaction, only a few types of polymer / reactive metal interactions have been studied in the literature. With the higher requirement of materials resistant to different thermal and mechanical environments, the understanding and characterization of polymer / reactive metal interactions are in great demand. In this study, PTFE (Polytetrafluoroethylene) 7A / Ti (Titanium) composites were studied under high strain rates by utilizing the Taylor impact and SHPB tests. Taylor impact tests with different impact velocities, sample dimensions and sample configurations were conducted on the composite, equipped with a high-speed camera for tracking transient images during the sudden process. SHPB and Instron tests were carried out to obtain the stress *vs.* strain curves of the composite under a wide range of strain rates, the result of which were also utilized for fitting the constitutive relations of the composite based on the modified Johnson-Cook strength model. Thermal analyses by DTA tests under different flow rates accompanied with XRD identification were conducted to study the reaction mechanism between PTFE 7A and Ti when only heat was provided. Numerical simulations on Taylor impact tests and microstructural deformations were also performed to validate the

constitutive model built for the composite system, and to investigate the possible reaction mechanism between two components. The results obtained from the high strain rate tests, thermal analyses and numerical simulations were combined to provide a systematic study on the reaction mechanism between PTFE and Ti in the composite systems, which will be instructive for future energetic studies on other polymer / reactive metal systems.

CHAPTER I

INTRODUCTION

1.1 Motivation and Objectives

Over 1000 years ago, as the first explosive, black powder, was invented in China, energetic materials started to unfold a broad and splendid panorama in the history of human development. Energetic materials store an extraordinary high amount of chemical energy that can be released under certain circumstances, e.g., high temperature, high pressure and/or ignition. Based on their application field, energetic materials can be classified as explosives, pyrotechnics, propellants or weapon ammunition [1]. As a special category of energetic material, impact-initiated reactive materials can only initiate chemical reactions under high impact loading while remaining inert in ordinary conditions. This type of material has gained special attention due to its novel approach to obtain compounds with superior properties, e.g., high density and highly refined microstructure compared with ones obtained through conventional techniques, and its potential significance for the control of energy release [2].

Similar to impact-initiated reactive materials but at a higher triggering pressure level, shock-initiated reactive materials have been systematically studied for several systems, e.g., Ti (Titanium) / C (Graphite) [3-7], Ni (Nickel) / Al (Aluminum) [8-10], Ti / Si (Silicon) [11-13], etc. In contrast, only a few types of polymer-based impact / shock-initiated reactive material systems have been explored, partially due to the intrinsic complexity of polymeric materials [14-17]. In general, polymers applied in reactive

materials can be classified into two groups: (1) As binder materials to trap the metal powders inside, and also to act as oxidizing agents for the redox reactions with the metal ingredient; (2) As ingredients in the application of light armor systems [18]. With the higher requirements of light-weight reactive materials resistant to different thermal and mechanical environments, the understanding and characterization of polymer-based impact / shock-initiated reactive materials are in great demand.

For polymer-based impact / shock-initiated reactive material systems, several key points highlight difficulties in the research work: (1) To understand the fundamental mechanism of the impact / shock-initiated transformation; (2) To establish the kinetic / thermodynamic parameters of the impact / shock-initiated transformation (e.g. pressure, temperature, etc.); (3) To understand and study the by-product of the impact / shock-initiated transformation; (4) To obtain the constitutive relation and EOS (Equation of State) for the impact / shock-initiated reactive material system; and (5) To explore the application of the impact / shock-initiated transformation.

In the current research, a polymer / reactive metal composite system, PTFE (Polytetrafluorethylene) / Ti, was chosen to explore the fundamentals of impact-initiated reaction mechanism by utilizing high strain-rate techniques. As a highly reactive metal, Ti was thoroughly studied with graphite as a shock-induced / shock-assisted combination [3-7]. A significant part of this reaction (>70%) was complete as the stress wave passed through the blended material in the time scale of 100 nanoseconds. For the current study, PTFE provided the carbon source as it is decomposed under the stress wave of impact. Other polymers may also be able to serve as carbon sources, but the simplicity in

structure, toughness and good resistance to thermal / chemical degradation qualified PTFE as a viable polymer candidate for the impact-initiated reaction system.

The objective of this research work was to understand the chemical and mechanical behaviors of the PTFE / Ti composite system under high strain rates. The overall objective was separated into four main aspects:

1. Study the chemical responses of PTFE / Ti composite under high strain rates: (a) Prove the existence of impact-initiated transformation processes and identify possible by-products; (b) Study the main factors having influences on the reactivity of the system, and propose the reaction mechanism between PTFE and Ti under high impact loading.

2. Study the mechanical properties of the PTFE / Ti composite under high strain rates and analyze its dynamic behaviors before the impact-initiated chemical reaction is triggered.

3. Build the constitutive model for the PTFE / Ti composite to describe and predict its mechanical behaviors under high strain rates.

4. Simulate the dynamic behaviors of the PTFE / Ti composite by incorporating built constitutive relationships under high strain rates.

1.2 Scope of Study

The PTFE / Ti composite system was investigated through high strain rate techniques in a wide strain rate range. The impact-initiated chemical reaction was studied with various impact velocities, sample dimensions and sample configurations by utilizing the Taylor impact test equipped with an *Imacon 2000* high-speed digital camera. Transient images taken during the impact process were analyzed as a main approach to

verify the reactivity and deformation behavior of this composite system. A series of stress *vs.* strain curves in a wide strain rate range obtained by SHPB (Split Hopkinson Pressure Bar) and Instron tests were employed to build the constitutive relation for the PTFE / Ti composite based on one polymer / reactive metal constitutive model proposed in the literature. Dynamic simulations on both macroscopic motion and microstructure were presented and compared with experimental data to validate the proposed constitutive relationship and the reaction mechanism.

In Chapter II, a brief introduction to the background in shock wave propagation, high strain rate techniques, shock-induced transformation and constitutive models for polymeric materials under high strain rates was presented. In Chapter III, the PTFE 7A / Ti composite system studied in this thesis work was presented and characterized in terms of its configurations, thermal properties and mechanical properties. In Chapter IV, a detailed and thorough investigation on the mechanical and chemical behaviors of PTFE 7A / Ti composite by means of Taylor impact test was shown and discussed with different experimental variables. In Chapter V, simulation results on Taylor impact test based on one newly-developed constitutive model were compared and evaluated with experimental data. Finally in Chapter V, microstructural simulation was conducted to study the influence of configuration on the reactivity of the PTFE 7A / Ti composite system.

CHAPTER II

BACKGROUND

2.1 Foundation of Wave Propagation

2.1.1 Elastic Wave and Plastic Wave

When a material is under dynamic compression loading, two types of waves are generated once the amplitude of the impact impulse exceeds the elastic limit of the material. One type is the elastic wave, and the other is the plastic wave. The elastic wave is defined as the wave propagating in an elastic or viscoelastic medium with the original position of the medium restored and without energy dissipation [19]. The elastic wave equation in a one dimensional case is given as:

$$\frac{\partial^2 u}{\partial t^2} = \frac{\partial^2 u}{C_0{}^2 \partial x^2} \tag{2.1}$$

where *u(x, t)* is the displacement of the particle located at position *x* at time *t*, and C_0 is the longitudinal (dilatational) wave velocity, $C_0 = \sqrt{\frac{E}{\rho}}$. C_0 is also called the bulk sound velocity, which is the sound velocity in the material at zero pressure. The general solution to the elastic wave equation is:

$$u(x,t) = F(x - C_0 t) + G(x + C_0 t) \tag{2.2}$$

The two functions *F* and *G* describe the shape of the pulse propagating in the positive and negative directions along the *x* axis at the velocity of C_0, respectively.

The plastic wave always travels slower than the elastic wave, and its velocity depends on the local stress. The higher the stress, the slower the velocity of the plastic wave. The plastic wave causes unrecoverable strain left in the material, and its velocity is expressed as [19]:

$$V_p = \left(\frac{d\sigma / d\varepsilon}{\rho}\right)^{1/2} \tag{2.3}$$

2.1.2 Shock Wave

The shock wave is a special case of elastic-plastic wave, which is simply defined as a discontinuity in pressure, temperature (or internal energy) and density. The shock wave is produced by rapidly imparting momentum onto the material surface, causing sudden changes in material properties. Under such conditions, the shock wave is treated as a fluid, neglecting the deviatroic component of the stress. Assume the shock front travels at a velocity of U_s, and the velocity of compressed particle is U_p, the material has initial density ρ_0 (or initial specific volume V_0) and initial internal energy E_0. After the shock wave travels through, the material has density ρ (or specific volume V) and internal energy E. Applying mass, momentum and energy conservation onto the material before and after shock compression, Equations 2.4 - 2.6 are obtained for describing the shock state in the material:

Conservation of mass:

$$\rho_0 U_s = \rho\left(U_s - U_p\right) \tag{2.4}$$

Conservation of momentum (changes in momentum equals to the impulse):

$$P - P_0 = \rho_0 U_s U_p \tag{2.5}$$

Conservation of Energy (changes of work done on the system equals to the increase of energy):

$$E - E_0 = \frac{1}{2}(V - V_0)(P + P_0) \tag{2.6}$$

A total of five variables are contained in Equations 2.4-2.6. A fourth equation needs to be added if one variable needs to be expressed as a function of any one of them. This additional equation is obtained by relating U_s to U_p:

$$U_s = C_0 + S_1 U_p + S_2 U_p{}^2 + \ldots \tag{2.7}$$

where Equation 2.7 is called the Equation of State (EOS), which must be determined experimentally.

The relationship between pressure and density (or specific volume *V*) is the Rankine-Hugoniot equation, which is defined as the locus of all shocked states [19]. Figure 2.1 schematically illustrates the Hugoniot curves for solid and porous materials [20]. The straight line connecting initial state (P_0, V_0) and any other state (P_1, V_1) is defined as Rayleigh line, which describes the shock state at P_1.

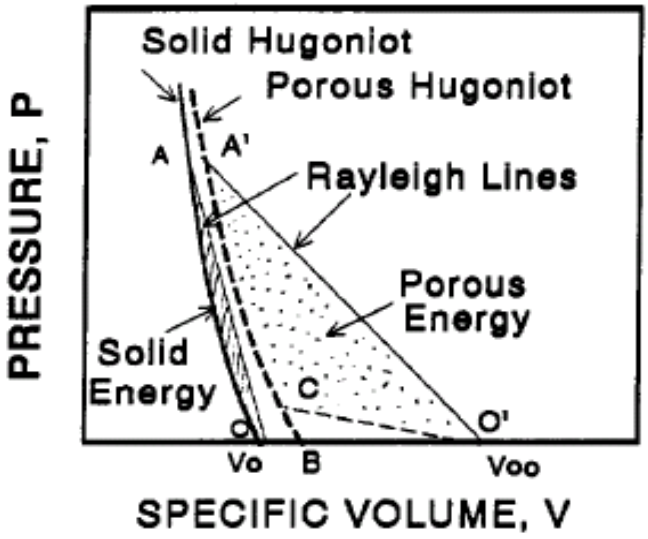

Figure 2.1. A schematic illustration of *P* – *V* Hogoniot curve for solid and porous materials [20]

The change of shock state does not follow the Hogoniot curve, but jumps to the (P_1,V_1) state directly from the initial state. The discontinuity property of the shock wave can be illustrated by the slope of the Rayleigh line. Figure 2.1 also shows the energy deposition to the material by the area between the Hugoniot curve and the Rayleigh line. Porous material obviously absorbs much more energy than solid material because of the extra energy required in compacting the porous material [20].

Carter and Marsh obtained a series of Hugoniot curves for a group of thermoplastic and thermosetting polymers by means of high explosive shock generator and streak camera to take record of the time *vs.* velocity information, the most thorough shock data collection for polymeric materials at that time [21]. High pressure transformations were observed for most of the testing polymers accompanied by obvious volume changes. Typical Hugoniot data are shown in Figure 2.2, from which a change in slope at around U_p=3km/s could be found in the U_p *vs.*U_s curve for polystyrene.

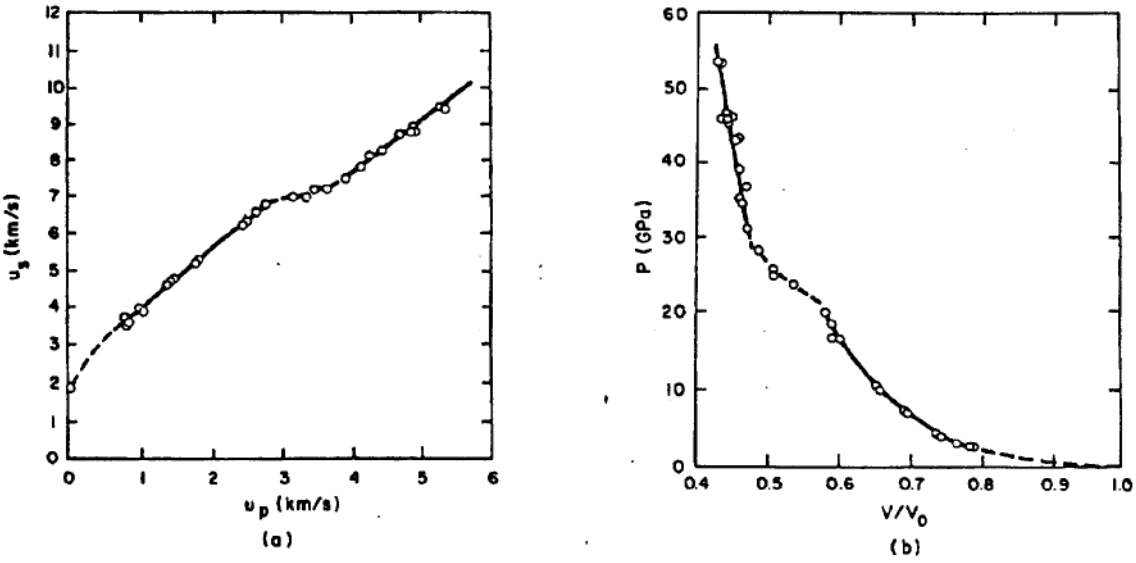

Figure 2.2. Hugoniot data (a) U_p *vs.* U_s and (b) V/V_0 *vs.* P for polystyrene [21]

The authors attributed this phenomenon to the molecular reordering due to the strong interchain interactions at relative high pressure. They further claimed that polymers containing aromatic ring structures would display a more intense transformation and larger volume change since the molecule would undergo a graphite-diamond like transformation [22].

2.2 High Strain Rate Measurement

Based on the range of strain rates, test techniques for measuring the mechanical properties at high strain rates (~ 10^2 to ~ 10^6 s^{-1}) could be categorized into several levels:

(1) 10^2 - 10^3 s^{-1}: Drop weight method

(2) 10^3 - 10^4 s^{-1}: SHPB

(3) 10^4- 10^5 s^{-1}: Taylor impact test

(4) $> 10^5\ s^{-1}$: Plate impact test

Categories (2) - (4) will be roughly discussed in terms of their working mechanisms as applied in this research work.

2.2.1 SHPB (Split Hopkinson Pressure Bar) Test

SHPB is one of the most widely used tests for measuring the dynamic mechanical properties of materials in compression, tension and torsion modes. As the simplest case, SHPB in compression mode consists of a striker bar, an incident bar, an output bar and a specimen placed in between (Figure 2.3):

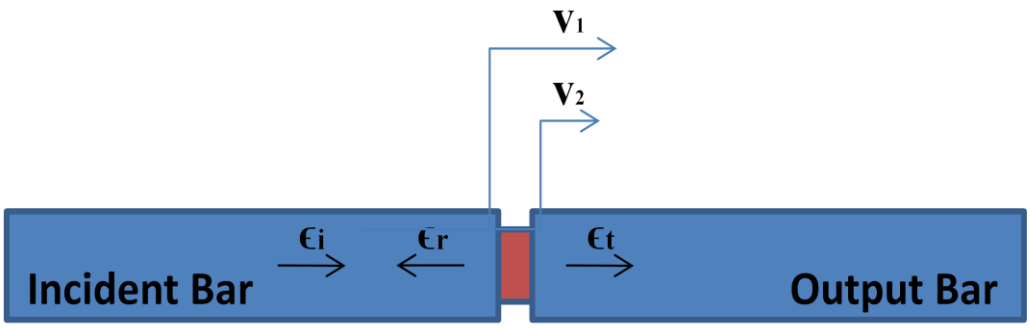

Figure 2.3. A schematic illustration of the main parts in SHPB test

When the striker bar propelled by gas strikes the incident bar, a rectangular compression wave is generated and travels through the incident bar until it reaches the specimen. At this point, some of the incident wave is reflected back, while some is transmitted into the specimen and then into the output bar. Based on the one-dimensional wave propagation analysis shown in Equation 2.1 and 2.2, strain and velocity in the incident bar are defined as in Equation 2.8 and 2.9:

$$\varepsilon = \frac{\partial u}{\partial x} = F' + G' = \varepsilon_i + \varepsilon_r \tag{2.8}$$

$$v = \frac{\partial u}{\partial t} = C_0(-F' + G') = C_0(-\varepsilon_i + \varepsilon_r) \tag{2.9}$$

where F' and G' are the derivatives of function F and G with respect to distance x. ε_i and ε_r represent the incident and reflected strain respectively. Since only the transmitted wave is propagating in the output bar, the velocity in the output bar is given as:

$$v = -C_0\varepsilon_t \tag{2.10}$$

where ε_t represents the transmitted strain. The strain rate in the specimen is calculated as:

$$\dot{\varepsilon} = \frac{(v_1 - v_2)}{l_s} \tag{2.11}$$

where l_s is the length of the specimen, v_1 and v_2 represent the velocity in the incident and output bar, respectively. Combining Equation 2.9 to 2.11, the strain rate in the specimen is calculated by the strains in the bar:

$$\dot{\varepsilon} = \frac{C_0}{l_s}(-\varepsilon_i + \varepsilon_r + \varepsilon_t) \tag{2.12}$$

Assuming the specimen deforms uniformly, the forces on both sides of the specimen are the same, which leads to Equation 2.13:

$$\varepsilon_i + \varepsilon_r = \varepsilon_t \tag{2.13}$$

Substituting Equation 2.13 into Equation 2.12 gives the strain rate only in terms of the reflected strain. By integrating the strain rate with time, strain in the specimen is calculated. Stress in the specimen is obtained by dividing the force in the transmission side by the cross-sectional area of the specimen (one-wave stress analysis). The final

stress *vs.* strain relationship and the strain rate equation are shown in Equations 2.14 - 2.16. Figure 2.4 shows the typical SHPB plots for the PTFE 7A material:

$$\dot{\varepsilon} = \frac{2C_0\varepsilon_r}{l_s};\ \sigma_{(t)} = \frac{AE\varepsilon_t}{A_s};\ \varepsilon_{(t)} = \frac{2c}{l_s}\int_0^t \varepsilon_r dt \qquad (2.14) - (2.16)$$

PTFE 7A is one type of Teflon® fluoropolymer products exhibiting a very small particle size and a high bulk density. The detailed material properties of PTFE 7A will be elaborated on in Chapter 3.1.

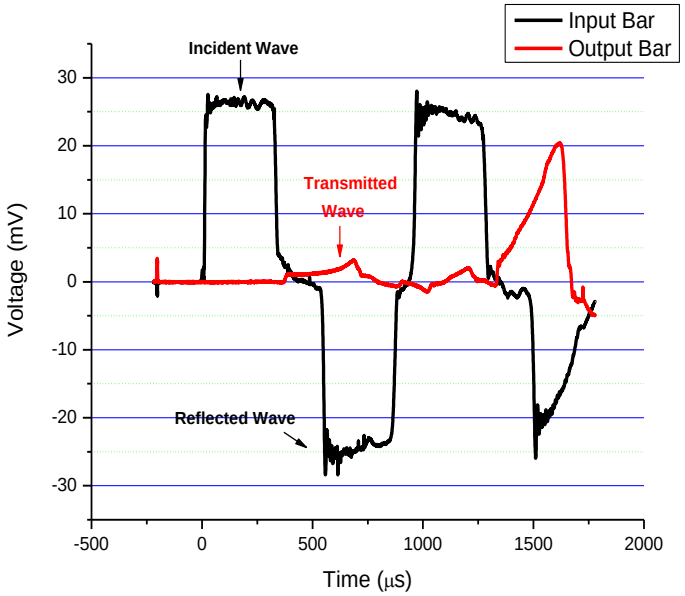

(a)

Figure 2.4. SHPB plots of PTFE 7A sample at the strain rate of 2250 s^{-1}: (a) The input and output impulse waves; (b) The stress *vs.* strain curves extracted from plot (a)

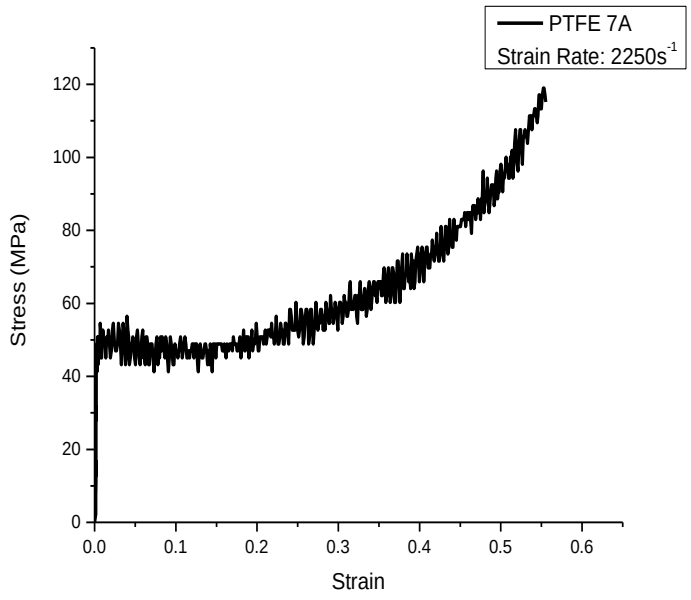

(b)

Figure 2.4. Continued

2.2.2 Taylor Impact Test

The Taylor impact test was first developed by G. I. Taylor for estimating the dynamic stress of metal material in compression [23-25]. The Taylor test consists of simply hitting a cylindrical projectile onto a rigid anvil and measuring the sizes of the projectile before and after impact to estimate the yield stress of this material by a series of analysis procedures. A cylindrical projectile with length *L* impacts onto a hard anvil at a velocity of *U*, at which point an elastic wave is generated at velocity *c* followed by a plastic wave of velocity *v* propagating towards the rear end of the projectile. The elastic wave first reaches the end of the projectile and reflects back to the front until it meets the plastic wave, where the whole process stops. By considering the plastic region (Figure

2.5 (a)) and the elastic region (Figure 2.5 (b)) separately, relationships 2.17, 2.18, and 2.20 are established by applying mass conservation and momentum conservation at the interfaces.

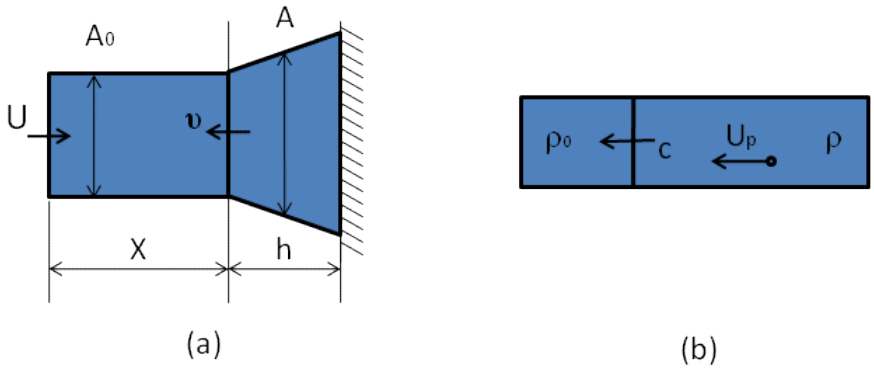

Figure 2.5. The detailed view of (a) plastic and (b) elastic wave propagation

Cons. of mass: $A_0(U+v) = Av\,,\ \rho \approx \rho_0$ (2.17)

Cons. of momentum: $\rho A_0(U+\upsilon) = \sigma_{yd}(A - A_0)$ (2.18)

$$\frac{\rho U^2}{\sigma_{yd}} = \frac{\varepsilon^2}{1-\varepsilon} \tag{2.19}$$

Cons. of mass: $\rho_0 C = \rho(C - U_p)$ (2.20)

The series of Equations 2.19, 2.21 and 2.22 - 2.24 can be derived from the three basic relations:

$$U_p = \sigma / c\rho_0 \tag{2.21}$$

Particle velocity in Region (1): U (2.22)

Particle velocity in Region (2): $U - \sigma_{yd} / c\rho_0$ (2.23)

Particle velocity in Region (3): $U - 2\sigma_{yd} / c\rho_0$ (2.24)

where σ_{yd} is the yield stress. Equations 2.22 - 2.24 give the particle velocities in three different regions as the projectile deforms: Region (1): the region between the elastic wave front and the back surface of the projectile; Region (2): the region between the elastic wave and the plastic wave front; Region (3): the region between the back surface of the projectile and the reflected elastic wave front. By considering the relationships between velocity, distance and time of the two types of waves, Equation 2.25 can be obtained, relating the extent of the deformation to the yield stress and strain:

$$\frac{dx}{x} = \frac{\rho_0}{\sigma_{yd}\varepsilon} U dU \tag{2.25}$$

By integrating Equation 2.25 and combining the resultant relation with Equation 2.19, a well-known plot of: $\frac{L_1}{L}$ $(and\ \frac{L_1-X}{L})$ *vs.* $\frac{\rho U^2}{\sigma_{yd}}$ is obtained (Figure 2.6). An approximate formula and a more accurate one with a correcting factor were both shown in Taylor's original paper [25].

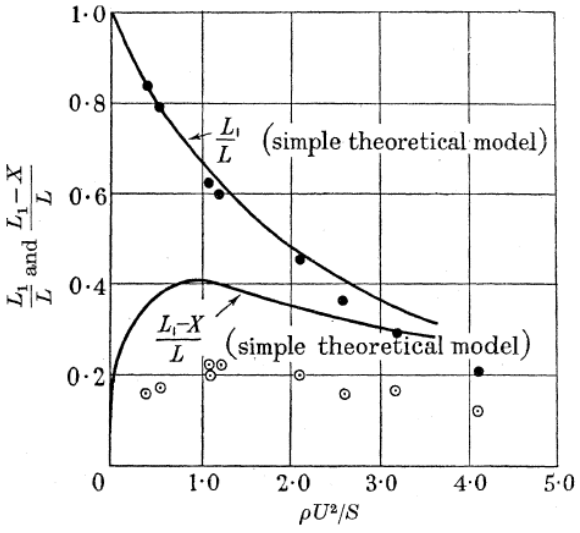

Figure 2.6. The calculation results and experimental data of $\frac{L_1}{L}$ $(and\ \frac{L_1-X}{L})$ versus $\frac{\rho U^2}{\sigma_{yd}}$ for steel [25]

Although Taylor's theory has been successfully applied to several metals for analyzing experimental data, it always overpredicts the yield stress for polymers since the theory assumes the material behavior to be rigid-plastic. The theory is not applicable to polymers which contain substantial elastic strains during deformation. A linear elastic, perfectly-plastic constitutive relation was proposed by Hutchings in interpreting data from the Taylor impact test [26]. A critical impact velocity, V_c, was found for polymeric materials below which the deformation is purely elastic. Hutchings' approach resulted in good predictive values of yield stress, especially for polymers like Polycarbonate (PC) that fractures under impact loading, or for polymers having long-term relaxations after deformation.

The use of high-speed photography developed in the 1980s has broadened the vision of the Taylor test, providing detailed deformation records during the impact process. House et al. developed a film data reduction method to extract the strain, strain rate, back end velocity and stress information from every single film record, finally building up the stress *vs*. strain curves [27]. With the development of finite element simulation software accompanied by high-speed photography, the Taylor test is no longer used for determining the yield stress of materials, but for validating the constitutive relation of the test material by comparing experimental observations from transient images with simulation results.

2.2.3 Plate Impact Test

Figure 2.7 presents a general configuration of plate impact test. A plate is shot onto a target specimen at a velocity up to 1.2 km/s to produce planar shock waves in one dimensional strain condition:

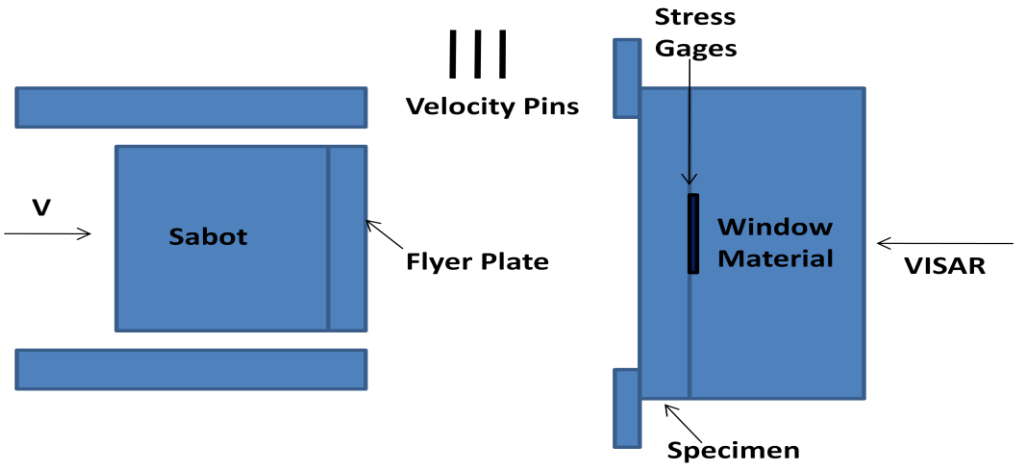

Figure 2.7. A schematic diagram of plate impact test

One typical application of this test is to obtain the Hugoniot curve for the specimen material. Velocity Interferometer System for Any Reflector (VISAR) allows for the direct measurement of the particle velocity, U_p, at the rear of the specimen based on the principle of laser interferometry. A transparent window material having similar shock impedance with the specimen is placed between the back surface of the specimen and the *VISAR* beam for monitoring the velocity history of an interface within the specimen. Stress gauges yield stress wave *vs.* time profiles which further provides the shock wave velocity, U_s. A EOS and Hugoniot curve of the target material can be obtained from this technique.

2.3 Mechanical Responses of Polymers Under High Strain Rates

Generally speaking, yield stress increases with increasing strain rate, especially at high strain rates. An increasing strain rate means decreasing the time scale of observance, and the molecular chain is less mobile and behaves stiffer compared with the conditions

under lower strain rates. Similarly, an increasing yield stress will be observed at lower temperature due to the principle of time-temperature equivalence. According to the different mechanical responses under high strain rates, polymers can be classified into three categories [28, 29]: Category (1): A bilinear behavior of yield stress *vs.* strain rate and a sharp increase in gradient at a strain rate of ~ 10^3 s^{-1}; Category (2): A decrease in yield stress at a strain rate of ~ 10^4 s^{-1}; Category (3): A linear relationship between yield stress and strain rate. Mechanical behaviors of different polymer groups will next be presented, and the corresponding possible explanations for those phenomena will be discussed.

2.3.1 Mechanical Behaviors of Different Polymers Under High Strain Rates

Most of the polymers show the yield stress *vs.* strain rate relationships as in Category (1). In the strain rate range from 10^{-4} to 10^4 s^{-1}, the yield stresses of PC and Polyvinylidene Difluoride (PVDF) increased bilinearly with the logarithm of strain rate [30, 31], which are their genuine material properties. For PC, the bilinear relation was due to the movement of the β transition to room temperature; for PVDF, it was due to the movement of the glass transition to room temperature. The yield stress of Polyethylene Terephthalate (PET) showed a sharp increase at the strain rate of 10^3 s^{-1} and above [32, 33]. The X-Ray Diffraction (XRD) analysis showed an increase in crystallinity at high strain rates which might be attributed to the rapid strain-induced crystallization at these rates. For Polymethylmethacrylate (PMMA), a ductile to brittle transition was observed at a strain rate of ~1000 s^{-1} [34]. A typical plot of bilinearity between yield stress and strain rate is shown in Figure 2.8 for PC [31]:

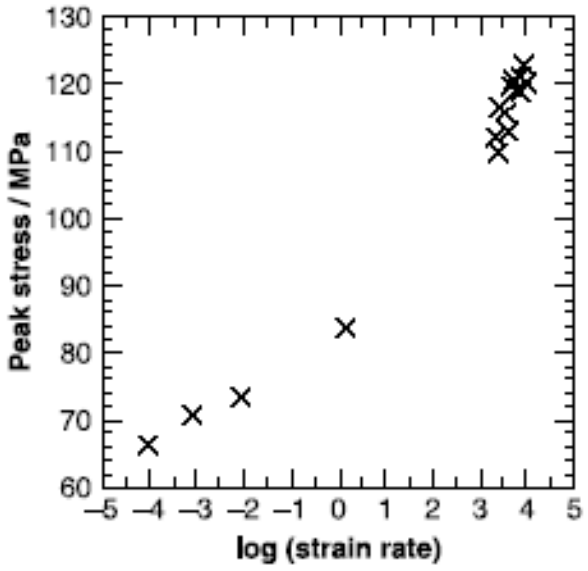

Figure 2.8. Maximum stress *vs.* strain rate at 21 ℃ for PC [31]

Polyetheretherketone (PEEK) and Nylatron (a Nylon 6,6 derivative) fall into Category (2). The polymers' flow stresses peaked and then fell again at strain rates greater than 10^4 s^{-1} (shown in Figure 2.9) [35]. Differential Scanning Calorimetry (DSC) and XRD results suggested that the change in crystallinity, rather than the introduction of an extra activated process, was the source of the rapid flow stress change. However, the reason for the decrease in crystallinity at very high strain rate (10^4 s^{-1}) was not provided.

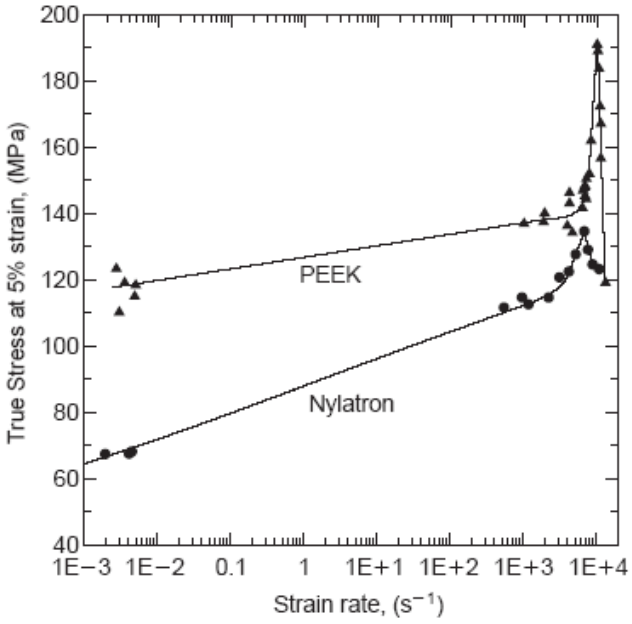

Figure 2.9. Flow stress at 5% strain *vs.* strain rate for PEEK and Nylatron [35]

Polyethylene (PE) may be the only polymer that follows the linear yield stress *vs.* strain rate behavior as detailed in Category (3). An increase in the yield stress dependence on stress was first observed by Briscoe and Hutchings [36] and other authors studying High Density Polyethylene (HDPE) (Figure 2.10):

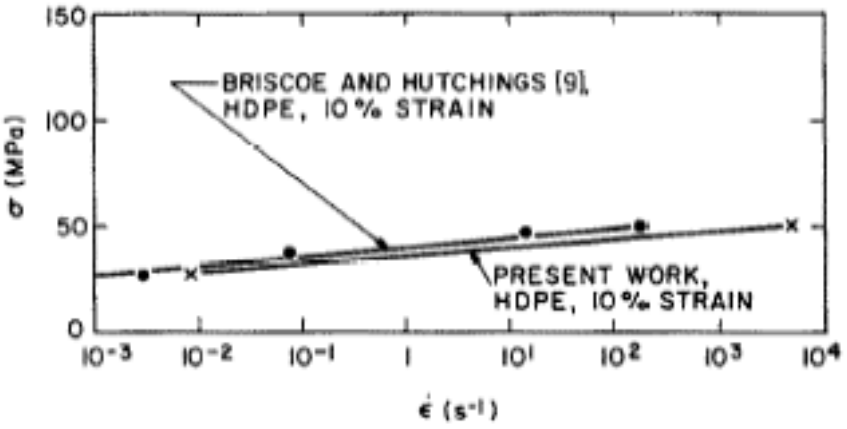

Figure 2.10. Flow stress at 10% strain *vs.* strain rate for PE [36]

Briscoe and Nosker later cast doubt on the validity of these earlier measurements. After considering the effects of friction and specimen response in the Hopkinson bar [37, 38], they concluded that the yield stress of HDPE was linear with the logarithm of strain rate.

2.3.2 Explanations for the Mechanical Behaviors of Polymers Under High Strain Rates

Several explanations for polymer yield stress dependence on strain rate have been given in the literature. Secondary molecular transitions is so far the most widely used and accepted theory, which is based on the activation energy change first proposed by Ree and Eyring [39]. The theory provides an analytical model capable of capturing polymer yield behavior across a transition threshold, beyond which the yield stress shows an increased sensitivity to strain rate / temperature. Multiple rate-activated processes are allowed and these processes are assumed to be related to specific degrees of freedom of polymer chains. The Ree-Eyring theory thus explains the transition behavior in terms of molecular-level motions. When a particular degree of freedom of the polymer chain becomes restricted at high strain rate / low temperature, the corresponding process begins dominating the overall material deformation behavior. Bauwen and his co-workers later built a modified version of the Ree-Eyring yield model, which involves two activation processes, α and β [40]. Many other authors observed that the yield stress increased dramatically with decreasing temperature near the secondary relaxation temperature (β transition) [41-43].

Some researchers attributed the increase of yield stress of polymers under high strain rates to the increased Strain-Induced Crystallization (SIC), in which the alignment

of polymer chains give rise to an increase in the overall crystalline content in the material and hence an increase in strength and hardness. Spruiell et al. studied the effect of strain history on the crystallization behavior of PET, and they found that high strain rate could produce necking, crystallization and a high degree of orientation [44]. Swallowe et al. researched for several polymer systems, including PEEK, Polyether ketone (PEK) and PET [33]. They observed an increase of flow stress with strain rate, associated with the improvement of crystallization as shown in the XRD pattern. Al-Maliky et al. also found a relationship between strain-induced crystallization and high strain rate in both PEEK and Nylatron [35].

A study of the mechanical responses of PMMA and Polystyrene (PS) by Swallowe et al. attempted to relate the increase of flow stress at high strain rates with the activation volume change [45]. The viscous flow in Eyring's theory was adopted to study the activation energy and activation volume of polymers. Over the strain rate range from 10^{-3} to $10^{1}s^{-1}$, the activation volume decreased significantly with increasing strain rate. Other effects like density variation, change in β relaxation and change in activation energy, seemed not to play an important role in the increase of yield stress.

The effect of adiabatic heating should also be taken into account in high strain rate tests because of the low thermal diffusivities of polymers. The closer the adiabatic temperature rise approaching the glass transition temperature, T_g, the stronger the effect on the strain hardening rate. In a study by Hamdan et al. [46], the effects of adiabatic heating were observed at high strain rates in both PEEK and PEK. The resulting temperature increase could reduce yield stress and cause strain softening effects.

However, at higher strain rates, the strain rate-induced brittleness surpassed the effect of adiabatic heat and increased the yield stress again (i.e., strain hardening).

2.4 Shock-Initiated Transformation

As the shock wave propagates through a material, the intense energy it carries dissipates quickly with distance, leading to a series of discontinuous changes in the characteristics of the medium such as density, pressure, etc., which can further trigger a number of physical and chemical changes [19]. The former one could be phase transformation or defect formation, while the latter one is the theoretical foundation of this study — impact-initiated / impact-induced chemical reactions, including chemical decomposition or chemical synthesis. In this part, two shock-initiated scenarios will be introduced in terms of conditions, mechanisms and typical examples.

2.4.1 Shock-Initiated Phase Transformation

Shock-initiated phase transformation was first reported in 1956 as the discovery of α (Body-Centered Cubic (*BCC*)) to ε (Hexagonal Close Packed (*HCP*)) phase transformation of iron at 12.8 GPa [47]. Other important examples of impact-initiated phase transformation include the graphite to diamond transformation [22], graphitic to wurtzite transformation in Boron nitride (BN) [48], Bismuth (Bi) I to Bi II phase transformation [49], etc., under different high shock pressures. In the review paper summarized by Duvall et al., fundamental theories, measurement techniques, possible mechanisms and typical literature observations for shock-induced phase transformation were elaborated in detail [50]. The diffusionless phase transformation taking place on the

order of microseconds was considered to be a consequence of displacive transformation through the creation of effective nucleation sites by copious defects under shock wave loading.

The polymeric material PTFE studied in this research exhibits four different crystalline phase behaviors under various temperature and pressure combinations (Figure 2.11 (a)) [51]:

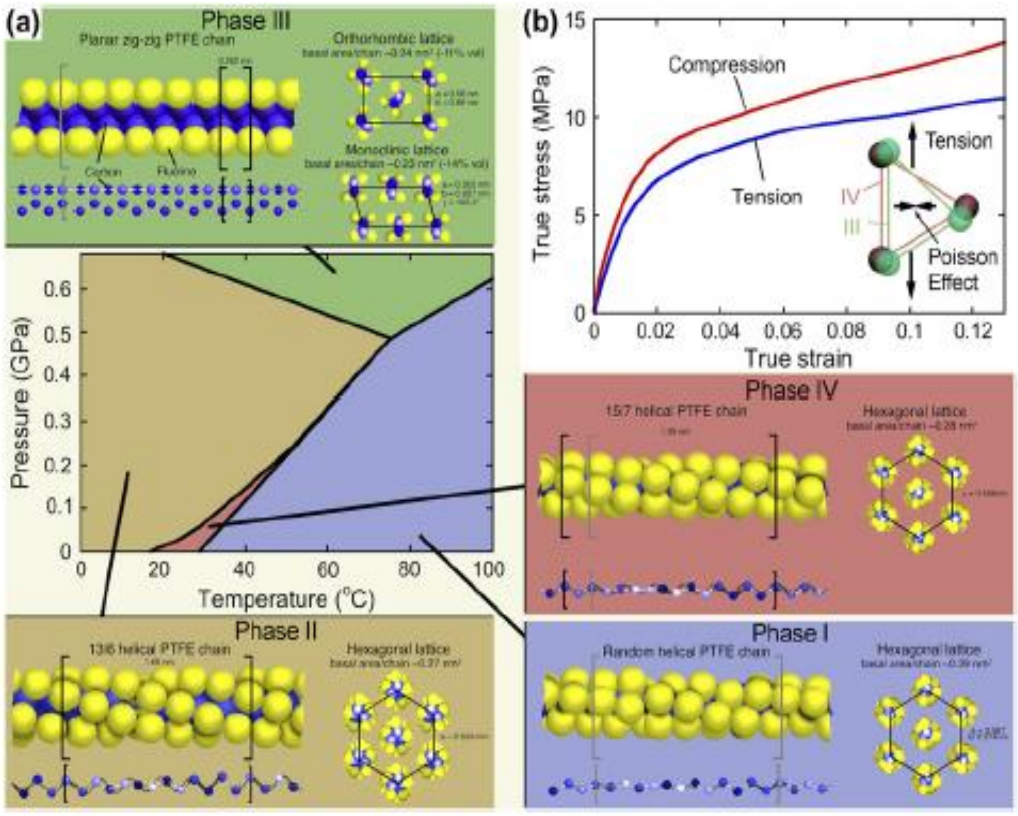

Figure 2.11. (a) PTFE crystalline phase transition behaviors under different temperature and pressure conditions; (b) stress *vs.* strain curves of PTFE at compression and tension modes [51]

At room temperature (19 ℃ - 30 ℃), PTFE presents a 15/7 helical Phase IV crystalline structure at atmospheric pressure. Below 19 ℃ and above 30 ℃, it transforms to a 13/6

helical Phase II and a random helical Phase I crystalline structure. At higher pressure (above ~0.65 GPa at room temperature), a planar zig-zag Phase III crystalline structure is formed. Fig 2.11 (b) displays the true stress *vs.* true strain curves for PTFE under compression and tension modes, which led to the conclusion that PTFE phase transitions depend mainly on temperature and pressure effects [51].

The other raw material studied in this research, Ti, changes its *HCP* structure to a *BCC* lattice form at 882 ℃ [52]. Besides four slip deformation modes associated with the unstable *HCP* structure at low stress, a twinning mode is accounted for by large deformation at high strain rates / low temperatures [53]. Twinning deformation is found to be highly dependent on temperature and strain rate, and the twinning density increases with strain rate, while decreasing with temperature [54]. Christma et al. have observed the shock-induced twinning along with an increase in hardness for Ti material [55].

2.4.2 Shock-Initiated Chemical Reaction

Since the middle of last century, shock-initiated chemical reactions have been applied in the synthesis of ceramics, intermetallic compounds and other immiscible system, and numerous compounds have been successfully synthesized, e.g., carbides [4-7, 11, 56-58], borides [59-61], aluminides [10, 61-64], silicides [13, 65-67], etc. Very similar but different in nature from shock-induced reactions, shock-assisted reactions always take place accompanied with shock-induced reactions after the shock wave passes through the material. A comparison between these two types of reactions is shown in Table 2.1 [20].

Table 2.1. A Comparison between shock-induced and shock-assisted chemical reaction

Shock-induced Reaction	Shock-assisted Reaction
During shock-compression state	Post-shock thermal treatment
Before unloading to ambient pressure	After unloading to ambient pressure
In time scale of mechanical equilibrium	In time scale of temperature equilibrium
Involving non-diffusional process and solid state structural rearrangement	Including solid-state defect-enhanced diffusional process

The thermodynamics and kinetics of shock-induced or shock-assisted reactions have also been studied extensively, although the exact mechanism has still not been firmly elaborated.

The reaction behavior of Ti and C (graphite) elemental powders has been under extensive study since 1990s [3-7]. Different from the conventional Self-Propagating High-Temperature Synthesis (SHS), one temperature-pressure cycle program was set on shock-compressed Ti and C mixtures to enhance the reactivity of this system and improve the density of the final product — Titanium Carbide (TiC_x). The shock-densified mixture was found to possess defect state and intimate interparticle contacts, which would lead to the shock-assisted, defect-enhanced, solid-state diffusion that accelerated the originally sluggish solid-state diffusion of Ti and C through the TiC_x layer. Since the objective of the current study focuses on the PTFE / Ti reaction, i.e., the chemical reaction between Ti and carbon source from the decomposition of PTFE, the reaction mechanism of Ti / C proposed in the literature helped with the understanding of the impact-initiated PTFE / Ti reaction mechanism.

In addition to the external conditions like temperature, pressure, etc., which influence the shock-induced or shock-assisted reaction processes, material property and morphology can also control the reactivity of the reaction to some degree. The Ti / Si

powder mixtures upon shock loading exhibited distinct deformation processes with Si particles of medium and large sizes [20]. Under the same shock loading pressure, the former revealed more extensive plastic deformation, flow and interconstituent mixing compared with the mixtures with larger sized Si powders. For the Ni / Al system, studies found that the flaky powder mixtures showed the most extensive deformation processes and flow of both components, next was mixtures with fine spherical morphologies, and the least plastic deformation and solid-state reaction process occurred in the Ni / Al system with coarse, rounded morphologies [9, 20]. Similar to the Ni / Al system, the PTFE / Ti composite is also characterized by a mixture of soft / hard phases, so the role of morphology factor was utilized to monitor the reactivity of this system.

Although the shock-induced reactions within metal / inorganic materials have been systematically studied since the 1960's, the chemical reactions between metal and polymeric materials have rarely been explored. In recent years, the U.S. Army Research Lab working jointly with Naval Surface Warfare Center has conducted a sequence of experiments and simulations to study the impact ignition of pressed PTFE / Al rods. A series of Taylor impact tests were carried out at various impact velocities ranging from ~ 100 to ~ 1000 m/s with framing camera sporadically tracking the impact process. Initiation light was observed above a certain initiation threshold, indicating that the chemical reaction between PTFE and Al occurred upon shock loading [15, 16]. A JCP (Johnson-Cook PSDam) constitutive relation model was also proposed to simulate the dynamic behavior of the PTFE / Al composite at high strain rates [14]. Another paper involving polymer / metal / inorganic material reactions employed PTFE as either a reaction promoter or as a carbon source in the presence of Ti and C elemental powders to

synthesis TiC-Ti composites through SHS [17]. The amount of PTFE as a reaction agent had to exceed certain threshold values to initiate the reaction between Ti and C powders. As a carbon source, PTFE directly participated in the carburizing of Ti via the products from PTFE decomposition and Ti powders, which was based on the detection of the TiF_3 intermediate product by the use of the combustion front quenching technique.

2.5 Constitutive Models for Polymers under High Strain Rates

Establishing constitutive relations for polymeric materials involve more work than that for metal / ceramic materials since polymers are more sensitive to strain rate, temperature, and pressure. The dynamic behaviors of polymers are also affected by many other structural factors, such as the degree of crystallinity, molecular weight, crystal size, phase transitions, etc. Due to the long chain structures, polymers show unique relaxation properties that highly depend on the time scale of observation. They exhibit complicated viscoelastic / viscoplastic behaviors in their stress *vs.* strain curves which deviates as the time scale of observation varies. Studies on constitutive models for polymeric materials under high strain rates have not been thoroughly and systematically conducted, but attention is now being paid because of the wide application of polymeric materials in some high strain rate-related fields, like military, aerospace, automotives, etc. An accurate constitutive model for polymers in a wide strain rate range would help simulate and predict their dynamic behaviors in some extreme conditions.

The basic constitutive model accounted for plastic flow originated from the pioneering work done by Eyring, where he treated the molecular movement as a thermally activated process that followed the Arrenhenius equation, and the activation

energy was replaced by shear stress under loading conditions [68]. In a later paper by Ree and Eyring, the model was modified to a multiple rate-activated process, in which the flow rate was dependent on relaxation times of different flow units and the distribution of such relaxation times [39].

Based on Eyring's model, Bauwens-Crowet, et al. developed a widely-used, two-process Eyring yield model [40, 69]. This model consisted of two activation processes, α and β, capable of describing molecular behaviors at low strain rates / high temperatures and high strain rates / low temperatures, respectively. Following studies have been conducted on specific polymers using this theory, and the experimental results explained [41-43]. In the following subsections, some commonly-used constitutive models, e.g., the Johnson-Cook model, the Zerilli-Armstrong model, and several other constitutive models applied to polymer / polymer composite systems, e.g., the Hutchings model, the Mulliken-Boyce model, and the modified Johnson-Cook model, will all be briefly discussed.

2.5.1 Hutchings Model

The Hutchings model was one of the pioneering researches conducted to develop the constitutive models for polymeric materials. To overcome the defect in Taylor's original derivation, which assumed the material to be "rigid-plastic" that is not applicable to most polymeric materials, Hutchings proposed a simplified "ideal elastic, perfectly-plastic" relationship to represent the dynamic behaviors of polymers by neglecting the strain rate effect [26]. Equations 2.26 and 2.27 together deliver the yield stress Y and yield strain ε_y:

$$(Y/\rho V^2) = \bar{C}_P/(\varepsilon_y - {\varepsilon_y}^2)[\tfrac{1}{1-\varepsilon} - (1-\bar{C}_P)/(1-\varepsilon_y)] \quad (2.26)$$

$$\varepsilon_y = \frac{\rho {V_c}^2/Y}{1+(\rho {V_c}^2/Y)} \quad (2.27)$$

where $$\bar{C}_P = [\varepsilon_y/(1-\varepsilon)]^{1/2} \quad (2.28)$$

$$\varepsilon = \frac{1}{8\varepsilon_y}\{(8{\varepsilon_y}^2 + 4k\varepsilon_y - k^2) + [(k^2 - 8{\varepsilon_y}^2 - 4k\varepsilon_y)^2 - 16\varepsilon_y(4{\varepsilon_y}^3 + 4k{\varepsilon_y}^2 + k^2\varepsilon_y - k^2)]^{\frac{1}{2}}\} \quad (2.29)$$

$$k = 1 - \frac{L}{L_0} \quad (2.30)$$

V_c is the critical velocity below which the deformation is purely elastic. V_c can be determined experimentally by plotting the line of plastic strain *vs.* impact velocity for a certain material, and the intercept with *x* axis is the value of V_c. After measurement of V_c, ρ, *V*, and *k*, the values of $\varepsilon_y$and *Y* can be determined by numerical methods with an initial estimation of ε_y.

The Hutchings model has been successfully applied to PC at high strain rate, and reasonable agreement between the predicted and experimental data was obtained [26]. One restriction of this model is its limitation only to polymeric materials with no fracture under impact loading or long-term relaxation after deformation.

2.5.2 Johnson-Cook Model

Johnson and Cook in 1983 developed a constitutive model subjected to large strains, high strain rates and high temperatures to a series of twelve metal materials based on the

torsion and tensile tests over a wide range of strain rates and temperatures [70]. The Johnson-Cook model, as shown in Equation 2.31, incorporated the effects of strain hardening, strain rate hardening, and thermal softening:

$$\sigma = [A + B\varepsilon^{n}][1 + Cln\dot{\varepsilon}^{*}][1 - T^{*m}] \tag{2.31}$$

where the von Mises flow stress, σ, is a function of equivalent plastic strain ε^{p}, dimensionless plastic strain rate $\dot{\varepsilon}$*, and homologous temperature T^{*} (Equations 2.32 - 2.33):

$$\dot{\varepsilon}^{*} = {\dot{\varepsilon}}/{\dot{\varepsilon}_{0}} \quad (\dot{\varepsilon}_{0} = 1.0s^{-1}) \tag{2.32}$$

$$T^{*} = \frac{T - T_{room}}{T_{melt} - T_{room}} \tag{2.33}$$

For the five material constants, *A* is the yield stress, *B* and *n* represent the strain-hardening effect, *C* is the strain rate constant, and *m* represents the thermal softening effect. The constants can be determined by fitting the Johnson-Cook model with various experimental curves at different conditions. To evaluate the Johnson-Cook model, data from the Taylor impact test on Armco iron, 4340 steel, and OFHC copper were compared with the simulation results, and all of them showed reasonable agreement [70]. As a relatively simple and robust constitutive model being able to describe and predict the dynamic behavior of materials in a wide range of strain rate, the Johnson-Cook model has been extensively applied to metal materials.

2.5.3 Zerilli-Armstrong Model

The Zerilli-Armstong constitutive model was proposed based on the thermally activated dislocation motion which expresses the flow stress of a material as the external forces overcoming both short-ranged thermally activated barriers ($\Delta\sigma_G$) and long-ranged athermal barriers ($\Delta\sigma_G{}'$) [71, 72]. The constitutive relation for *FCC* and *BCC* metals were formulated separately by considering the effects of strain hardening, strain-rate hardening, thermal softening and polycrystal grain boundaries (Equations 2.34 - 2.35):

$$\text{FCC: } \sigma = \Delta\sigma_G{}' + c_2\varepsilon^{1/2}\exp(-c_3T + c_4Tln\dot{\varepsilon}) + kl^{-1/2} \tag{2.34}$$

$$\text{BCC: } \sigma = \Delta\sigma_G{}' + c_1\exp(-c_3T + c_4Tln\dot{\varepsilon}) + c_5\varepsilon^n + kl^{-1/2} \tag{2.35}$$

where c_1, c_2, c_3, c_4, and c_5 are material constants, k represents the microstructural stress intensity, and l is the average grain diameter. The strain hardening effect is uncoupled from strain-rate hardening and thermal softening effects in the *BCC* case, and the latter dependencies are more sensitive in *BCC* metals.

The application of the Zerilli-Armstrong models on polymers was developed in 2007 [73]. An enhanced strain hardening effect with increasing strain at higher strain rates and pressure was accounted for in the model compared with metal deformation behaviors. The Zerilli-Armstrong model for polymers is composed of a viscoplastic component governed by Eyring's thermal activation theory and a viscoelastic component described by Maxwell-Weichert model. As illustrated in Figure 2.12, the Maxwell-Weichert model is a parallel connection of elastic spring and non-linear dashpot in series, and the total stress deviators are applied on both the viscoelastic and viscoplastic parts.

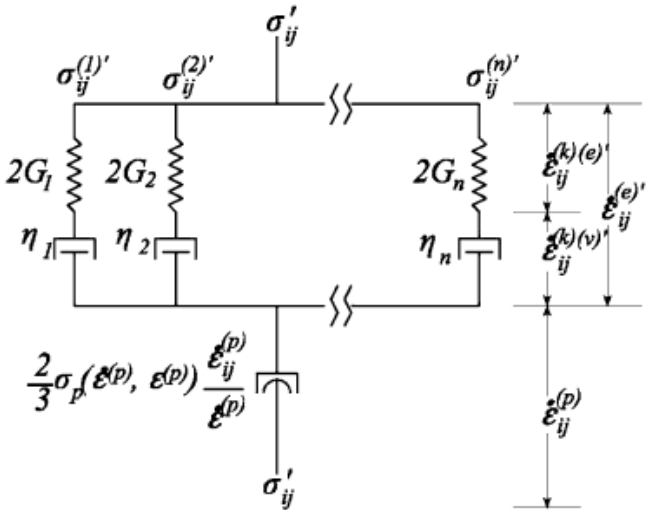

Figure 2.12. Maxwell-Weichert model description with linear viscoelasticity plus thermal activation non-linear viscoplasticity [73]

The applications of the Zerilli-Armstrong model on PTFE and PMMA for simulating their dynamic behaviors in a wide strain rate range have shown reasonable agreement with experimental results [73, 74].

2.5.4 Mulliken and Boyce Model

Mulliken and Boyce in 2006 proposed a three-dimensional strain rate dependent model to successfully describe and predict the strain rate and temperature dependent behaviors of PC and PMMA polymers [75]. The Mulliken and Boyce model comprises the contributions from different molecular motions under different frequency regimes. The one-dimensional interpretation of this model is shown in Figure 2.13. Segment B is a non-linear Langevin spring that represents the molecular network resistance to stretching and alignment. Segment A contains two sub-segments (α and β) in parallel, each with an

elastic spring connected to a viscoelastic dashpot in series, representing the intermolecular resistance to chain-segment rotation:

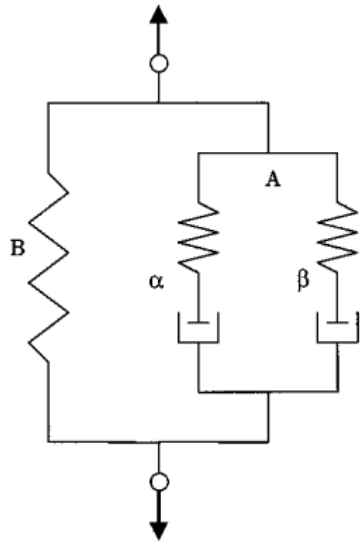

Figure 2.13. One-dimensional interpretation of the Mulliken and Boyce constitutive model [75]

The two sub-segments indicate two distinct thermally-activated processes associated with different molecular-level motions as described in the two-process Eyring yield model [40]. This model assumed that the α and β molecular processes were sufficiently de-coupled, so that the overall material response might be approximated as the simple superposition of the two.

2.5.5 Modified Johnson-Cook Model

Raftenberg M. N. and his coworkers [14] recently simulated the Taylor impact deformation of the PTFE / Al composite by using modified Johnson-Cook and PSDam strength models. The latter one was developed particularly for the PTFE / Al system at the Sandia National Labs, while the former one was based on the Johnson-Cook model

described in 2.5.2, and it defined the von Mises effective stress as a function of plastic strain, plastic strain rate and temperature (Equation 2.36):

$$\sigma_{JCP}\left(\varepsilon^{p},\theta,\dot{\varepsilon}\right)=\left[\hat{A}\left(\dot{\varepsilon}\right)+\hat{B}\left(\dot{\varepsilon}\right)\cdot\left(\varepsilon^{p}\right)^{\hat{N}\left(\dot{\varepsilon}\right)}\right]\left(\frac{\theta_{m}-\theta}{\theta_{m}-\theta_{r}}\right) \tag{2.36}$$

By comparing Equation 2.36 with the original Johnson-Cook model in Equation 2.31, the second bracket in Johnson-Cook model describing strain rate dependency is not presented in Equation 2.36, while the material constants *A*, *B*, and *n* in Johnson-Cook model are modified to $\hat{A}(\dot{\varepsilon})$, $\hat{B}(\dot{\varepsilon})$ and $\hat{N}(\dot{\varepsilon})$, which are all functions of strain rate $\dot{\varepsilon}$. In this sense, the modified Johnson-Cook model combines the strain hardening and strain rate hardening effects into one term shown in the first bracket of Equation 2.36. The second bracket in Equation 2.36 is the same as the original one, describing the thermal softening effect. The modified Johnson-Cook model introduces seven material constants: A_0, A_1, B_0, B_1, N_0, N_1 and θ_m, which are determined by fitting the model with Instron and SHPB data at two different strain rates. The simulation results of the Taylor impact test by incorporating the modified Johnson-Cook model represented the experimental results quite well at low impact velocities. However, at higher impact velocities, the simulation results started to deviate from the experimental data, which could be attributed to the interior structural change of the sample and/or the chemical reactions taking place upon impact. Due to the similarity between the composite system in this thesis work (PTFE 7A / Ti) and the one studied by Raftenberg et al. (PTFE / Al), the modified Johnson-Cook model was beneficially applied to the former, and the deformation process of the Taylor impact test was simulated prior to any chemical reaction taking place. The elaboration of this model and simulation results are presented in detail in Chapter V.

CHAPTER III

POLYTETRAFLUOROETHLYENE (PTFE) 7A / TITANIUM (TI) COMPOSITE SYSTEM

As an example of a polymer / reactive metal composite system, PTFE 7A and Ti were chosen to form composite systems with different constitutions and configurations for high strain rate tests. The materials were chosen due to the high reactivity of the Ti element and the superior physical / thermal properties of the PTFE polymer. In this chapter, the processing procedures for preparing the PTFE 7A / Ti composite systems will be described in detail followed by a series of characterizations to study their thermal, chemical and mechanical properties.

3.1 Materials

Teflon® PTFE 7A particles were obtained from the *E. I. DuPont Company* as white powders. One type of Teflon® fluoropolymer resin product with high bulk density applied to large moldings, or used as a filler to modify the mechanical properties of moldings, PTFE 7A, also possesses the superior properties of typical fluoropolymer resins: inertness to most chemicals, low friction, outstanding dielectric properties and stability in a wide temperature range (~240 ℃ to ~260 ℃). Some of the important material property data are listed in Table 3.1:

Table 3.1. Typical property data for Teflon® PTFE 7A

Property	Value
Average bulk density (g/L)	460
Average particle size (μm)	34
Melting temperature (℃)	342
Glass transition temperature (℃)	250
Tensile strength (MPa)	34.5
Elongation at break (%)	375

Titanium particles (99%, metal basis) were obtained from *Alfa Aesar* as dark grey powders. Some of the important Ti material property data are listed in Table 3.2:

Table 3.2. Typical property data for Titanium powders

Property	Value
Density at 20 ℃ (g/cm^3)	4.507
Average particle size (μm)	43
Melting temperature (℃)	1668
Boiling temperature (℃)	3260
Ignition temperature (℃)	250

3.2 Fabrication and Processing of PTFE 7A / Ti Composite

The preparation of PTFE 7A / Ti composites included the steps of mixing, pressing and sintering:

(1) The PTFE 7A / Ti mixtures were prepared in three different ways: (a) 51 wt% PTFE 7A and 49 wt% Ti, with Ti aggregated in a PTFE 7A matrix (Batch #1); (b) 51wt% PTFE 7A and 49 wt% Ti, well mixed (Batch #2); (c) 32.4 wt% PTFE 7A and 67.6 wt% Ti, well mixed (Batch #3, equal volume). The non-uniform mixture was prepared by

mixing PTFE 7A and Ti powders in a low-speed *V*-shaped blender for 24 hours, and the uniform mixture were made by first stirring the sticky and soft PTFE 7A powders well and then mixing the two components in the low-speed *V*-shaped blender for 24 hours.

(2) The mixture was then statically pressed in dies with different diameters by a 20,000 lb hydraulic press machine to mold them into short cylindrical rods. The sample sizes of four different dimensions are shown in Table 3.3:

Table 3.3. Sample sizes of four different dimensions

Sample dimension	Diameter (mm)	Length (mm)
Large	~7.49	~19.83
Medium	~6.38	~3.79
Small	~3.19	~3.39
Even smaller	~3.19	~1.46

(3) The sample rods were heated under an Argon (Ar) environment to the soak temperature of PTFE 7A at 300 ℃ for 6 hours, heated to the melting temperature of PTFE 7A at 357 ℃ for another 6 hours, and finally cooled to room temperature [74]. The composite densities and Theoretical Maximum Density (TMD) are listed in Table 3.4:

Table 3.4. Density and %TMD of PTFE 7A / Ti composite in three batches

Batch	Density (g/cm^3)	% TMD
#1	~2.81	~97%
#2	~2.90	~100%
#3	~3.32	~99.7%

3.3 PTFE 7A / Ti Composite Configuration

PTFE 7A powders, titanium powders and PTFE 7A / Ti composites with three different configurations were characterized after pressing by Scanning Electron Microscopy (SEM). The medium-sized pressed samples were gold coated by using an *ISI Sputter Coater* and imaged by a *Hitachi S800* field emission gun operating at 12 / 10 kV.

As shown in the SEM images of Ti (Figure 3.1 a - b) pressed powders and original PTFE 7A (Figure 3.1 c - d), the pressed PTFE 7A had a smooth morphology, while pressed Ti showed obvious voids between particles. In the Batch #1 sample composite (Figure 3.1 e - f), the dark region represents PTFE 7A matrix, and the white region refers to the Ti component. Compared with Batch #2 (Figure 3.1 g - h) and Batch #3 (Figure 3.1 i - j) sample composites, the Ti component in Batch #1 was distributed in a more aggregated way in the PTFE 7A matrix.

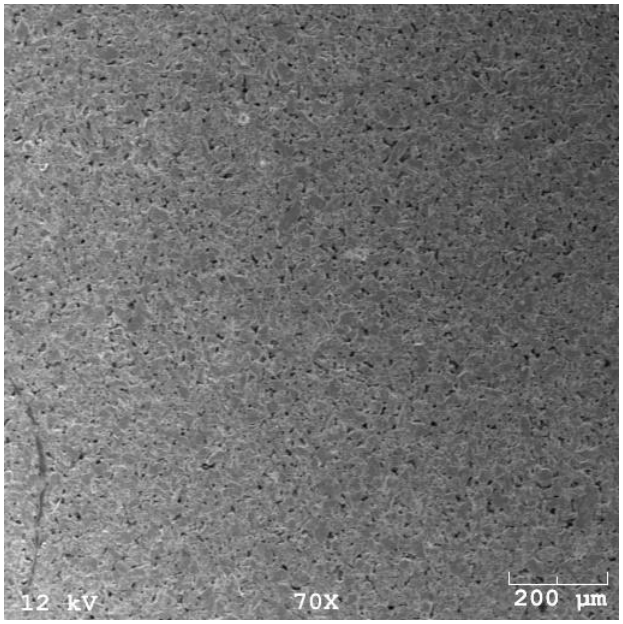

(a)

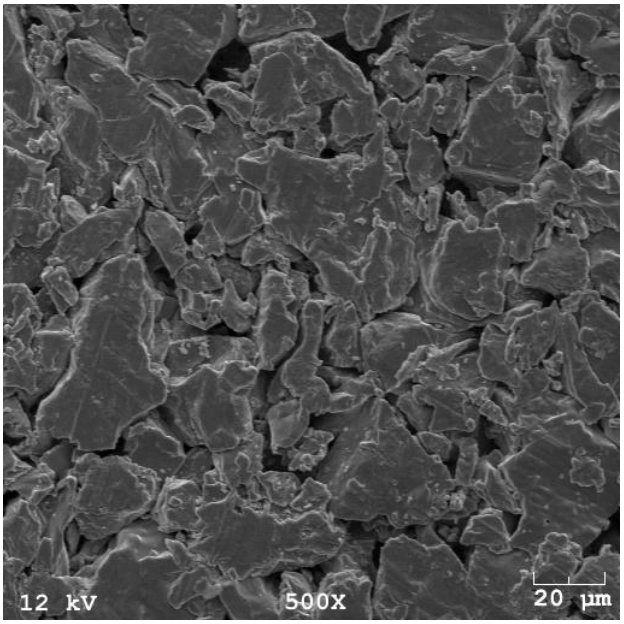

(b)

Figure 3.1. SEM images of (a) - (b) Ti powders after pressing; (c) - (d) PTFE 7A powders after pressing; (e) - (f) PTFE 7A (51 wt%) / Ti (49 wt%) composite with non-uniform distribution; (g) - (h) PTFE 7A (51 wt%) / Ti (49 wt%) composite with uniform distribution; (i) - (j) PTFE 7A (32.4 wt%) / Ti (67.6 wt%) composite with uniform distribution

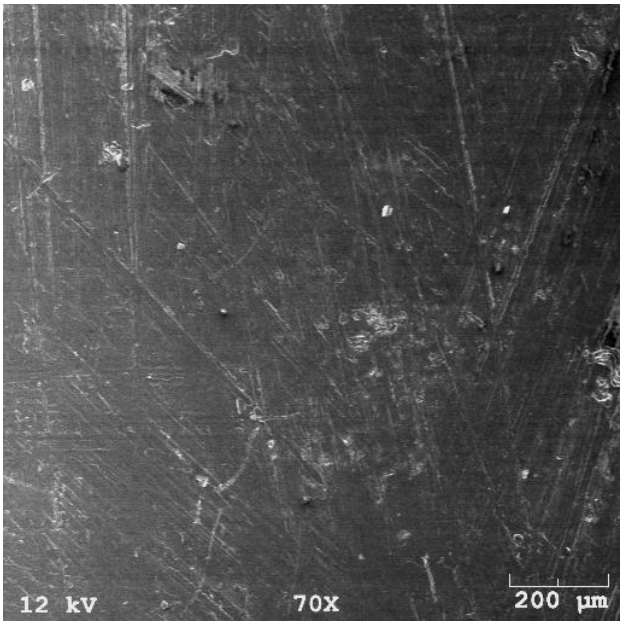

(c)

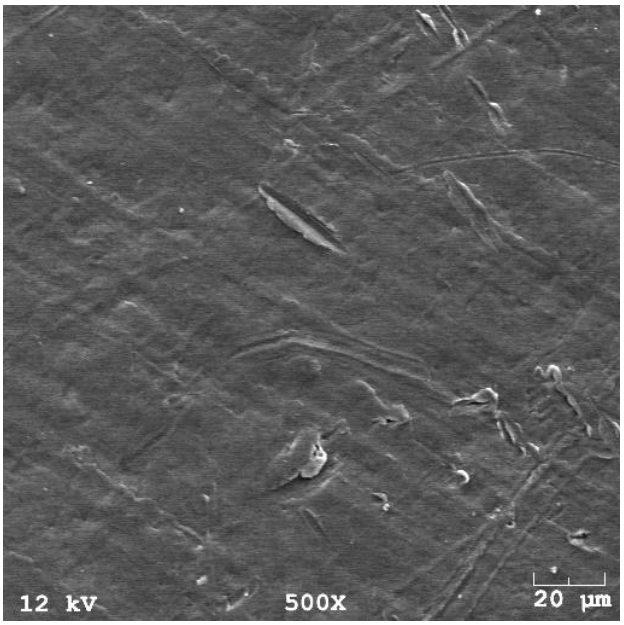

(d)

Figure 3.1. Continued

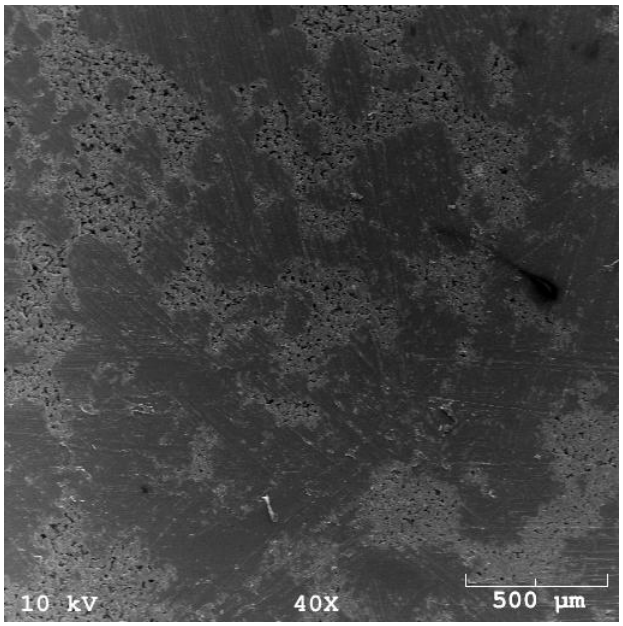

(e)

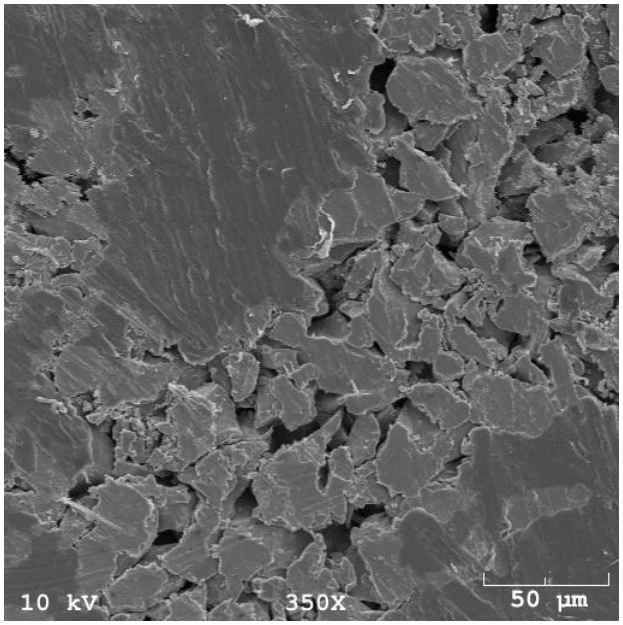

(f)

Figure 3.1. Continued

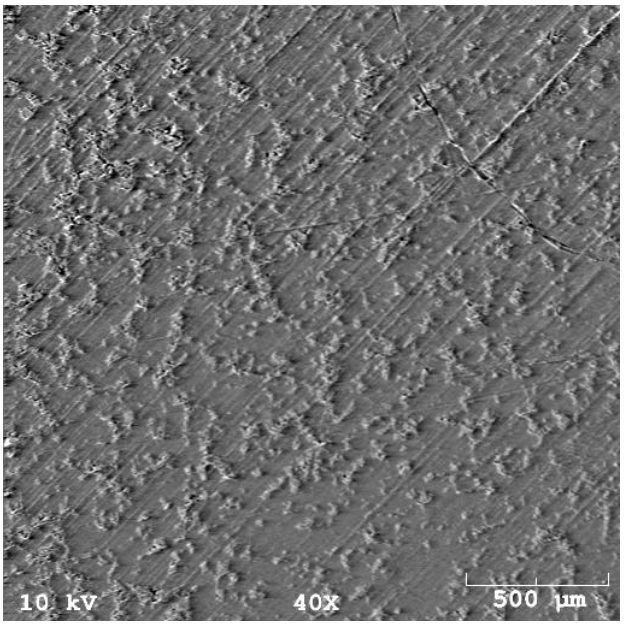

(g)

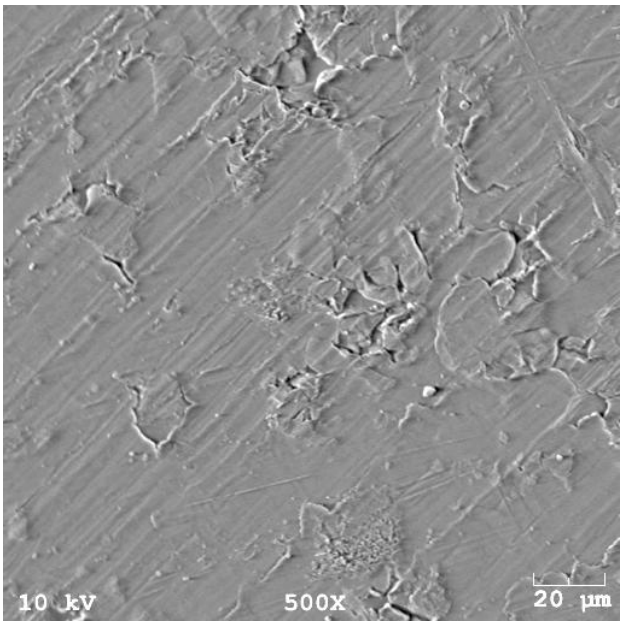

(h)

Figure 3.1. Continued

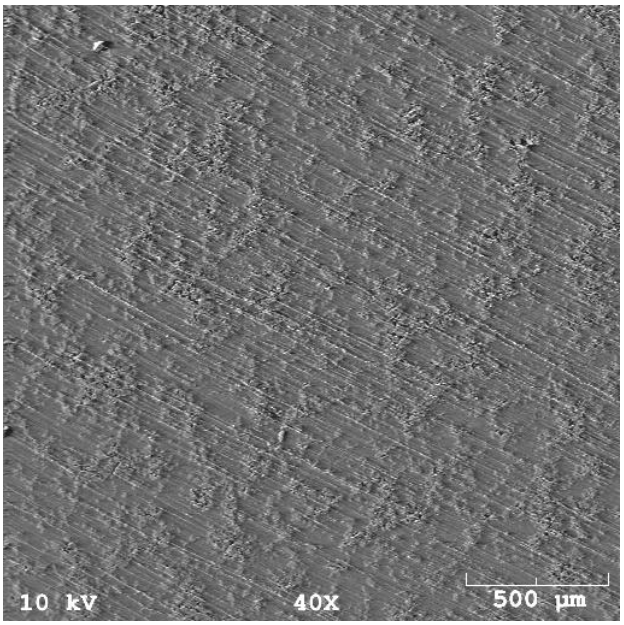

(i)

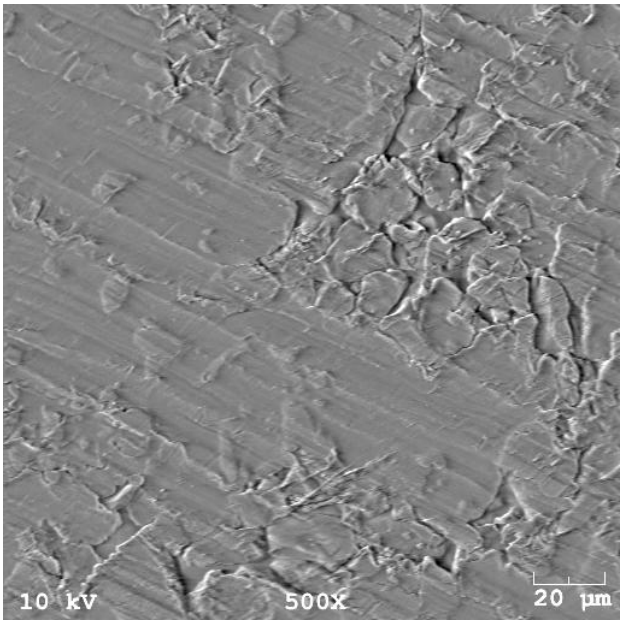

(j)

Figure 3.1. Continued

3.4 Characterization of PTFE 7A / Ti Composites

3.4.1 Thermal Analyses

Before conducting high strain rate tests on the PTFE 7A / Ti composites, the pure chemical reaction mechanism behind these two materials with only heat provided was investigated. PTFE 7A / Ti (Batch #1) composite was first analyzed by Differential Thermal Analysis (DTA) (*Perkin-Elmer DTA7*) from room temperature to 1400 ℃ under an Argon environment at three different flow rates: 2 ℃/min, 10 ℃/min and 50 ℃/min. The DTA curves are shown in Figure 3.2 for both pure PTFE 7A and PTFE 7A / Ti (Batch #1) composite:

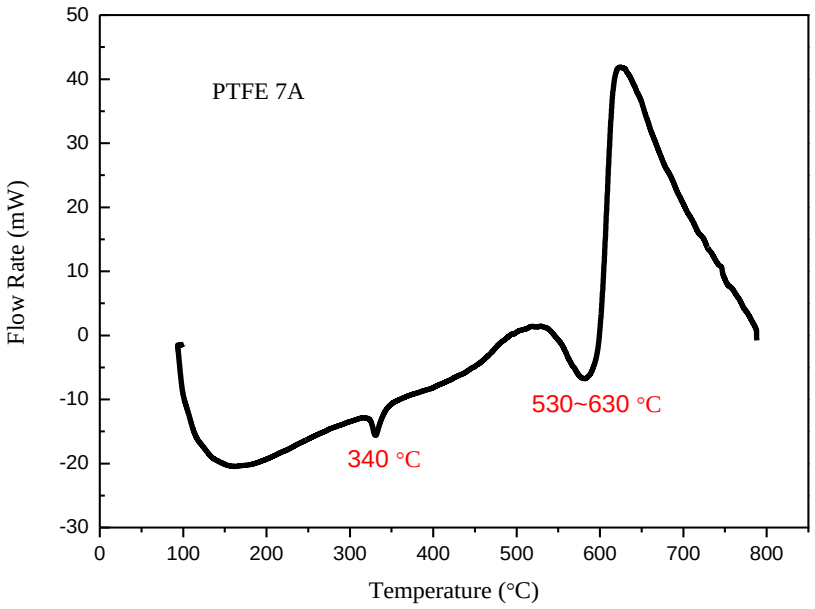

(a)

Figure 3.2. DTA curves of (a) PTFE 7A and (b) PTFE 7A / Ti composite at three different heating rates: (a) at 2 ℃/min; (b) at 10 ℃/min; (c) at 50 ℃/min

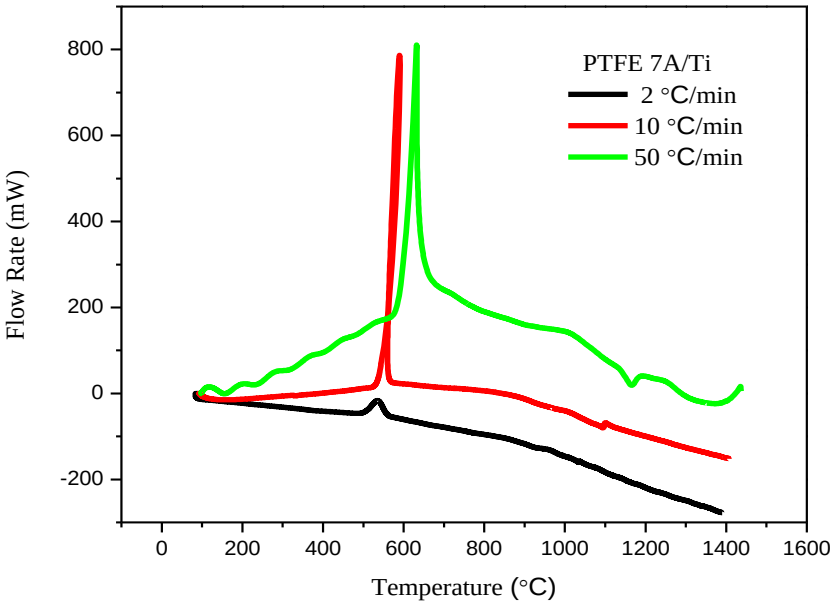

(b)

Figure 3.2. Continued

For pure PTFE 7A, the melting stage gave a small endothermic trough at around 340 ℃, which was then followed by a large decomposition endothermic trough starting at 530 ℃ and ending at 630 ℃. The DSC thermal decomposition behavior of PTFE has been studied by Ksiqzczak [76], and they observed one small exothermic peak from 547 to 564 ℃, then a large endothermic trough from 602 to 647 ℃. However, the small exothermic peak mentioned in their paper was not obvious in Figure 3.2 (a). For the PTFE 7A / Ti composite, one large exothermic peak representing chemical reaction between PTFE 7A and Ti occurring at 500 ℃ overshadowed all other small variations in the DTA curves due to the massive amount of heat released from the reaction. Since the temperature range for PTFE 7A degradation overlapped with that for the reaction, it was

assumed that this chemical reaction involved: (1) the degradation of PTFE 7A; (2) the reaction between Ti and the products from PTFE 7A degradation. As indicated in the DTA curves with different flow rates, the exothermic peak became larger and more evident with the increase in flow rate. The low flow rate enabled the PTFE 7A degradation products to react slowly and steadily with Ti, thus forming smaller exothermic peaks in DTA curves compared with the larger ones formed in a more intensive way at higher flow rates.

3.4.2 XRD Identification After Heating

The post-DTA solid products were then collected for XRD (*X'Pert PRO Alpha-1*) analysis. Figure 3.3 shows the XRD patterns of the products at three different flow rates:

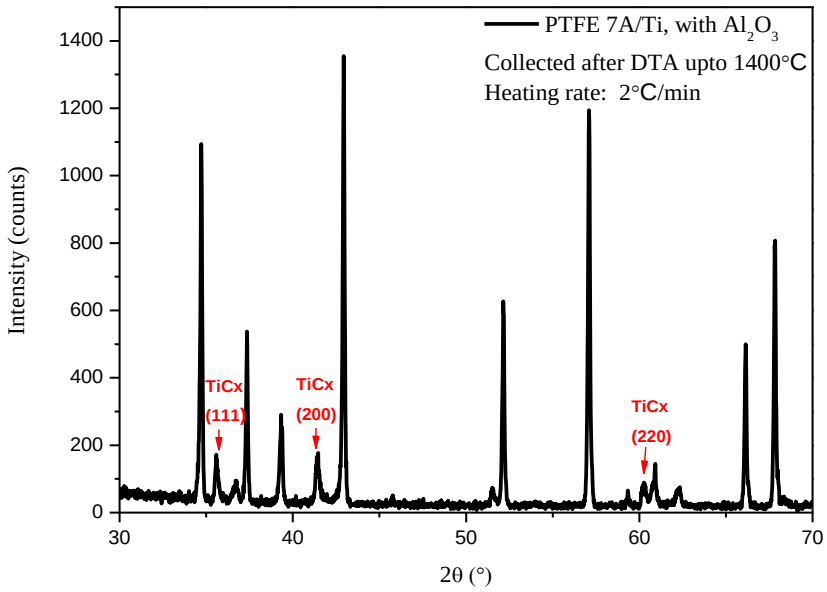

(a)

Figure 3.3. XRD patterns of the PTFE 7A / Ti composite collected after DTA test at three different heating rates: (a) at 2 ℃/min; (b) at 10 ℃/min; (c) at 50 ℃/min

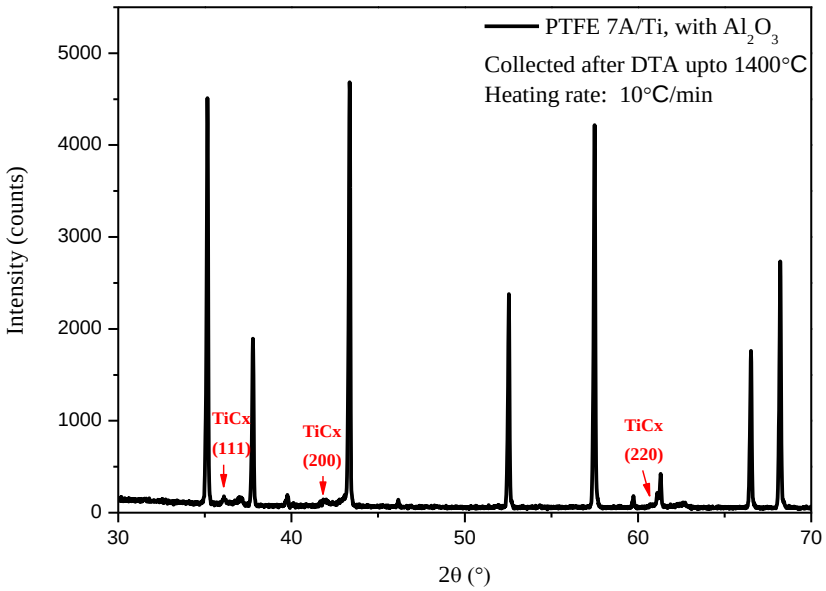

(b)

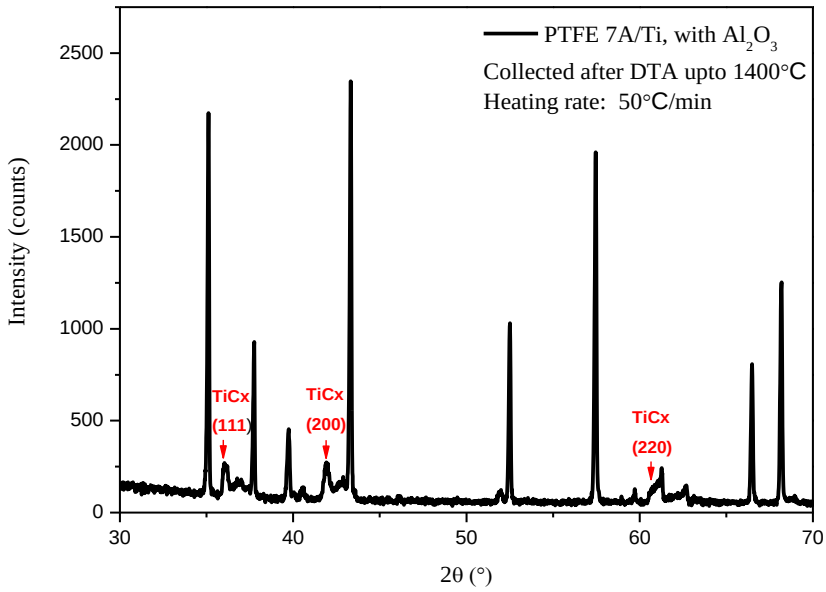

(c)

Figure 3.3. Continued

The patterns were first analyzed through the 'search / match' function in the *Jade 8.0* software, by which TiC_x (marked in red) and Al_2O_3 phases were identified as the most prominent peaks. Since Al_2O_3 powders were used as reference in the DTA test, they could not be removed from the final products. As shown in Figure 3.4(a), TiC_x has a NaCl-type *FCC* structure, with two *FCC* ions interpenetrating with each other:

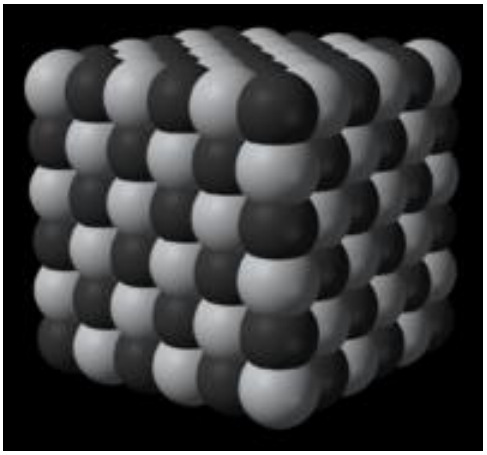

(a)

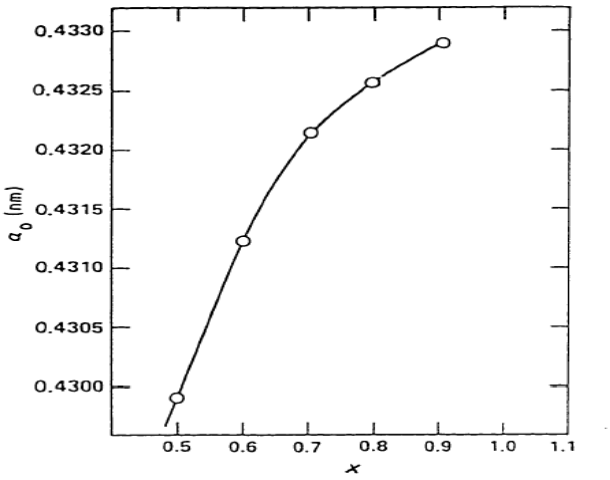

(b)

Figure 3.4. (a) The crystal structure of TiC_x; (b) The variation of the lattice parameter of TiC_x with stoichiometry, observed from combustion synthese of Holt and Munir [58]

The three most intensified peaks of TiC_x were fitted with a Lorentzian curve fit, and then the lattice constant a of TiC_x corresponding to each peak was calculated by using Equation (3.1), where θ and m could be determined from the position of peaks (2θ) and the plane indices (*hkl*). An average a was taken among three peaks for each flow rate:

$$sin^2\theta = \frac{\lambda^2}{4a^2}m \tag{3.1}$$

Based on the relationship between lattice constant a and C/Ti ratio in TiC_x, the x value corresponding to certain a could be determined by checking the plot in Figure 3.4(b). All of the lattice parameters a and x values at different flow rates are listed in Table 3.5:

Table 3.5. The lattice parameters of PTFE 7A / Ti composite reaction products after heating at different heating rates

Flow rate (℃/min)	2θ (°)	Lattice indices (*hkl*)	Lattice constant (*Å*)	Average *a* (*Å*)	*x* (C/Ti)
2	35.597	(111)	4.3648	4.353	close to 1
	41.425	(200)	4.3559		
	60.283	(220)	4.3389		
10	36.105	(111)	4.3054	4.3054	0.54
	41.949	(200)	4.3039		
	60.780	(220)	4.3063		
50	36.097	(111)	4.3063	4.3065	0.55
	41.943	(200)	4.3045		
	60.750	(220)	4.3087		

Results in Table 3.5 suggested that the lattice parameter a and x value (or C/Ti ratio) were highly dependent on flow rate. As the flow rate increased from 2 to 10 ℃/min, the average lattice parameter a decreased about 10%, and the C/Ti ratio decreased dramatically from almost 1 to 0.54. However, with the further increase of flow rate, the

lattice size and C/Ti ratio changed little, apparently due to the effect of flow rate on reaction dynamics. Heating under low flow rate tended to drive the reaction to completeness, yielding the TiC_x with larger crystal size and better crystal structure.

3.4.3 Quasi-Static Compression Test

The chemical reaction between PTFE 7A and Ti, as well as the main product TiC_x, was verified through DTA analysis and XRD identification. The next step was to test its mechanical properties under different strain rates without triggering the chemical reaction.

Stress *vs.* strain curves in Figure 3.5 were obtained from Instron test (*Instron Corporation compression testing machine 5566* with a 10KN load cell) with strain rate changing from 0.0001 to 0.1 s^{-1}:

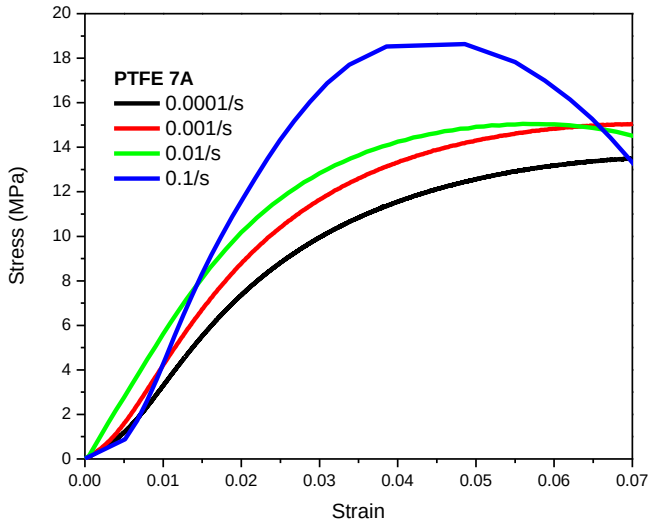

(a)

Figure 3.5. Stress *vs.*strain curves obtained from Instron test for (a) PTFE 7A and (b) PTFE 7A / Ti composite with strain rate ranging from 0.0001 s^{-1} to 0.1 s^{-1}(Batch #2)

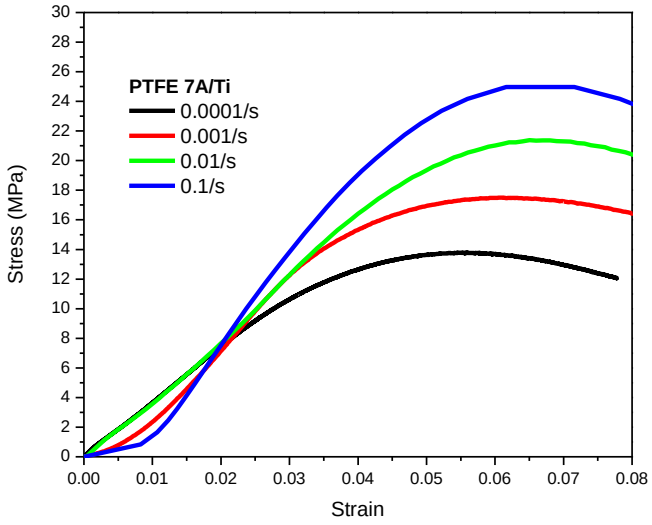

(b)

Figure 3.5. Continued

For both the PTFE 7A and the PTFE 7A / Ti (Batch #1) composite, yield stress increased with increasing strain rate, and that of the PTFE 7A / Ti composite was higher than for pure PTFE 7A, especially at higher strain rates (> 0.01 s^{-1}). Except for the instability in the initial stage at 0.1 s^{-1}, Young's modulus also increased with strain rate. This phenomenon was widely observed in many different types of materials and has been explained in detail in Section 2.3. The yield stress of the PTFE 7A / Ti composite reached 25 MPa at 0.1 s^{-1}, while that of pure PTFE 7A at 0.1 s^{-1} was less than 19 MPa. The mechanical properties of the PTFE 7A / Ti composite should have exceeded that of the pure PTFE 7A, since metal Ti was incorporated in the system.

3.4.4 SHPB Test

SHPB tests with strain rate ranging from ~ 2000 to ~ 3000 s^{-1} were performed on the PTFE 7A / Ti (Batch #2) composite (Figure 3.6).

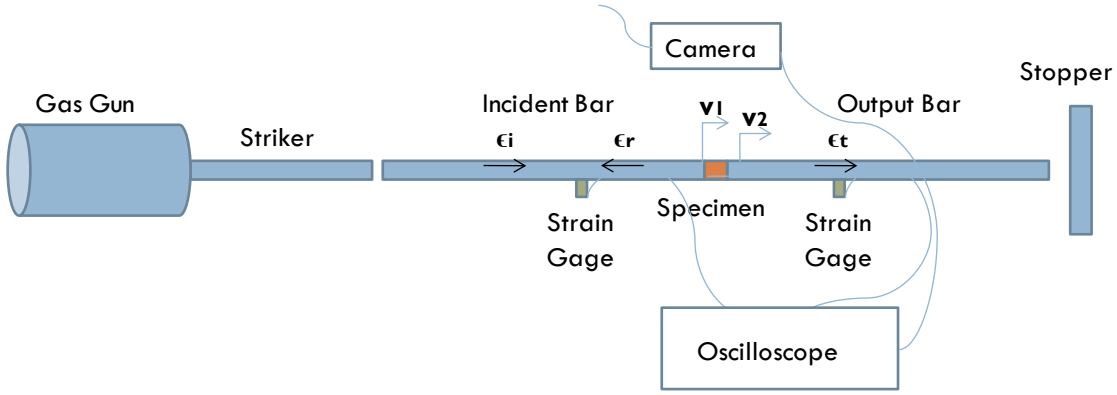

Figure 3.6. Experimental setup for SHPB test in compression mode

Stress *vs.* strain curves obtained from the SHPB test with strain rates ranging from ~ 2000 to ~ 3000 s^{-1} exhibited more instability than in the Instron test due to the higher strain rates involved and adiabatic heat generated during compression (Figure 3.7):

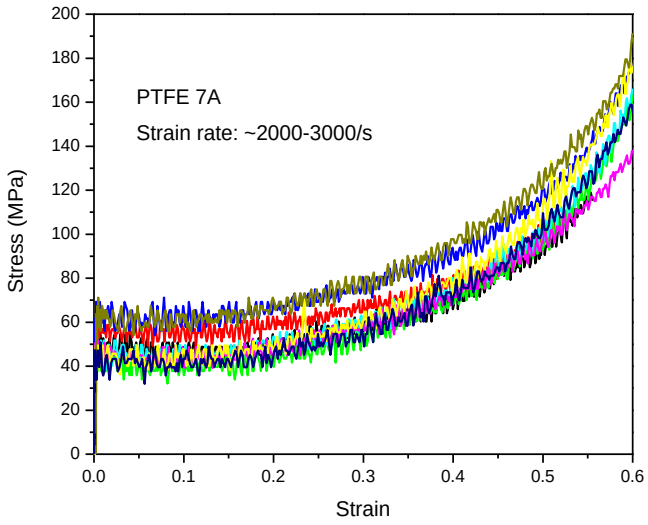

(a)

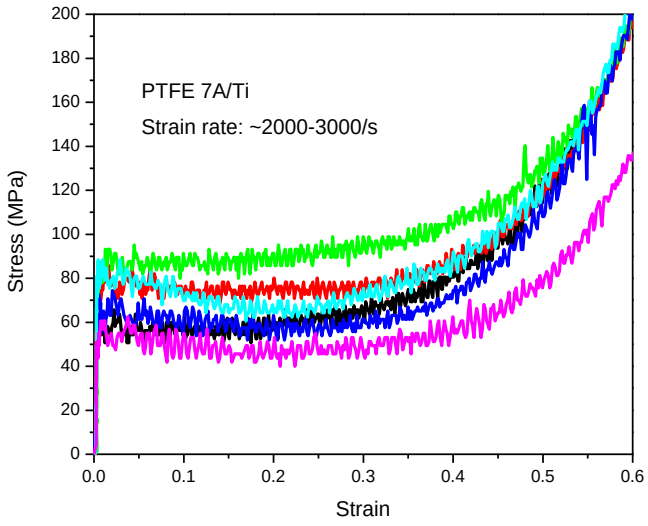

(b)

Figure 3.7. Stress *vs.* strain curves obtained from SHPB test for (a) PTFE 7A; (b) PTFE 7A / Ti composite; (c) comparison plots at strain rate of ~ 3100 s^{-1}

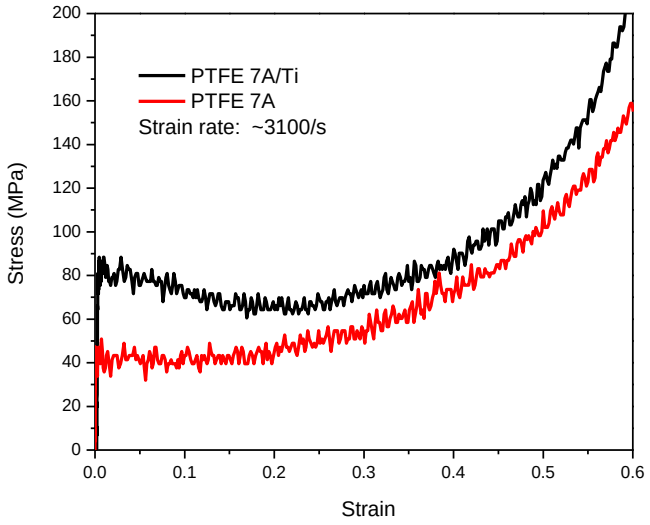

(c)

Figure 3.7. Continued

A series tests at various strain rates therefore did not exhibit an apparent trend as in the Instron test, although the stress *vs.* strain curve is highly strain rate-sensitive. Within the strain rate ranging from 2000 to 3000 s^{-1}, the yield stress of pure PTFE 7A varied from 40 to 60 MPa, while that of the PTFE 7A / Ti (Batch #2) composite varied from 50 to 90 MPa, which was much higher and also more strain rate-sensitive than for pure PTFE 7A. One pair of selected stress *vs.* strain curves at ~3100 s^{-1} (Figure 3.7 (c)) clearly illustrated the difference between PTFE 7A and the PTFE 7A / Ti composite at high strain rate.

3.4.5 Post-SHPB Characterization by XRD Analysis

The deformed samples after the SHPB test were collected for XRD analyses (Figure 3.8):

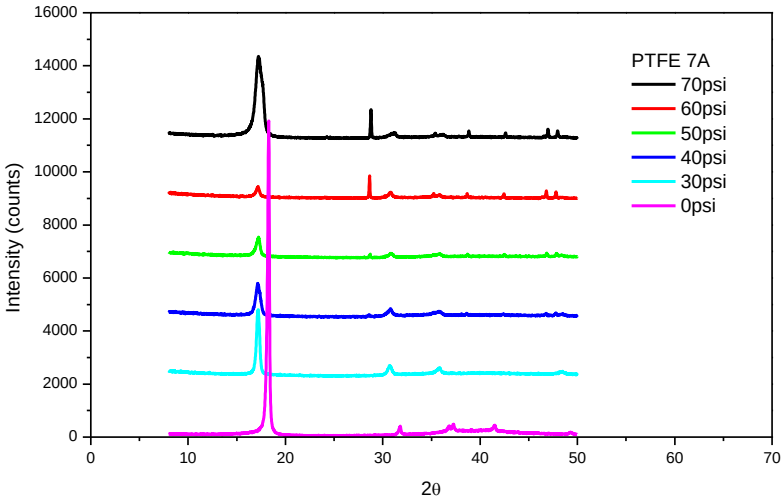

(a)

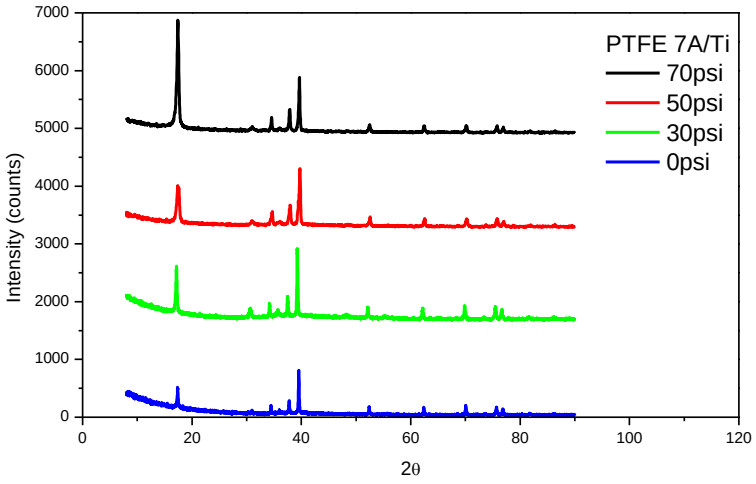

(b)

Figure 3.8. XRD analyses of post-SHPB samples: (a) PTFE 7A (b) PTFE 7A / Ti composite under different compression pressures

As referred to the literature [77], the typical trace of PTFE 7A has a strong crystalline (110) peak at around 18 ° and amorphous halo in the range of 30 - 50 °, indicated by the pattern that was under 0 psi pressure at the bottom of the XRD chart (Figure 3.8(a)). With the increase of impact pressure from 30 to 70 psi, the crystalline peaks moved to lower 2θ values, suggesting that residual strains remained in the crystals produced by impact compression. In addition, the amorphous phase diminished with increasing pressure, while an additional crystalline peak appeared at around 28 ° under 50 psi, increasing in intensity with increasing pressure. The new peak was due to the diffraction of a new crystalline plane attributed to the strain-induced crystallization process.

For the post-SHPB PTFE 7A / Ti (Batch #2) composite, no evidence from XRD patterns showed the introduction of new compound, indicating that the impact energy did not reach the level of activation energy for chemical reaction to occur. Comparing the four XRD patterns shown in Figure 3.8(b) at different impact pressures, little difference was observed except for the stronger crystalline (110) peak with increasing impact pressure, nor did new peaks appear at higher pressures. The incorporation of Ti in PTFE 7A apparently hindered the generation of a new crystalline plane of PTFE 7A at around 28 °, whereas it promoted the growth of existing crystalline phases.

3.5 Summary

PTFE 7A / Ti composites were prepared in three different configurations by following the described mixing, pressing and sintering procedures. The composite systems were characterized by DTA thermal analysis using different heating rates, and the chemical reaction between the two components followed the steps of: (1) PTFE 7A

decomposition, and (2) reaction between Ti and the PTFE 7A degradation products. By conducting the XRD analysis on post-DTA samples, the main reaction product was identified as the compound TiC_x, and the *x* value increased dramatically to approach one as the heating rate decreased, suggesting that a slow heating rate could lead to a more thorough reaction and a product with an improved crystal structure.

Mechanical tests with different strain rates were also carried out on the PTFE 7A / Ti composites by Instron (0.0001 to 0.1 s^{-1}) and SHPB (~ 2000 to ~ 3000 s^{-1}) techniques. As compared with the pure PTFE 7A sample, the yield stress and Young's modulus of the PTFE 7A / Ti composites had higher values due to the incorporation of Ti particles. The yield stress increased as the strain rate increased for both the PTFE 7A and PTFE 7A / Ti composites.

Post-SHPB samples (both PTFE 7A and PTFE 7A / Ti composites) were analyzed by XRD under different compression pressures. For the PTFE 7A sample, a new crystalline peak formed at around 28 ° as compression pressure increased to 60 psi, which was assumed to be a strain-induced crystallization process. For the PTFE 7A / Ti composites, only the strong PTFE 7A (110) crystalline peak was observed as compression pressure increased, and no other new crystalline peak was found.

CHAPTER IV

EXPERIMENTAL INVESTIGATION OF TAYLOR IMPACT TEST ON PTFE 7A / TI COMPOSITES

4.1 Overview

Although the Taylor impact test has been used extensively to study the dynamic behaviors and validate constitutive models for metallic materials at high strain rates in combination with numerical simulations, reports on the high strain rate behaviors of polymeric materials by using the Taylor impact test are rare. PC [78], PEEK [18], PE [79] and some polymer / metal composite systems [80, 81] have been investigated through the Taylor impact or reverse Taylor impact tests [82] to observe their deformation and fracture phenomena, build wave propagation structures and study their complicated viscoelastic-plastic constitutive behaviors.

As a semicrystalline polymer with desirable physical and chemical properties, PTFE has attracted particular attention due to its high strain rate behaviors compared with other polymers. A ductile to brittle transition was detected in a narrow velocity range by the Taylor impact test, which was considered to be related to the Phase II to III transition of PTFE [83-85].

In this study, Taylor impact tests were carried out on large, medium, small, and even smaller dimension samples from three PTFE 7A / Ti batches with the impact

velocity from ~ 90 to ~ 500 m/s. The influences of sample dimension, sample configurations, and impact velocity were also investigated.

4.2 Experimental

Taylor impact tests were performed by using a Helium driven gas gun with a diameter of 0.3 inches. The experimental setup is illustrated in Figure 4.1:

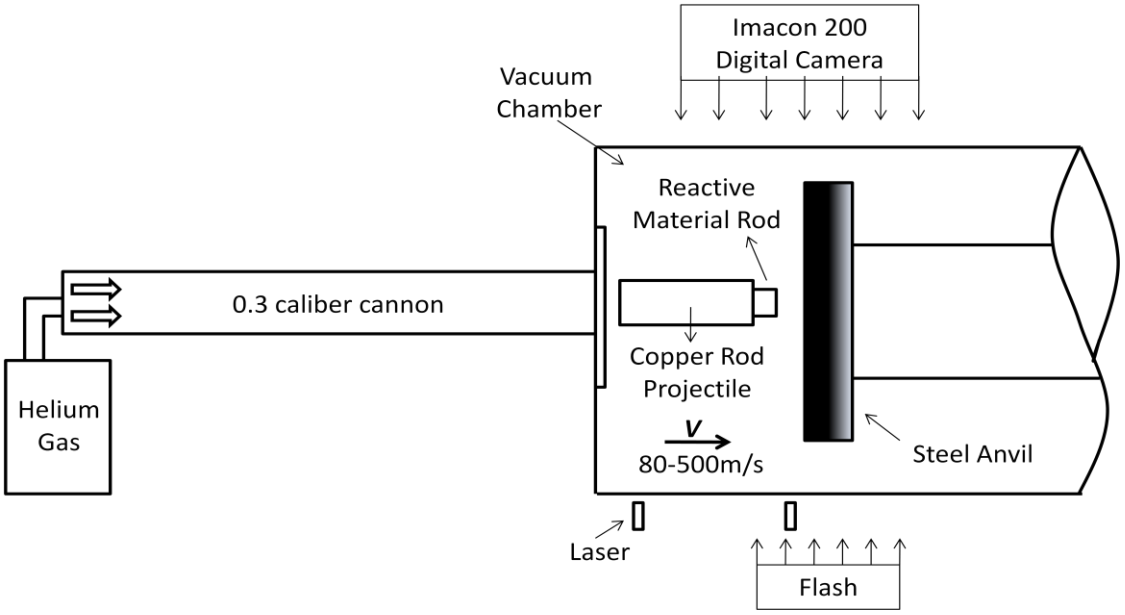

Figure 4.1. Schematic diagram of Taylor impact test setup

The cylindrical-shaped projectile was propelled by high pressure Helium gas with the impact velocity up to about 400 m/s, hitting onto a hardened steel anvil inside the vacuum chamber. The impact and deforming processes of the projectile were taken by an *Imacon 2000* digital camera that captured 16 images with the speed of 200 million frames per

second. The camera exposure time was set as 500 ns for all the experiments, and the inter-frame time was set as 1 μs, 1.5 μs, 1.75 μs, etc., based on the impact velocity. The velocity of the projectile was calculated by a laser measurement system that also triggered the start of the camera. Samples with medium, small and even smaller dimensions were attached onto a copper rod with a diameter of ~ 0.3 inches to form a projectile for launching. The sample with the larger dimension was propelled directly through the cannon. Steel dies of different sizes were used for molding and pressing PTFE 7A / Ti composites into cylindrical rods.

4.3 Results and Discussion

Table 4.1 summarizes the Taylor impact test results for the PTFE 7A / Ti composite from three different batches with four different dimensions, and at different impact velocities ranging from ~ 100 m/s to ~ 500 m/s:

Table 4.1. Summary of Taylor impact test results

	Batch #1 51 wt% PTFE 7A / 49 wt% Ti non-uniform			Batch #2 51 wt% PTFE 7A / 49 wt% Ti uniform			Batch #3 32.4 wt% PTFE 7A / 67.6 wt% Ti uniform		
Sample Dimension	Impact velocity (m/s)	Ignition time (μs)	Reaction severity	Impact velocity (m/s)	Ignition time (μs)	Reaction severity	Impact velocity (m/s)	Ignition time (μs)	Reaction severity
Medium	118	46.5	Reaction light	100	-	No reaction	89	45	Fume
Medium	135	35	Reaction light	201	24.75	Fume	205	22.5	Fume
Medium	156	25	Reaction light	304	20	Fume	281	20	Fume, reaction light
Medium	189	22.5	Reaction light	396	13.5	Fume	408	10.5	Fume, reaction light
Medium	308	20	Reaction light	-	-	-	-	-	-
Small	309	14	Reaction light	99	-	No reaction	91	36	Reaction light
Small	-	-	-	199	20.25	Reaction light	201	20.25	Reaction light
Even smaller	300	8	Reaction light	102	18	Fume, reaction light	101	12	Reaction light
Even smaller	-	-	-	203	15.75	Reaction light	204	9	Reaction light
Large	-	-	-	496	-	No reaction	498	-	No reaction

Ignition time was defined as the frame time of the first image detecting the reaction light or fume triggered by the energy deposited by impact loading. For all the three batches with medium, small and even smaller dimensions, either ignition light or ignition fume was detected under certain range of impact velocities.

In the next three subsections, Taylor impact tests on PTFE 7A / Ti composites from three batches will be separately discussed. In the fourth subsection, a film reduction method was applied on large dimension samples to extract the information of stress, strain and strain rate during impact process. In the fifth subsection, a comparison was made to elucidate the influences of impact velocity, sample dimension and sample configuration on the impact-initiated reaction.

4.3.1 PTFE 7A (51 wt%) / Ti (49 wt%) Composite (Batch #1) with Non-Uniform Distribution

Taylor impact test were conducted on the PTFE 7A / Ti composite (Batch #1) of three different sizes: medium dimension, small dimension and even smaller dimension. In all of the three cases, composite samples were attached to copper rods with similar dimensions. For each specific size, a series of impact tests with different impact velocities were performed.

4.3.1.1 Medium Dimension

Figures 4.2 - 4.5 demonstrate the transient images of the Taylor impact tests in tens of micro seconds at the impact velocity from ~ 100 m/s to ~ 300 m/s, and the approximate time corresponding to each frame was labeled within each image:

.

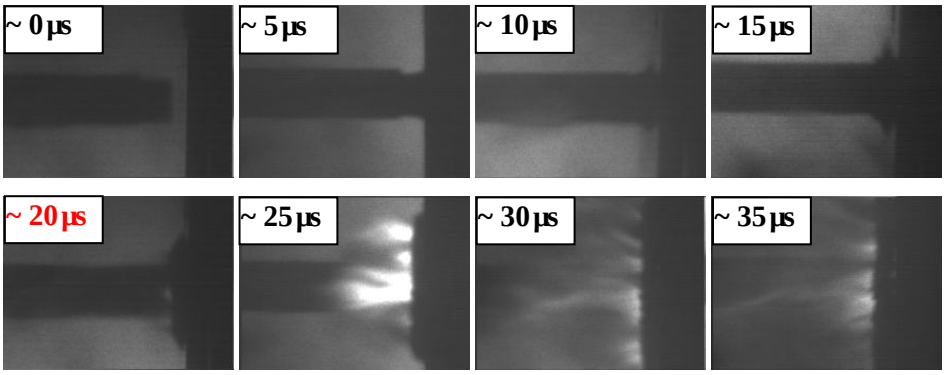

Figure 4.2. Consecutive images of the Taylor impact test on PTFE 7A / Ti composite (Batch #1, medium size), V_i = 308 m/s, the exposure time t_{exp} = 500 ns, and the interframe time t_{int} = 2 µs

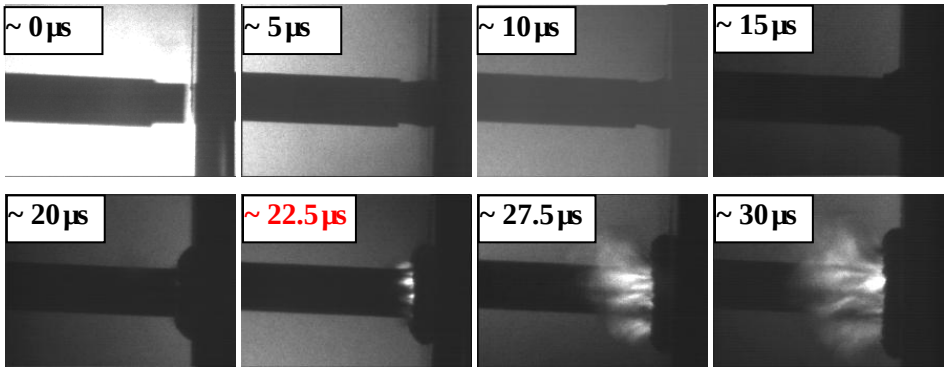

Figure 4.3. Consecutive images of the Taylor impact test on PTFE 7A / Ti composite (Batch #1, medium size), V_i = 188.73 m/s, t_{exp} = 500 ns, and t_{int} = 2 µs

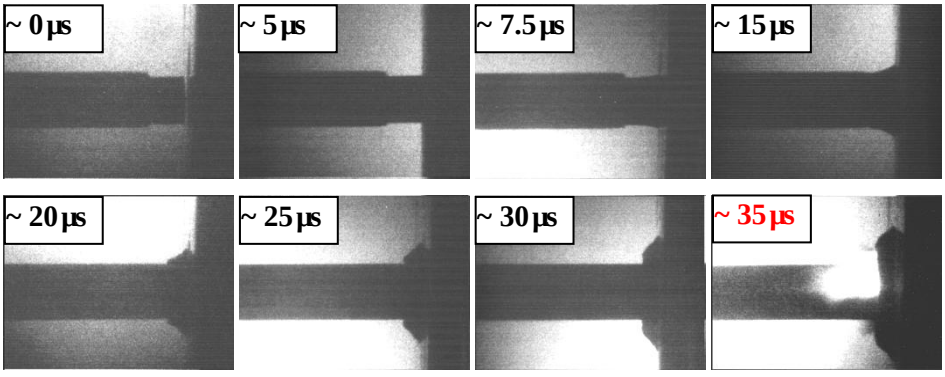

Figure 4.4. Consecutive images of the Taylor impact test on PTFE 7A / Ti composite (Batch #1, medium size), V_i = 135.1 m/s, t_{exp} = 500 ns, and t_{int} = 2 µs

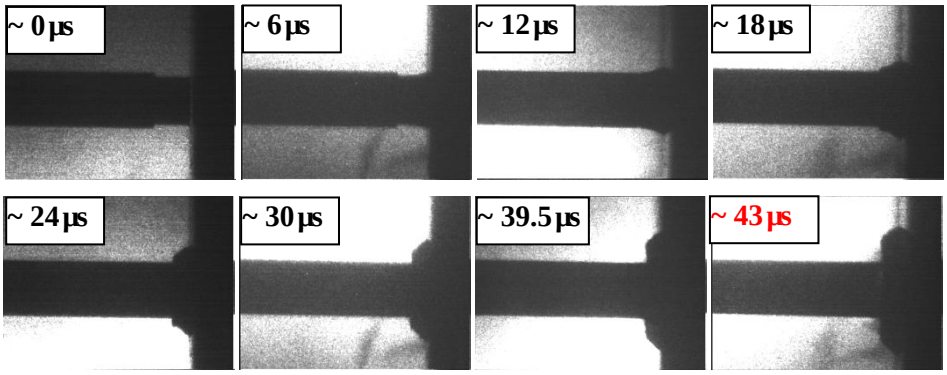

Figure 4.5. Consecutive images of the Taylor impact test on PTFE 7A / Ti composite (Batch #1, medium size), V_i = 117.94 m/s, t_{exp} = 500 ns, and t_{int} = 2.5 µs (first 13 frames), t_{int} = 3 µs (last 3 frames)

At each impact velocity, reaction light was observed as intense flash coming from the annular region at the rear end of the sample after it deformed to certain extent, which was deemed to be the indication of the beginning of chemical reaction, and the corresponding ignition time was emphasized in red. Sample deformation under various velocities shared one common process: (1) the composite sample was first deformed upon impact with the anvil, with the strain gradually decreasing from the front to the rear (projectile unchanged); (2) the deformation of the composite sample proceeded until the diameter of the rear end exceeded the diameter of the projectile, after which the projectile started punching into the composite sample, i.e., the shear strain / shear stress started to play an important role from this moment forwarded; and (3) the composite sample kept deforming under the impulse and thrust from the projectile until the point that the chemical reaction was triggered, after which the deformation of the projectile could not be observed from the images.

Figure 4.6 shows the axial / areal strain of the composite sample *vs.* image sequence at various impact velocities:

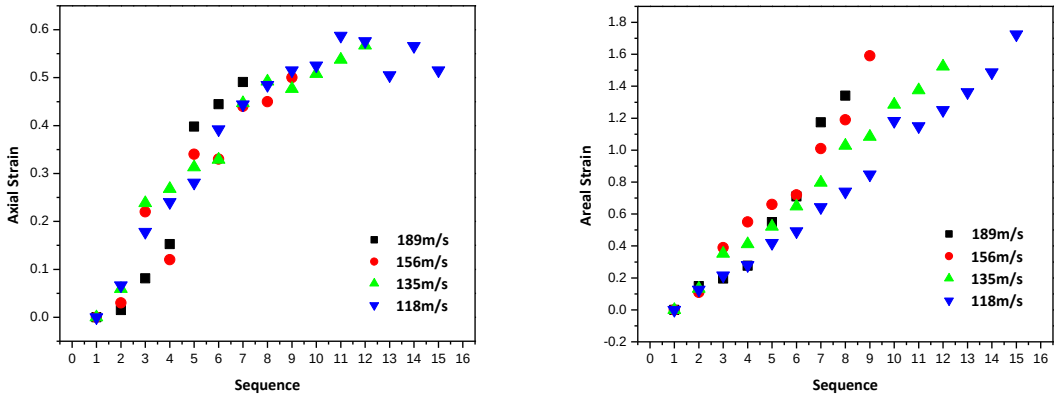

(a) (b)

Figure 4.6. Axial strain (a) and areal strain (b) *vs.* image sequence of PTFE 7A / Ti composite (Batch #1) under four different impact velocities

Axial / areal strains were measured from images by *Photoshop* software and they stopped at the critical points, after which chemical reaction took place. The critical axial strains were around 50 - 60% and the critical areal strains 140 - 170%, both of which were independent of impact velocities. The impact-initiated reaction between PTFE 7A and Ti relied not only on impact velocities which were related to kinetic energy, but also highly on the degree of deformation.

Figure 4.7 relates the ignition time with kinetic energy at five different impact velocities:

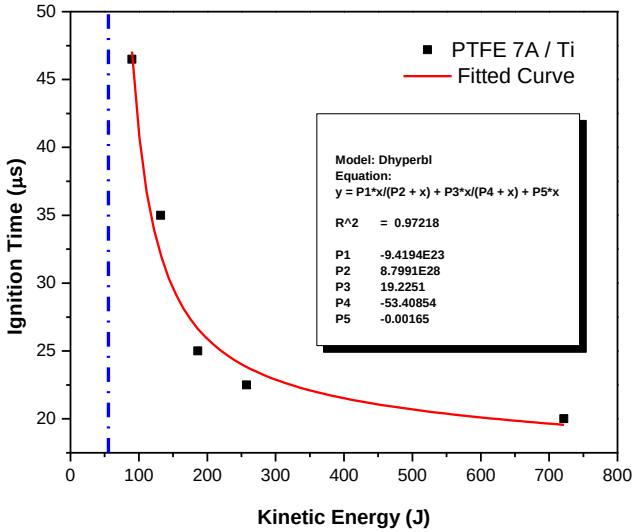

Figure 4.7. Ignition time *vs.* kinetic energy based on the Taylor impact test at five different impact velocities (Batch #1). The blue dash dot indicates the limit of the red curve.

As kinetic energy decreased, the ignition time increased with an increasing rate. By fitting the data points with the *Dhyperbl* function, an asymptote at x = 53.41 J was obtained, which appeared to be the critical value of kinetic energy, below which the reaction could not be triggered (see blue dash-dot line, Figure 4.7). This critical kinetic energy (impact velocity) was related to the activation energy of the PTFE 7A / Ti reaction.

4.3.1.2 Small and Even Smaller Dimension

Figure 4.8 and 4.9 show transient Taylor impact images of PTFE 7A / Ti composite samples with small and even smaller dimensions at around 300 m/s:

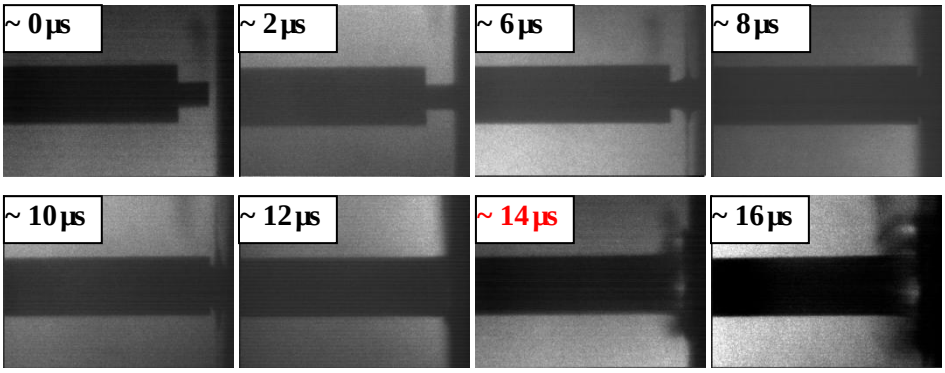

Figure 4.8. Consecutive images of the Taylor impact test on PTFE 7A / Ti composite (Batch #1, small size), V_i = 309.2 m/s, t_{exp} = 500 ns, and t_{int} = 1.5 μs

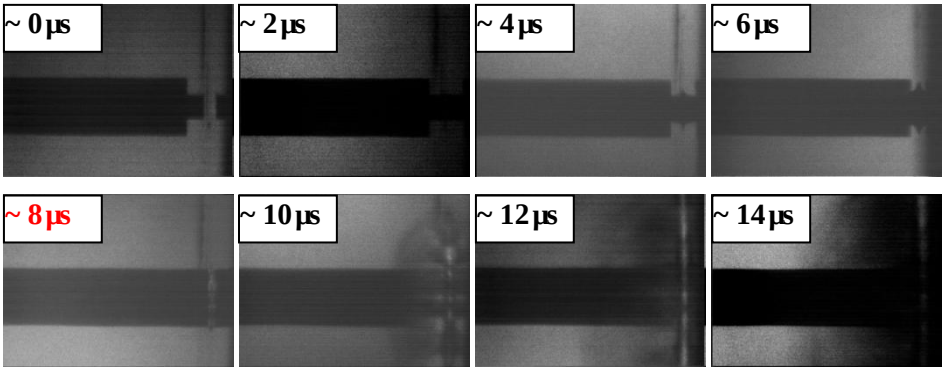

Figure 4.9. Consecutive images of the Taylor impact test on PTFE 7A / Ti composite (Batch #1, even smaller size), V_i = ~ 300 m/s, t_{exp} = 500 ns, and t_{int} = 1.5 μs

The deformation process for the small dimension sample experienced similar three stage process as described for the medium dimension samples: (1) sample deformed; (2) the sample diameter exceeded the projectile diameter and the projectile punched inside the sample; and (3) the reaction was triggered. For the even smaller composite sample, since the size of the sample was so small that strain in the radial direction could not go beyond that of the projectile, the punching phenomenon before the display of reaction light was not detected (Figure 4.9). Compared with the ignition time (~ 20 μs) for the medium size

sample at ~ 300 m/s impact velocity, the small and even smaller sample showed shorter ignition times, 14 μs and 8 μs, respectively. From the data, the conclusion was drawn that the smaller the sample size, the shorter the ignition time.

4.3.2 PTFE 7A (51 wt%) / Ti (49 wt%) Composite (Batch #2) with Uniform Distribution

The PTFE 7A / Ti composite (Batch #2) was investigated with the Taylor impact test. Besides the three dimensions (medium, small and even smaller) used in Batch #1, one more size — large dimension samples were also prepared for testing, in which case the composite samples were directly propelled onto the target anvil.

4.3.2.1 Medium Dimension

Transient images of the Taylor impact tests for the Batch #2 composite samples are shown in Figures 4.10 - 4.13 at impact velocities ranging from ~100 m/s to ~ 400 m/s:

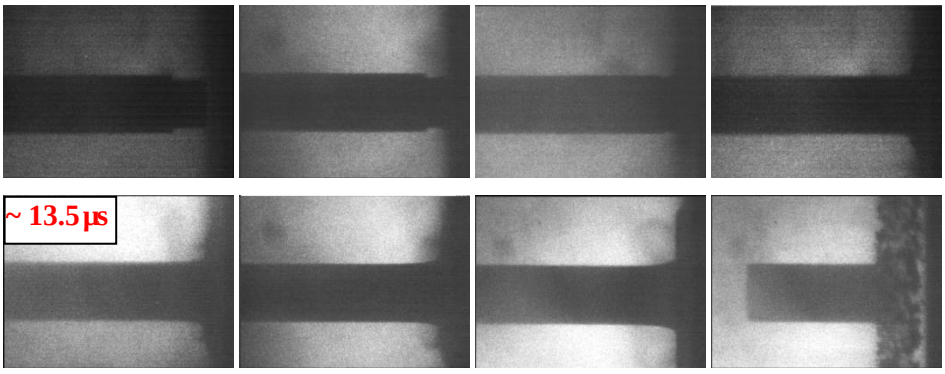

Figure 4.10. Consecutive images of the Taylor impact test on PTFE 7A / Ti composite (Batch #2, medium size), V_i = 395.5 m/s, t_{exp} = 500 ns and t_{int} = 1 μs

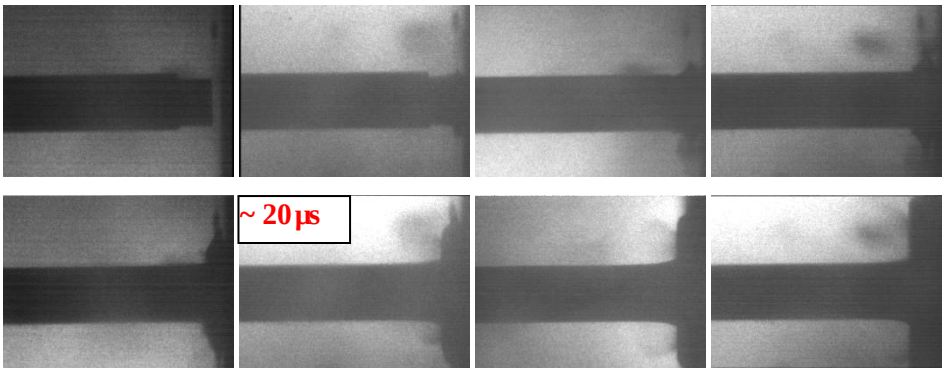

Figure 4.11. Consecutive images of the Taylor impact test on PTFE 7A / Ti composite (Batch #2, medium size), V_i = 304.41 m/s, t_{exp} = 500 ns, and t_{int} = 1.5 µs

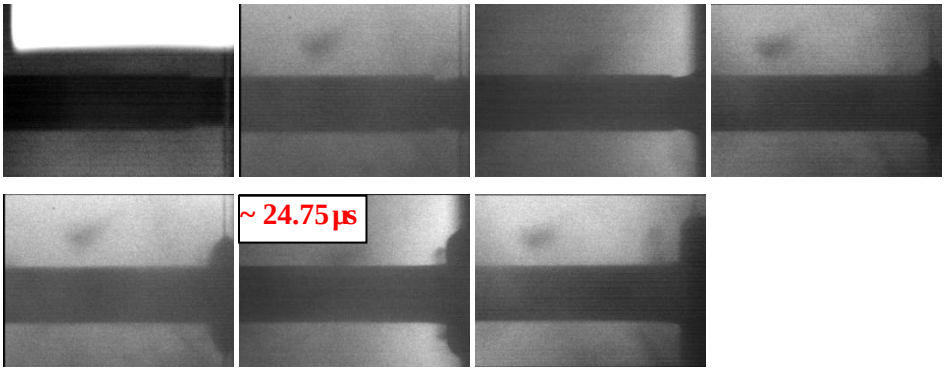

Figure 4.12. Consecutive images of the Taylor impact test on PTFE 7A / Ti composite (Batch #2, medium size), V_i = 200.96 m/s, t_{exp} = 500 ns and t_{int} = 1.75 µs

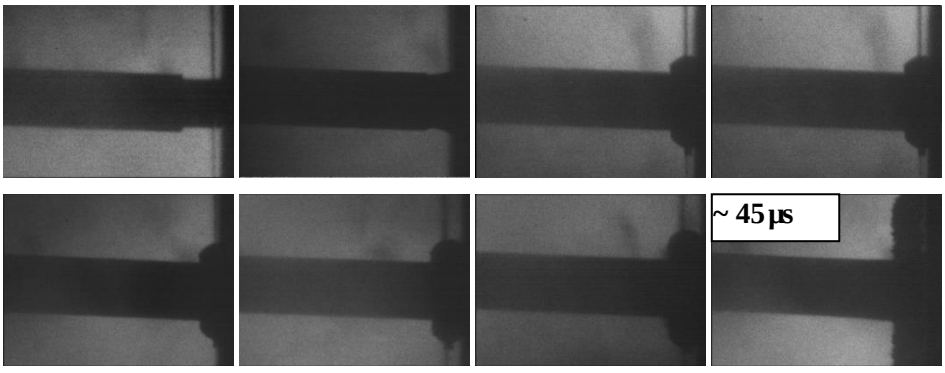

Figure 4.13. Consecutive images of the Taylor impact test on PTFE 7A / Ti composite (Batch #2, medium size), V_i = 100.17 m/s, t_{exp} = 500 ns and t_{int} = 2.5 µs

Because of the limitation of the *Imacon 200* digital camera, some of the images were missing out of the overall 16 during impact loading, and thus the exact time sequence of the images could not be accurately recorded, and only the approximate ignition time was marked in red in these image series. Instead of reaction light as detected with Batch #1, only reaction fume emitting from the annular region at the rear end of the sample was observed at impact velocities from ~ 200 m/s to ~ 400 m/s. Although the reaction fume was hard to distinguish from powder fume by impact, the location of the rising fume was the same as that of the reaction light emission with Batch #1. The fume emission was therefore considered as an indication of impact-initiated chemical reaction, but with lower reactivity compared to reaction light emission. As the impact velocity decreased, the reaction fume became less evident, becoming invisible at ~ 100 m/s. The three-stage deformation process was also the same as previously described.

The axial / areal strain curves *vs.* sequence for the Batch #2 samples are plotted in Figure 4.14 at three impact velocities, all of which stopped at the point that the first reaction fume arose:

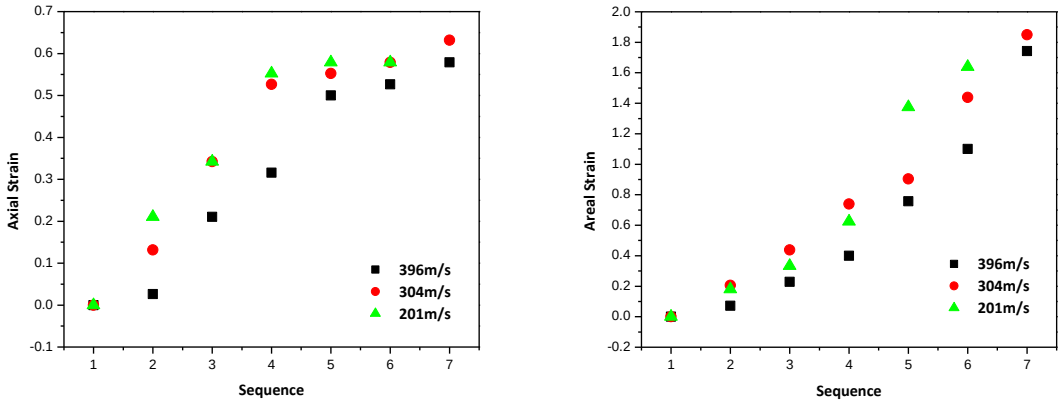

(a) (b)

Figure 4.14. Axial strain (a) and areal strain (b) *vs.* image sequence of PTFE 7A / Ti composite (Batch #2) under three different impact velocities

The critical axial / areal strains read from the plots were in the range of 55 - 65% and 160 - 180%, respectively, which were slightly higher than those of Batch #1. The impact-initiated reaction of PTFE 7A / Ti composite was highly dependent on the degree of deformation.

Figure 4.15 relates the ignition time with kinetic energy at three different impact velocities for the Batch #2 samples:

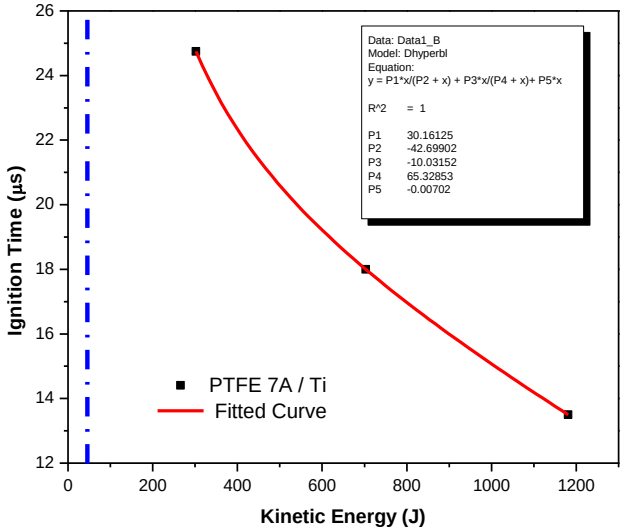

Figure 4.15. Ignition time *vs.* kinetic energy based on the Taylor impact test at three different impact velocities (Batch #2). The blue dash dot indicates the limit of the red curve.

The plot was fitted to the *Dhyperbl* function and the asymptote was obtained at x = 42.70 J, which was deemed the critical value of kinetic energy for the PTFE 7A / Ti composite and below which the reaction could not be triggered (see blue dash-dot line, Figure 4.15). With an impact velocity of ~ 100.17 m/s for the Batch #2 sample, the ignition fume was not detected until the last frame of ~ 45 µs. By applying the corresponding kinetic energy of 75.48 J in this case to the fitted *Dhyperbl* function, a ignition time of 63.45 µs was obtained, which concluded that there might be chemical reaction triggered beyond the time scale captured by the camera.

4.3.2.2 Small and Even Smaller Dimension

Figure 4.16 - 4.19 show the Taylor impact images of a small dimension sample at impact velocities of ~ 200 m/s and ~ 100 m/s, and a even smaller dimension sample at impact velocities of ~ 200 m/s and ~ 100 m/s:

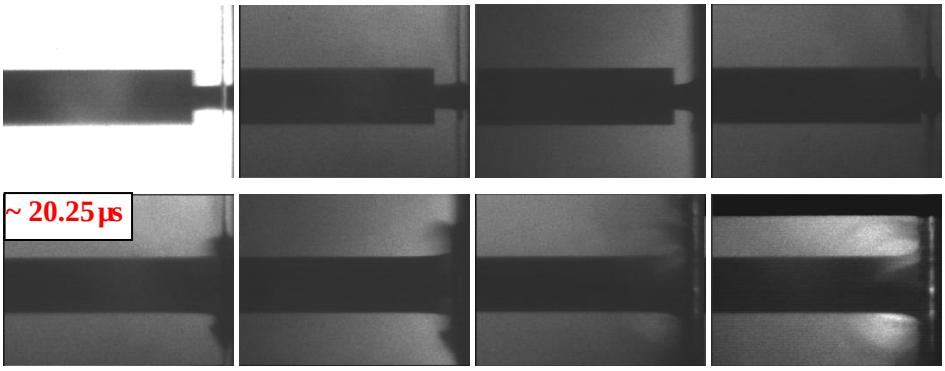

Figure 4.16. Consecutive images of the Taylor impact test on PTFE 7A / Ti composite (Batch #2, small size), V_i = 198.67 m/s, t_{exp} = 500 ns and t_{int} = 1.75 μs

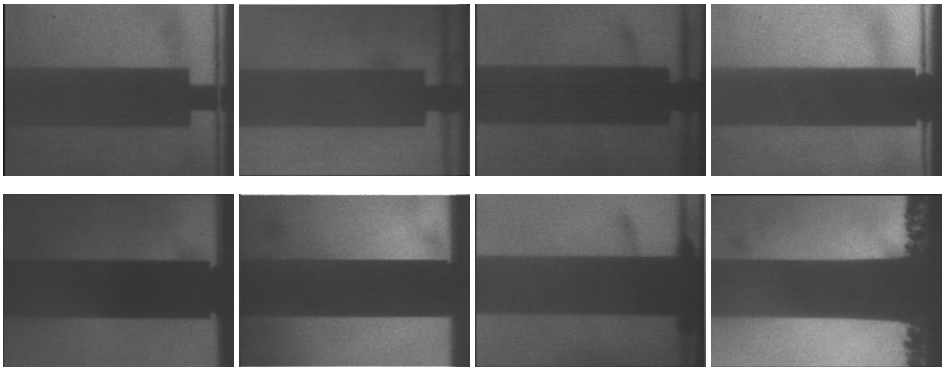

Figure 4.17. Consecutive images of the Taylor impact test on PTFE 7A / Ti composite (Batch #2, small size), V_i = 99.44 m/s, t_{exp} = 500 ns and t_{int} = 2.5 μs

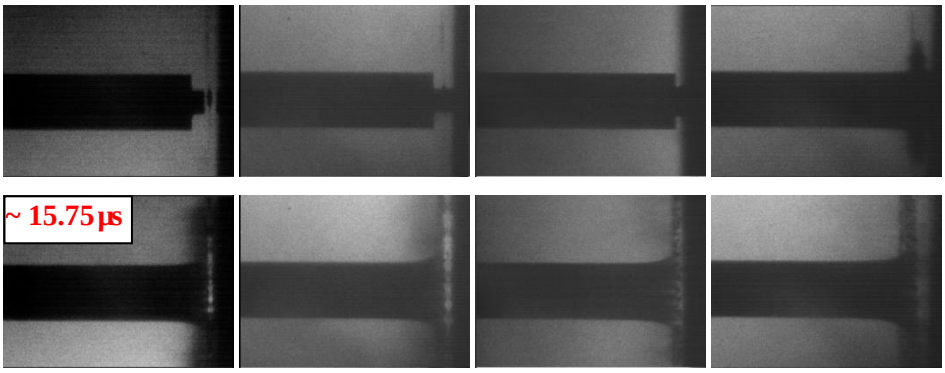

Figure 4.18. Consecutive images of the Taylor impact test on PTFE 7A / Ti composite (Batch #2, even smaller size), V_i = 203.04 m/s, t_{exp} = 500 ns and t_{int} = 1.75 µs

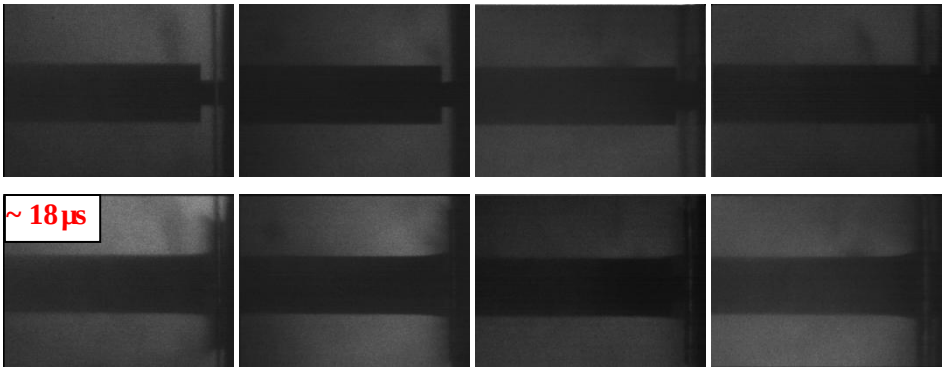

Figure 4.19. Consecutive images of the Taylor impact test on PTFE 7A / Ti composite (Batch #2, even smaller size), V_i = 101.68 m/s, t_{exp} = 500 ns and t_{int} = 2.5 µs

At impact velocity of ~ 200 m/s, the small dimension sample exhibited reaction fume first at ~ 20.25 µs, then severe reaction light around the whole deformed sample. The even smaller dimension showed sample reaction light directly at ~ 15.75 µs. Compared with the medium dimension sample that showed reaction fume only, the smaller the sample, the more severe the impact-initiated reaction. At the impact velocity of ~ 100 m/s, similar phenomena were also observed: the small dimension sample did not show any reaction fume until the end of the image series, while even smaller dimension sample

exhibited weak reaction light at ~18 μs. The conclusion that the smaller the sample size, the shorter the ignition time was reinforced.

4.3.2.3 Large Dimension

Figures 4.20 - 4.24 exhibit the Taylor impact images of Batch #2 PTFE 7A / Ti composites with large dimensions at impact velocities from ~100 m/s to 500 m/s, with the final frame time of each series marked in the last image:

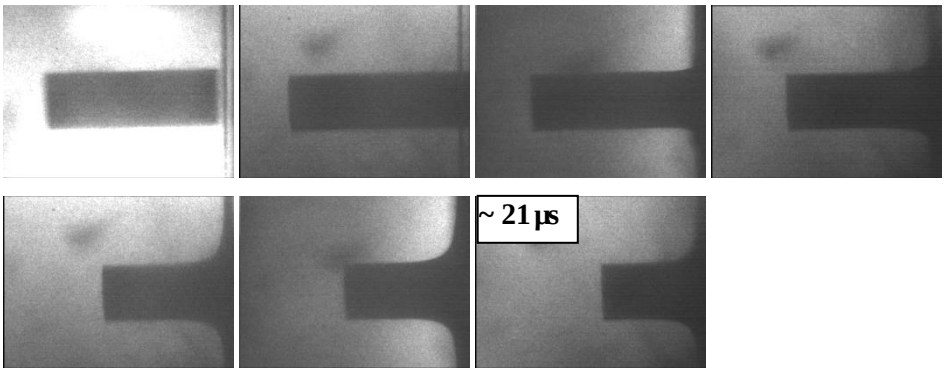

Figure 4.20. Consecutive images of the Taylor impact test on PTFE 7A / Ti composite (Batch #2, large size), V_i = 495.61 m/s, t_{exp} = 500 ns and t_{int} = 1 μs

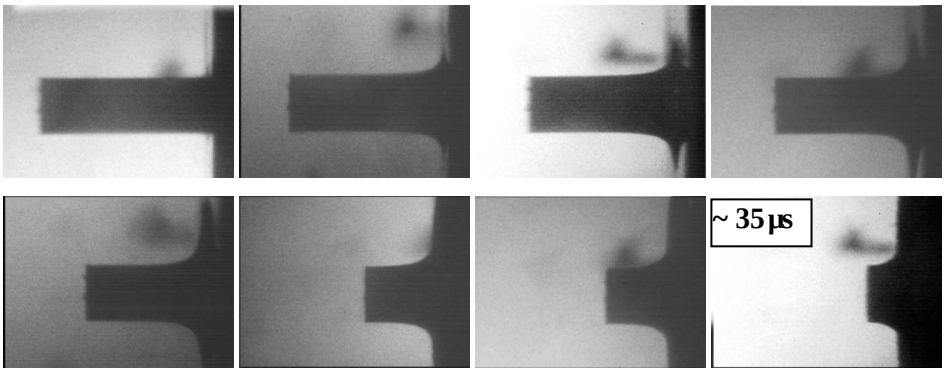

Figure 4.21. Consecutive images of the Taylor impact test on PTFE 7A / Ti composite (Batch #2, large size), V_i = 406.44 m/s, t_{exp} = 500 ns and t_{int} = 2 μs

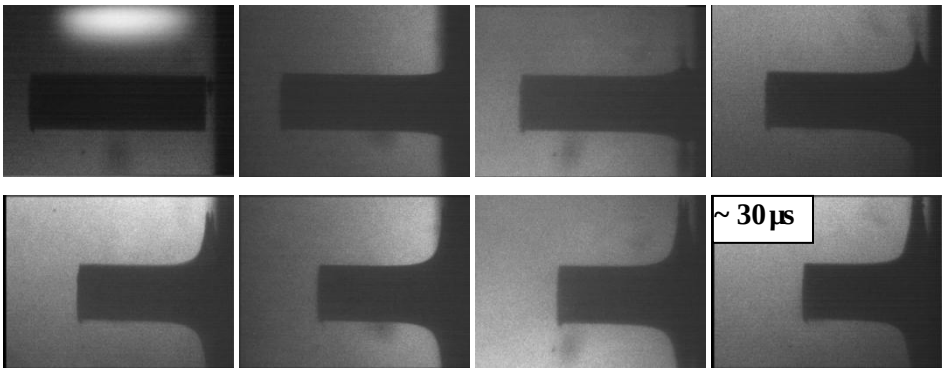

Figure 4.22. Consecutive images of the Taylor impact test on PTFE 7A / Ti composite (Batch #2, large size), V_i = 282.56 m/s, t_{exp} = 500 ns and t_{int} = 1.5 µs

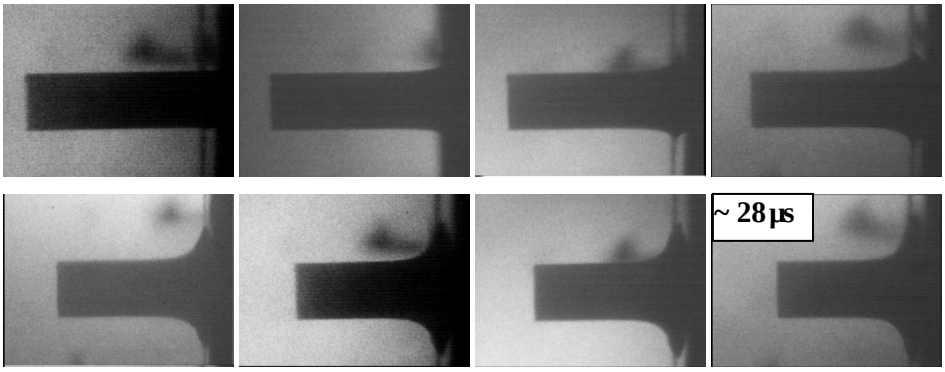

Figure 4.23. Consecutive images of the Taylor impact test on PTFE 7A / Ti composite (Batch #2, large size), V_i = 201.01 m/s, t_{exp} = 500 ns and t_{int} = 1.5 µs

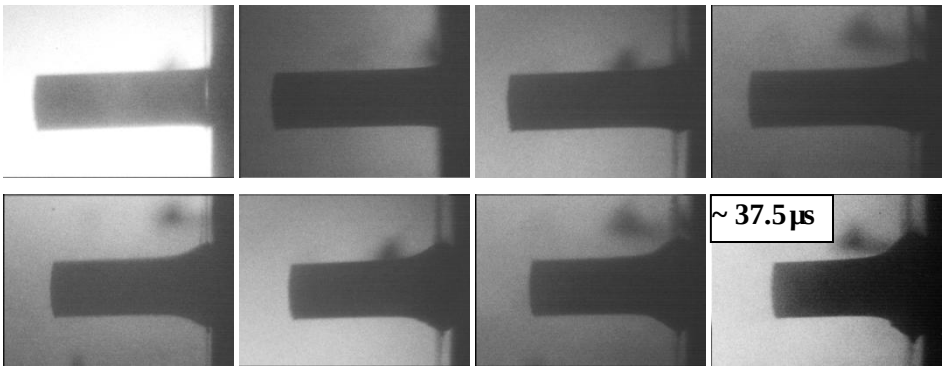

Figure 4.24. Consecutive images of the Taylor impact test on PTFE 7A / Ti composite (Batch #2, large size), V_i = 112.38 m/s, t_{exp} = 500 ns and t_{int} = 2 µs

Unlike the phenomena observed in the previous series, no ignition light was observed even at the impact velocity of 500 m/s, indicating the chemical reactions observed in the previous series did not take place for large dimension samples. As explained previously, the impact-initiated reaction was dependent on both impact velocity (kinetic energy) and degree of deformation that was highly related to the shear strain / stress. For large dimension samples, the kinetic energy could reach 339.15 J at the impact velocity of 495.61 m/s, which was comparable to the value for medium dimension samples for Batch #1 and Batch #2 where impact-initiated reactions were observed. The criterion of kinetic energy was reached in this case, but the shear strain / stress did not reach the critical point, leading to failure of the triggering chemical reaction. The biggest difference on Taylor impact tests between large dimension samples and medium / small / even smaller samples lay on the existence of the copper rod. When samples were attached onto copper rods, the shear strain / stress produced by the punching effect was much more pronounced than the samples without copper rod inclusion. However, the deformation processes without chemical reactions involved could be utilized to collect the dynamic behavior information based on the film reduction method (see Subsection Four).

4.3.3 PTFE 7A (32.4 wt%) / Ti (67.6 wt%) Composite (Batch #3) with Equal Volume Composition

For PTFE 7A / Ti composite Batch #3, the same experimental procedures were performed as for Batch #2. Medium, small and even smaller dimensions samples were tested by attaching them onto copper projectiles, while large dimension samples were propelled directly onto the target anvil.

4.3.3.1 Medium Dimension

Figures 4.25 - 4.28 show the transient Taylor impact images of the PTFE 7A / Ti composite from Batch #3 at impact velocities ranging from ~ 90 m/s to ~ 400 m/s:

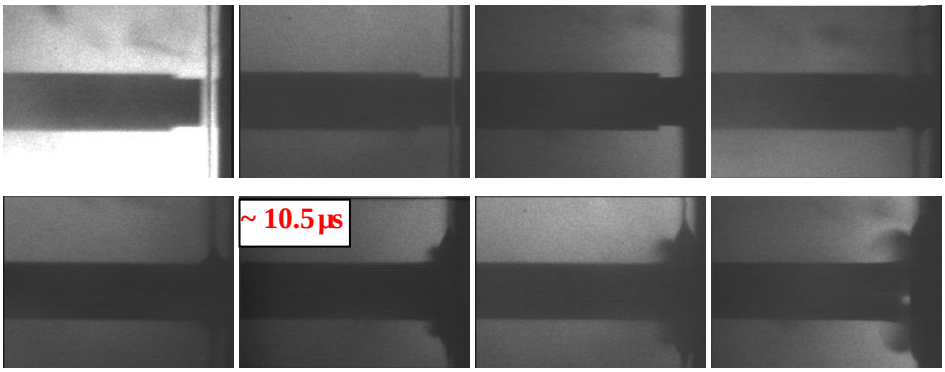

Figure 4.25. Consecutive images of the Taylor impact test on PTFE 7A / Ti composite (Batch #3, medium size), V_i = 408.44 m/s, t_{exp} = 500 ns and t_{int} = 1 µs

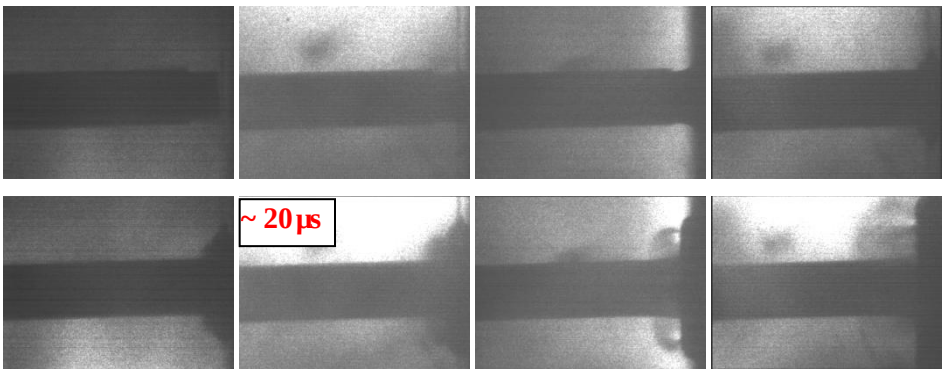

Figure 4.26. Consecutive images of the Taylor impact test on PTFE 7A / Ti composite (Batch #3, medium size), V_i = 281.32 m/s, t_{exp} = 500 ns and t_{int} = 1.5 µs

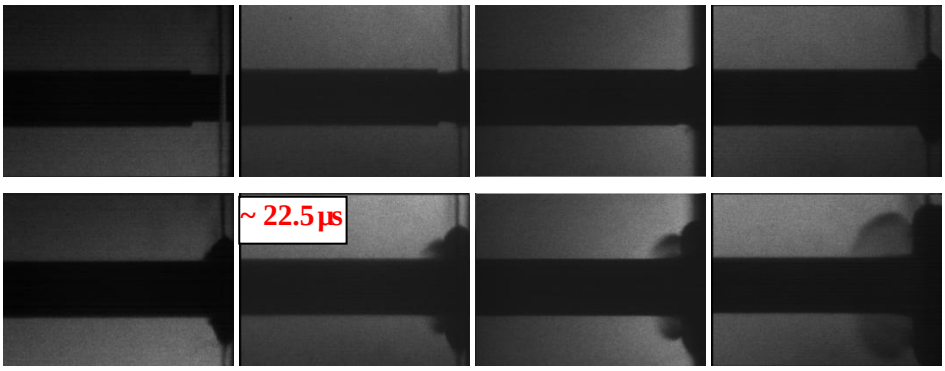

Figure 4.27. Consecutive images of the Taylor impact test on PTFE 7A / Ti composite (Batch #3, medium size), V_i = 204.59 m/s, t_{exp} = 500 ns and t_{int} = 1.75 µs

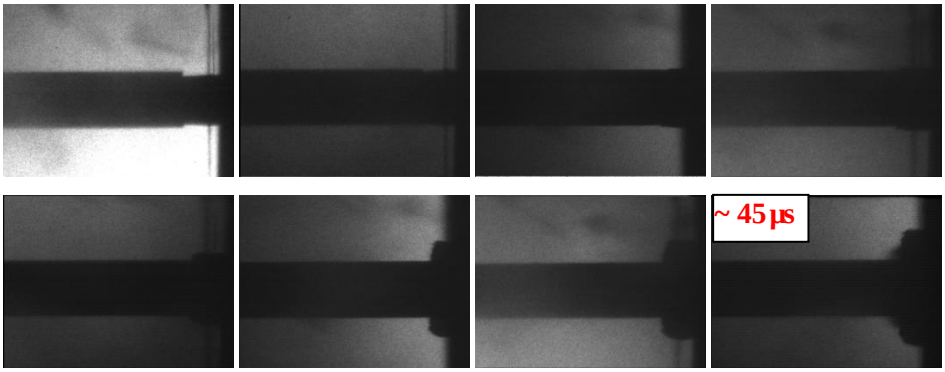

Figure 4.28. Consecutive images of the Taylor impact test on PTFE 7A / Ti composite (Batch #3, medium size), V_i = 88.99 m/s, t_{exp} = 500 ns and t_{int} = 2.5 µs

Like the phenomena observed for the Batch #2 samples, the reaction fume first emitted from the location around the shear band of the deformed Batch #3 samples. However, at the impact velocities of 408.44 m/s and 281.32 m/s, the reaction fume then converted to reaction light as earlier shown in the Batch #1 sample images. At impact velocities of 204.59 m/s and 88.99 m/s, the reaction fume remained the same, but became more severe at the very end of the image series. Recalling the deformation images of medium dimension samples for Batch #1 and Batch #2, the impact-initiated reaction in Batch #3

was not as severe as in Batch #1, but more severe than in Batch #2. One common observation in these three batches was that they all followed the three-stage deformation process to trigger the chemical reaction.

The axial / areal strains *vs.* image sequence for the Batch #3 samples are shown below in Figure 4.29:

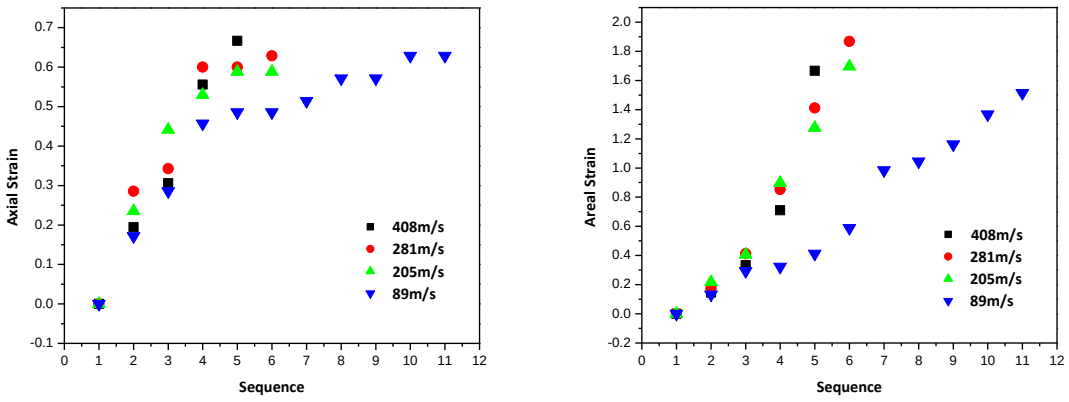

(a) (b)

Figure 4.29. Axial strain (a) and areal strain (b) *vs.* image sequence of PTFE 7A / Ti composite (Batch #3) under four different impact velocities

The critical axial / areal strains were separately in the range of 55 - 65 % and 150 - 185 %, which were almost at the same level as in Batch #2 and Batch #1.

Figure 4.30 plots the kinetic energy (impact velocity) *vs.* ignition time for the Batch #3 samples at four different impact velocities:

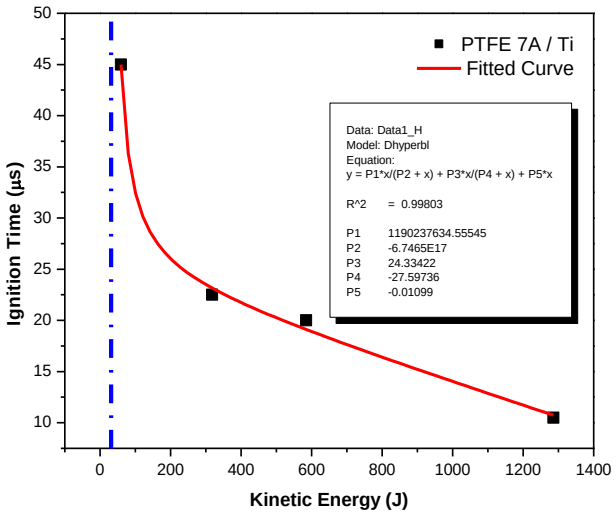

Figure 4.30. Ignition time versus kinetic energy based on the Taylor impact test at four different impact velocities (Batch #3). The blue dash-dot line indicates the limit of the red curve.

After fitting with the *Dhyperbl* function, the critical kinetic energy determined to be x = 27.60 J (see the blue dash-dot line in Figure 4.30). The curve showed an exponential decay in ignition time as kinetic energy (impact velocity) increased, similar to the plots for the Batch #1 and Batch #2 samples.

4.3.3.2 Small and Even Smaller Dimension

Figures 4.31 - 4.34 show the Taylor impact images of small dimension Batch #3 samples at impact velocities of ~ 200 m/s and ~ 100 m/s, and even smaller dimension samples at impact velocities of ~ 200 m/s and ~ 100 m/s:

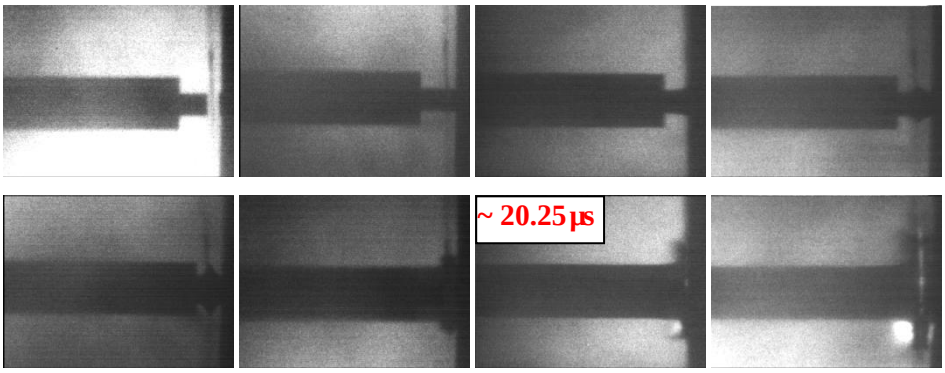

Figure 4.31. Consecutive images of the Taylor impact test on PTFE 7A / Ti composite (Batch #3, small size), V_i = 201.44 m/s, t_{exp} = 500 ns and t_{int} = 1.75 µs

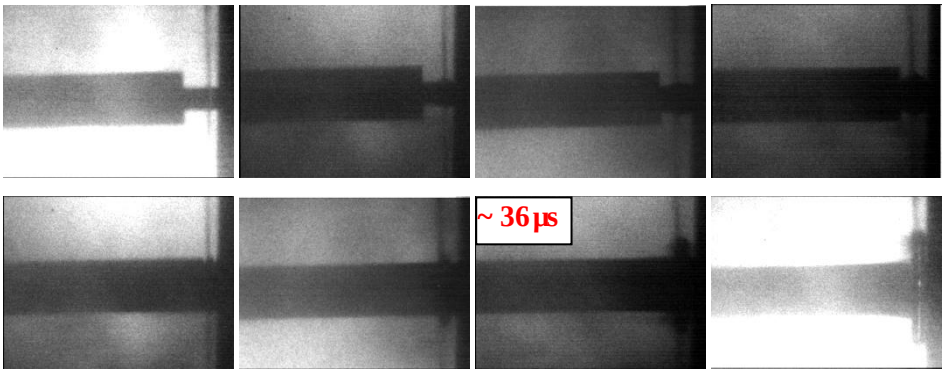

Figure 4.32. Consecutive images of the Taylor impact test on PTFE 7A / Ti composite (Batch #3, small size), V_i = 91.08 m/s, t_{exp} = 500 ns and t_{int} = 2.5 µs

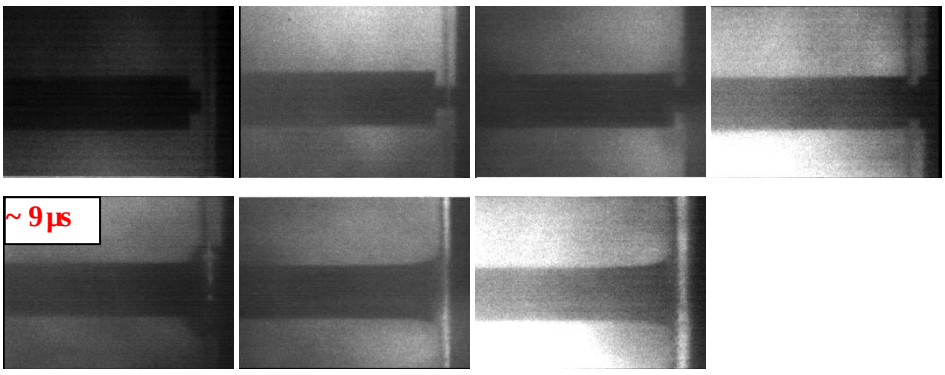

Figure 4.33. Consecutive images of the Taylor impact test on PTFE 7A / Ti composite (Batch #3, even smaller size), V_i = 204.11 m/s, t_{exp} = 500 ns and t_{int} = 1.75 µs

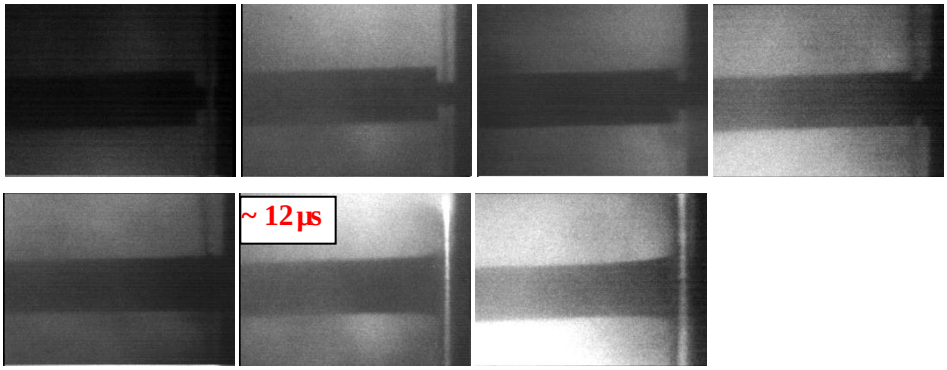

Figure 4.34. Consecutive images of the Taylor impact test on PTFE 7A / Ti composite (Batch #3, even smaller size), V_i = 100.64 m/s, t_{exp} = 500 ns and t_{int} = 2.5 μs

All of the four series eventually exhibited reaction light, even at the impact velocity of ~ 100 m/s. The severity of the reaction for Batch #3 samples was more intense than that of Batch #2, but less violent than that of Batch #1. As before, the smaller the sample size, the more severe the reaction and the shorter the ignition time.

4.3.3.3 Large Dimension

Figures 4.35 - 4.39 exhibit the Taylor impact images of large dimension Batch #3 samples with impact velocities from ~ 100 m/s to ~ 500 m/s:

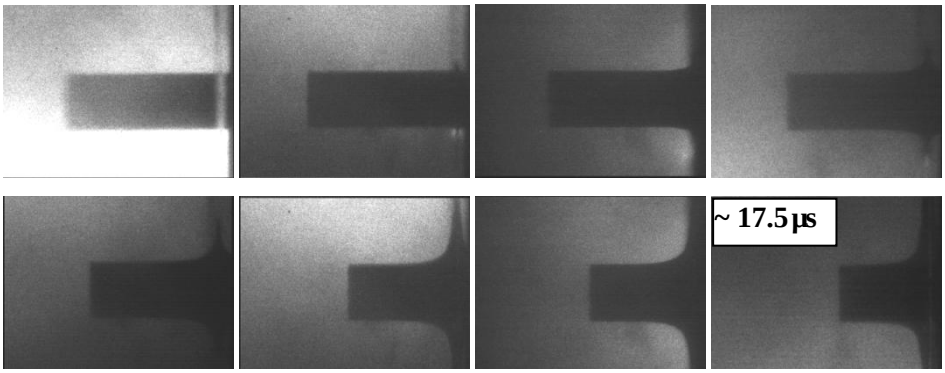

Figure 4.35. Consecutive images of the Taylor impact test on PTFE 7A / Ti composite (Batch #3, large size), V_i = 498 m/s, t_{exp} = 500 ns and t_{int} = 0.75 µs

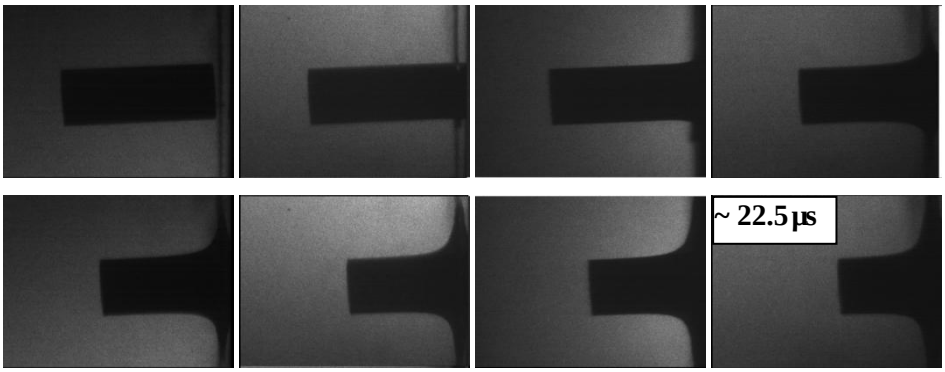

Figure 4.36. Consecutive images of the Taylor impact test on PTFE 7A / Ti composite (Batch #3 large size), V_i = 399.02 m/s, t_{exp} = 500 ns and t_{int} = 1 µs

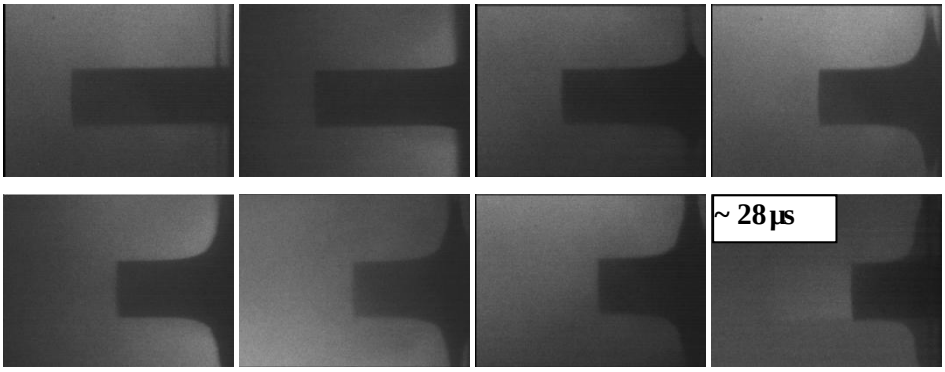

Figure 4.37. Consecutive images of the Taylor impact test on PTFE 7A / Ti composite (Batch #3, large size), V_i = ~300 m/s, t_{exp} = 500 ns and t_{int} = 1.5 µs

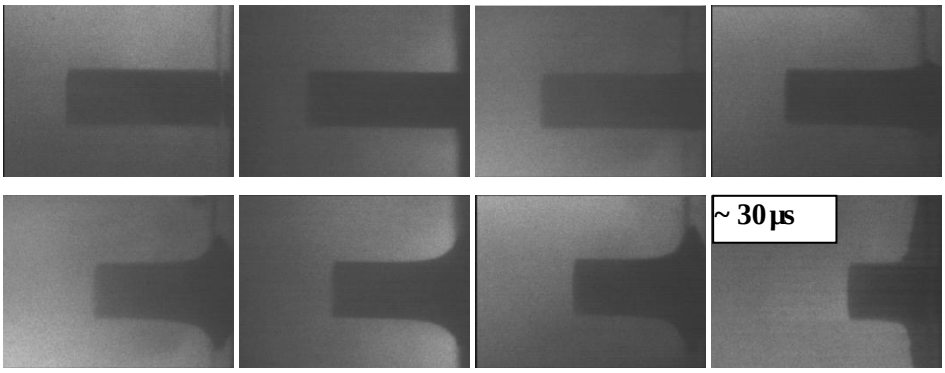

Figure 4.38. Consecutive images of the Taylor impact test on PTFE 7A / Ti composite (Batch #3, large size), V_i = 196.53 m/s, t_{exp} = 500 ns and t_{int} = 1.5 μs

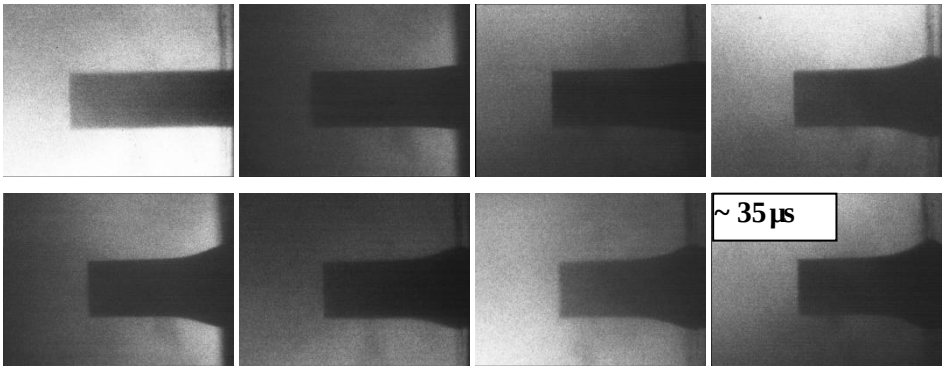

Figure 4.39. Consecutive images of the Taylor impact test on PTFE 7A / Ti composite (Batch #3, large size), V_i = 90.95 m/s, t_{exp} = 500 ns and t_{int} = 2 μs

Like the phenomena observed with Batch #2 samples, no ignition light was detected for all of the series, even at the impact velocity of ~ 500 m/s. For example, with V_i = 498 m/s, the kinetic energy was 342.82 J, far beyond the kinetic energy threshold for Batch #3 samples of medium dimensions. Shear strain / stress was concluded to play an important role in triggering the impact-initiated chemical reaction for the PTFE 7A / Ti composite. Figures 4.35 - 4.39 will also be used to provide the dynamic behavior information in Subsection Four.

4.3.4 Film Reduction (House Method) Analysis

With the development of high-speed photography in the 1980s, the Taylor impact test was employed as a means to validate and establish the constitutive relationship for the target material at high strain rates, since the dynamic deformation process could be recorded and analyzed to extract useful information such as stress, strain and strain rate. House et al. developed the film reduction method to provide additional information for the constitutive model at high strain rates [27].

4.3.4.1 House Method

Generally, the House method can be divided into five steps for obtaining the information of stress, stain, and strain rate during two time intervals:

(1) Plot radius *vs.* axial position curves at three different frame times, t_1, t_2 and t_3 ($t_1 < t_2 < t_3$), by measuring the images taken by the *Imacon 2000* digital camera in *Photoshop* (Figure 4.40), then converting them into strain *vs.* axial position plots by adopting the definition of areal strain (Equation 4.1):

$$e = 1 - \frac{A_0}{A} \tag{4.1}$$

where A_0 is the original sample cross section area, and A is the current cross section area at the location of areal strain e (Figure 4.41):

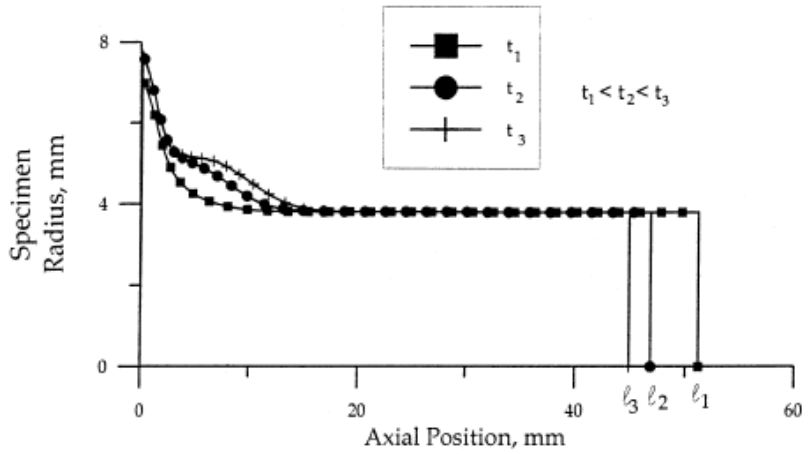

Figure 4.40. Specimen radius *vs.* axial position at three frame times [27]

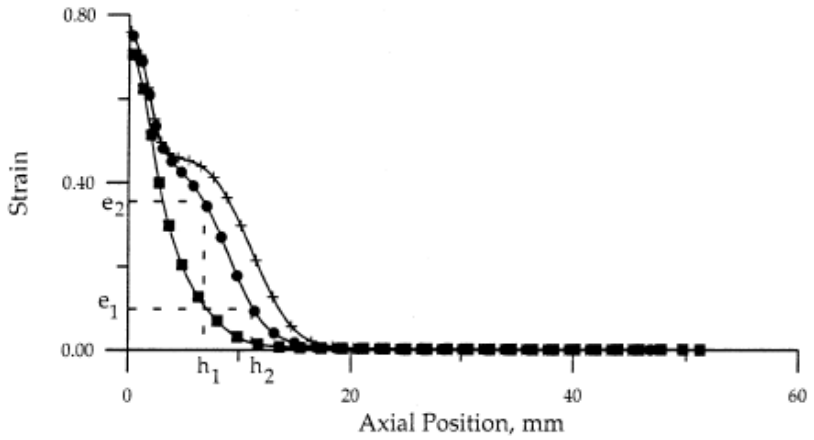

Figure 4.41. Strain *vs.* axial position at three frame times [27]

(2) Calculate the back end speed u by definition (Equation 4.2):

$$u = \frac{l_1 - l_2}{t_2 - t_1} \tag{4.2}$$

where l_1 and l_2 are the specimen lengths corresponding to t_1 and t_2.

(3) Calculate the plastic wave speed v by selecting a series of strain values e at the proper intervals, read the corresponding values of axial position h_1 and h_2, then define the

plastic wave speed as travelling the distance h_2 - h_1 during the time interval t_2 - t_1 for one specific strain e (Equation 4.3):

$$v = \frac{h_2 - h_1}{t_2 - t_1} \tag{4.3}$$

(4) Estimate the strain rate value by selecting a series of axial position values at the proper intervals, read the corresponding values of strain e_1 and e_2, then define the strain rate as the change in strain e_2 - e_1 during time interval t_2 - t_1 at one specific axial position (Equation 4.4):

$$\frac{de}{dt} = \frac{e_2 - e_1}{t_2 - t_1} \tag{4.4}$$

(5) Obtain the stress information by applying the conservation of mass and momentum at the plastic wave front (refer to Figure 2.5 and Equation 2.17-18) so that the stress associated with the strain corresponding to the change from A_0 to A can be calculated as (Equation 4.5):

$$\sigma = \rho(u + v)v \tag{4.5}$$

4.3.4.2 Film Reduction Analysis on Large Dimension Samples

Following the five-step procedure, the stress / strain rate *vs.* strain plots were obtained for PTFE 7A / Ti composites Batch #2 and Batch #3, large dimension samples, with the impact velocity ranging from ~ 100 m/s to ~ 400 m/s. For each impact velocity, three frames were selected for film reduction analysis. Interpretive analyses were then conducted for each frame to obtain the strain *vs.* axial position plots, and stress *vs.* strain and strain rate *vs.* strain curves were then obtained at two time intervals (Figures 4.42 - 4.57):

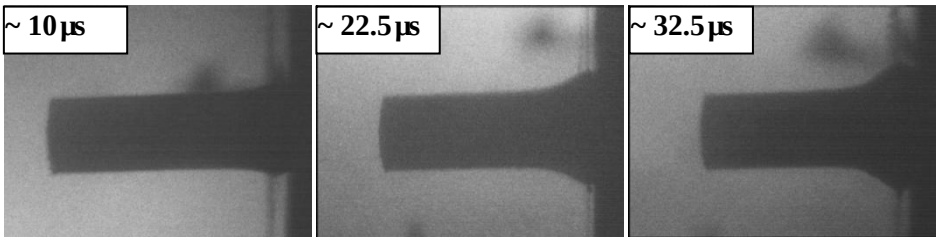

Figure 4.42. Three frames selected for film reduction analysis at V_i = 112.38 m/s (large dimension sample from Batch #2)

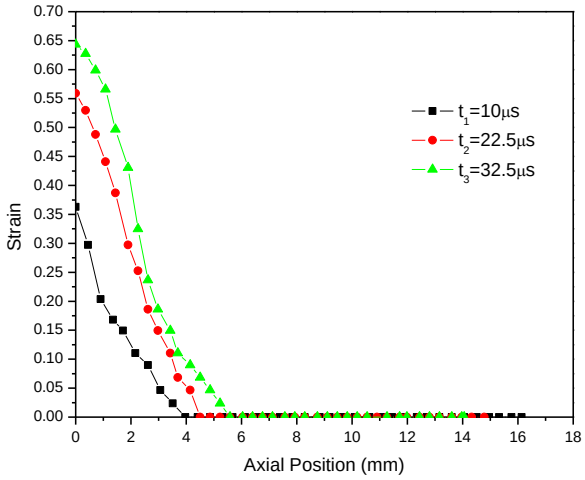

(a)

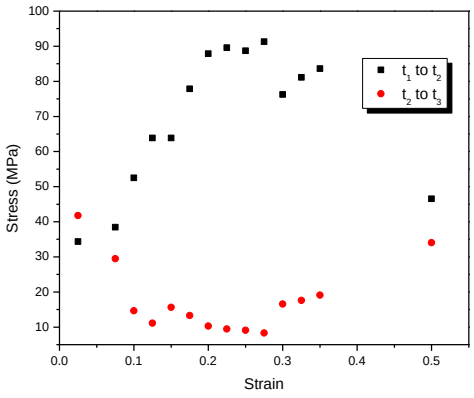

(b)

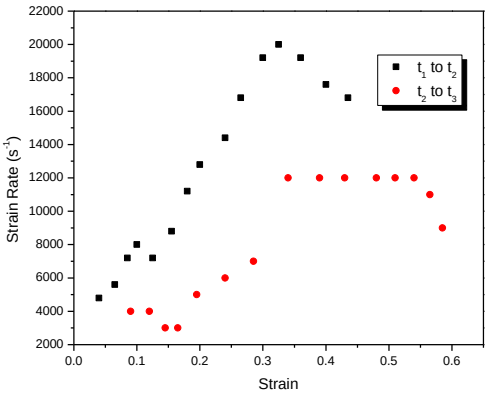

(c)

Figure 4.43. Film data analysis for Batch #2 large dimension sample at V_i = 112.38 m/s, (a) strain *vs.* axial position plots at three different times; (b) stress *vs.* strain curves at two intervals; (c) strain rate *vs.* strain curves at two intervals

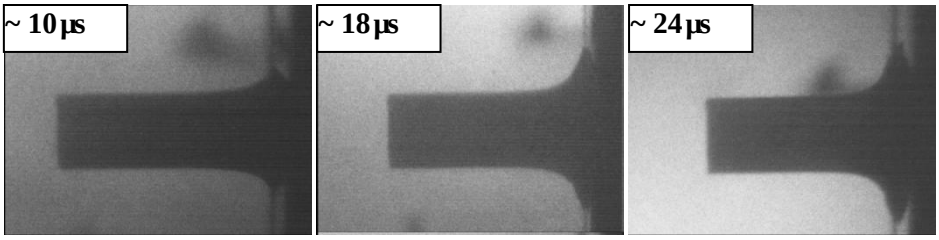

Figure 4.44. Three frames selected for film reduction analysis at V_i = 201.01 m/s (large dimension sample from Batch #2)

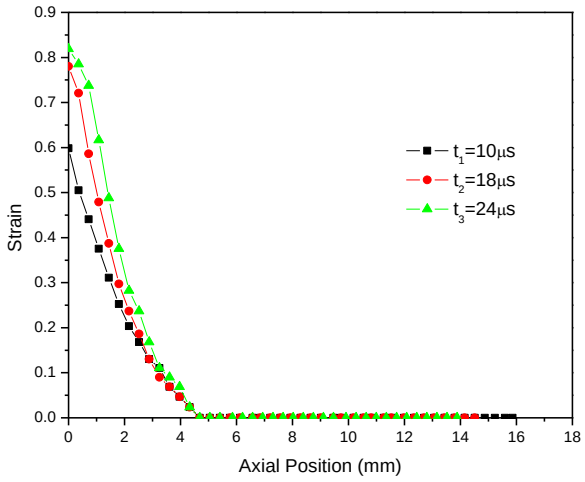

(a)

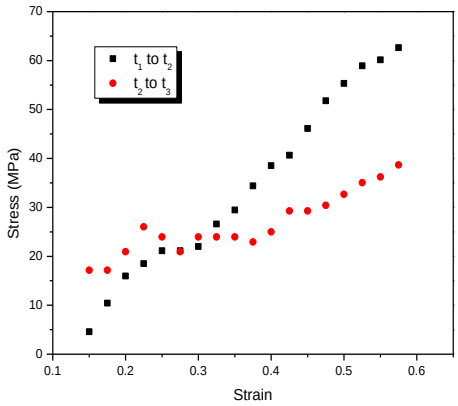

(b)

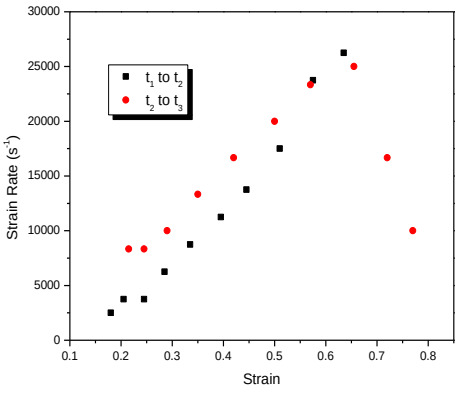

(c)

Figure 4.45. Film data analysis for Batch #2 large dimension sample at V_i = 201.01 m/s, (a) strain *vs.* axial position plots at three different times; (b) stress *vs.* strain curves at two intervals; (c) strain rate *vs.* strain curves at two intervals

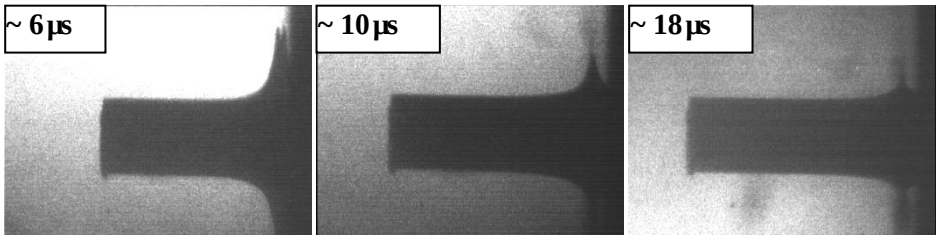

Figure 4.46. Three frames selected for film reduction analysis at V_i = 282.56 m/s (large dimension sample from Batch #2)

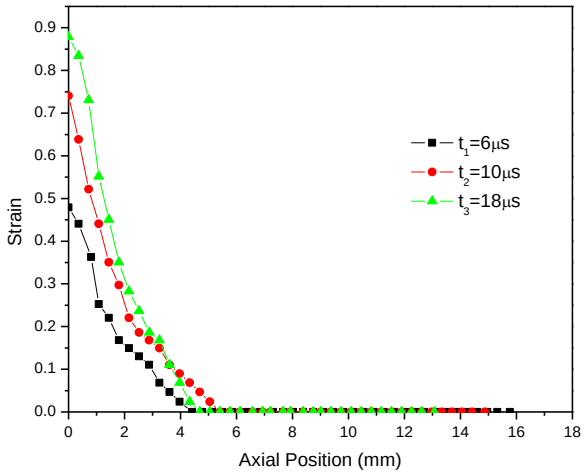

(a)

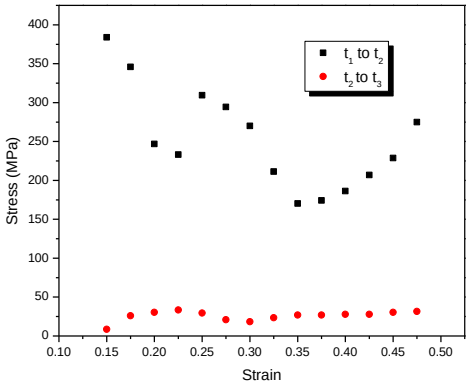

(b)

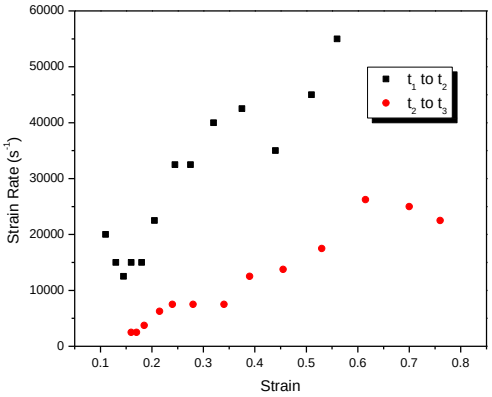

(c)

Figure 4.47. Film data analysis for Batch #2 large dimension sample at V_i = 282.56 m/s, (a) strain *vs.* axial position plots at three different times; (b) stress *vs.* strain curves at two intervals; (c) strain rate *vs.* strain curves at two intervals

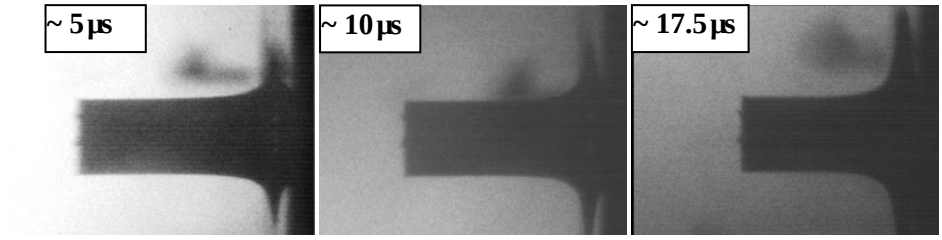

Figure 4.48. Three frames selected for film reduction analysis at V_i = 406.44 m/s (large dimension sample from Batch #2)

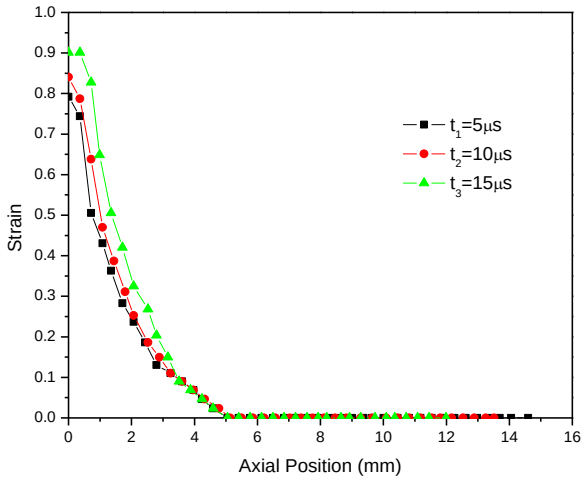

(a)

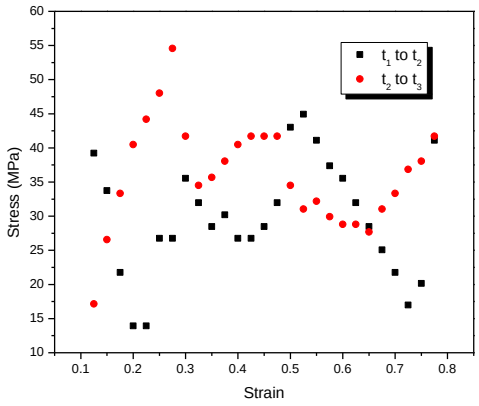

(b)

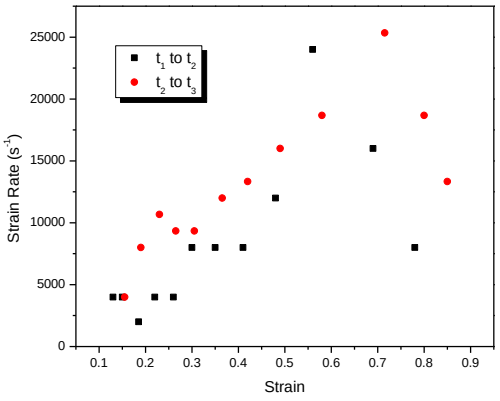

(c)

Figure 4.49. Film data analysis for Batch #2 large dimension sample at V_i = 406.44 m/s, (a) strain *vs.* axial position plots at three different times; (b) stress *vs.* strain curves at two intervals; (c) strain rate *vs.* strain curves at two intervals

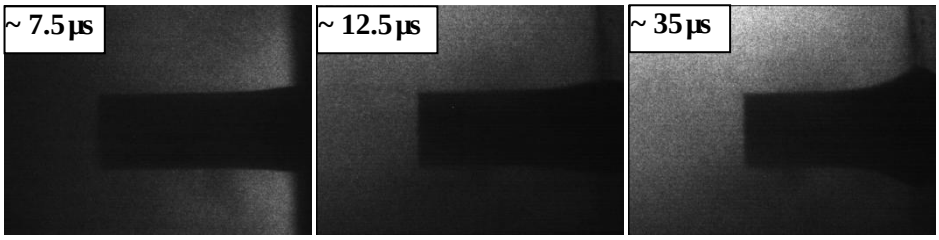

Figure 4.50. Three frames selected for film reduction analysis at V_i = 90.95 m/s (large dimension sample from Batch #3)

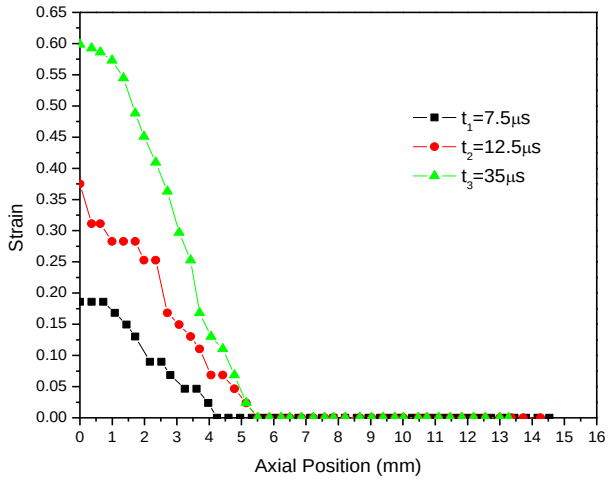

(a)

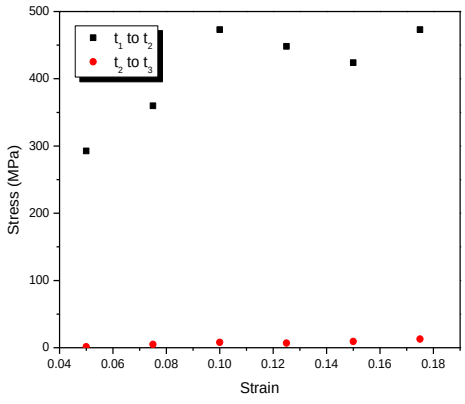

(b)

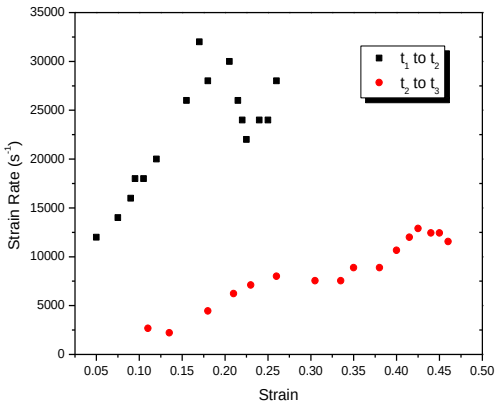

(c)

Figure 4.51. Film data analysis for Batch #3 large dimension sample at V_i = 90.95 m/s, (a) strain *vs.* axial position plots at three different times; (b) stress *vs.* strain curves at two intervals; (c) strain rate *vs.* strain curves at two intervals

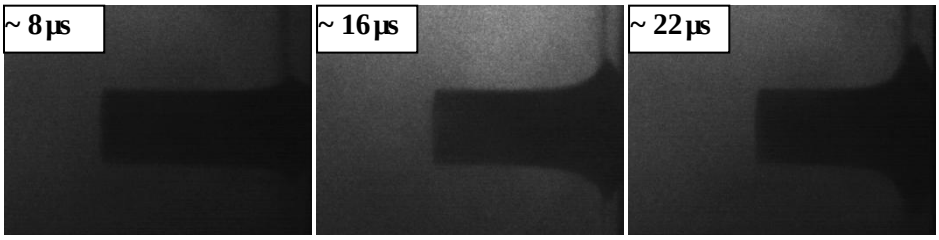

Figure 4.52. Three frames selected for film reduction analysis at V_i = 196.53 m/s (large dimension sample from Batch #3)

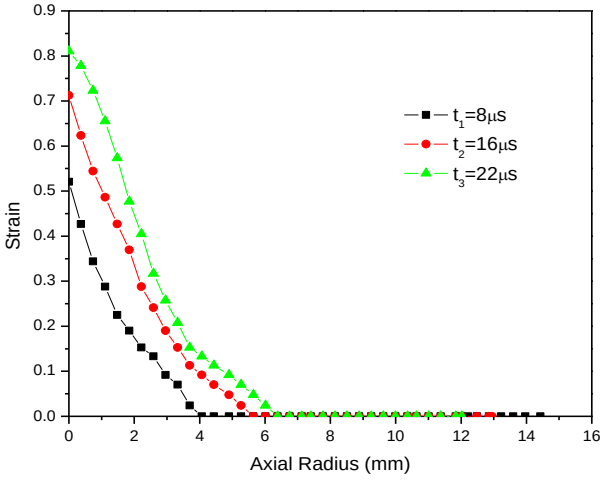

(a)

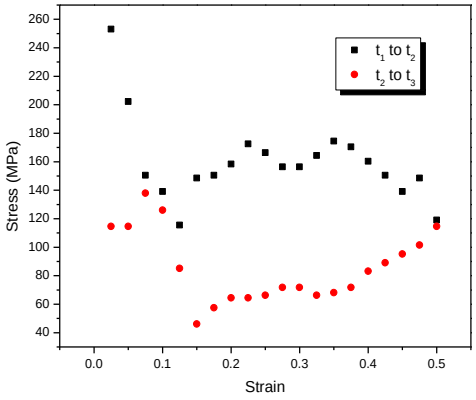

(b)

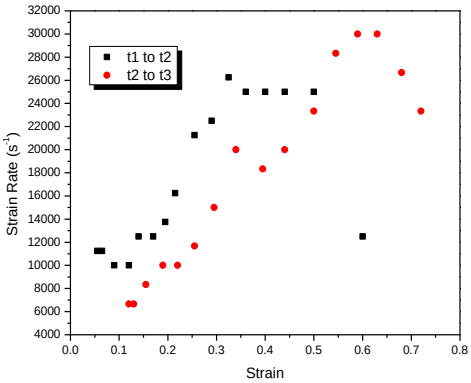

(c)

Figure 4.53. Film data analysis for Batch #3 large dimension sample at V_i = 196.53 m/s, (a) strain *vs.* axial position plots at three different times; (b) stress *vs.* strain curves at two intervals; (c) strain rate *vs.* strain curves at two intervals

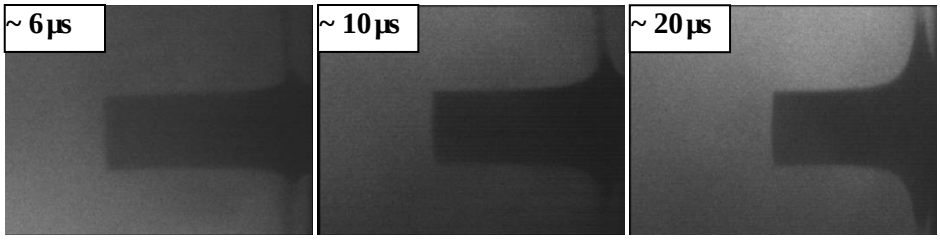

Figure 4.54. Three frames selected for film reduction analysis at V_i = ~ 300 m/s (large dimension sample from Batch #3)

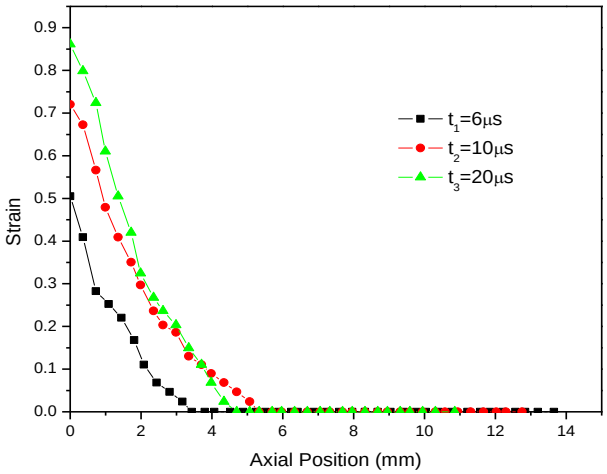

(a)

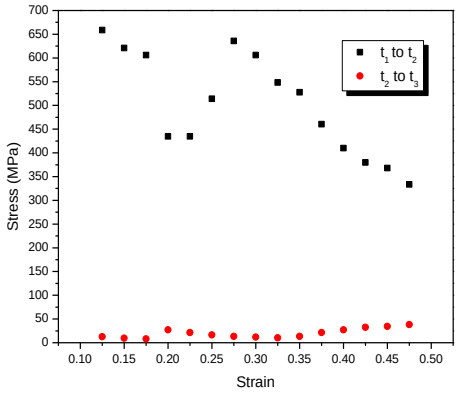

(b)

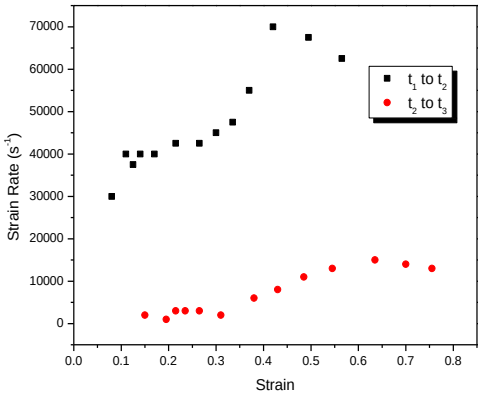

(c)

Figure 4.55. Film data analysis for Batch #3 large dimension sample at V_i = ~ 300 m/s, (a) strain *vs.* axial position plots at three different times; (b) stress *vs.* strain curves at two intervals; (c) strain rate *vs.* strain curves at two intervals

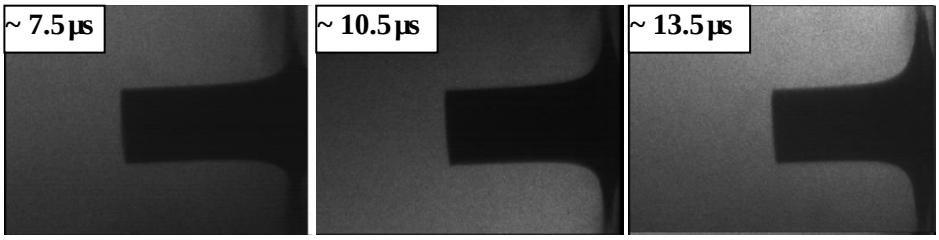

Figure 4.56. Three frames selected for film reduction analysis at V_i = 399.02 m/s (large dimension sample from Batch #3)

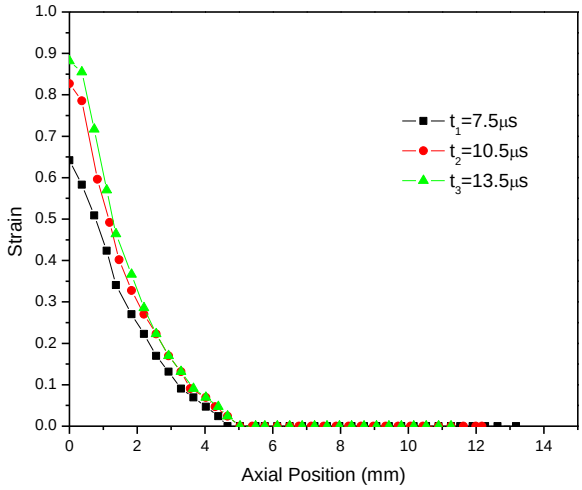

(a)

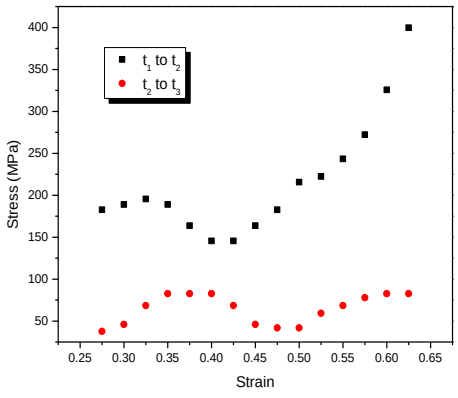

(b)

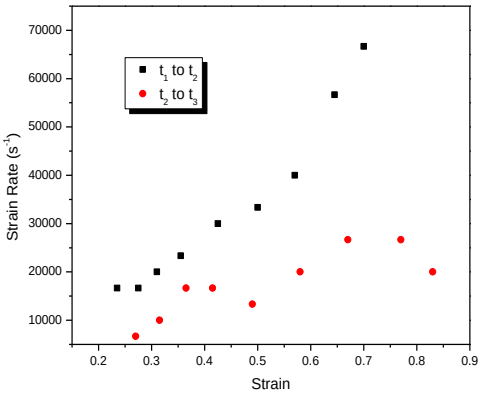

(c)

Figure 4.57. Film data analysis for Batch #3 large dimension sample at V_i = 399.02 m/s, (a) strain *vs.* axial position plots at three different times; (b) stress *vs.* strain curves at two intervals; (c) strain rate *vs.* strain curves at two intervals

The accuracy of stress and strain rate value was highly dependent on the length of time interval selected between frames. In general, as the time interval approached zero, the back end velocity and plastic wave velocity approached the actual value based on their definitions (Equations 4.2 - 4.3), and so did the value of stress and strain rate. However, if the time interval selected between two frames was too close, the uncertainty of the measurement also increased. Proper time intervals were therefore chosen based on the frame quality at each impact serial with consideration of accuracy.

Upon examing the stress / strain rate *vs.* strain curves for the Batch #2 and Batch #3 samples with various imapct velocities, no obvious trend was found. Some of the plots even showed an irregular pattern (e.g., Figure 4.49 (b)) which was believed to be caused by errors introduced by measurement and time interval selections. Nevertheless, as additional information provided for dynamic analysis and consitutive modelling, the plots were used to extract general information about the stress and strain rate accumulation during impact deformation. By comparing the stress *vs.* strain and strain rate *vs.* strain plots between two batches at similar impact velocity, Batch #3 samples exhibited higher stress and strain rate values than Batch #2. The peak stress value at the first time interval for Batch #3 samples ranged from 260 to 650 MPa, while Batch #2 ranged from 55 to 400 MPa. The peak strain rate value at first time interval for Batch #3 samples ranged from 32,000 to 70,000 s^{-1}, and Batch #2 ranged from 20,000 to 70,000 s^{-1}. Since Batch #3 samples had a higher content of Ti particles (67.6 wt%) than did Batch #2 (49 wt%), the hard component had a pronounced reinforcing effect on the composite, so the stress value of Batch #3 samples was significantly higher that of Batch #2. For all the strain rate *vs.* strain profiles, strain rate increased with strain until a certain point was reached, i.e.,

strain rate increased from the end towards the front. For some plots, especially seen in the second time intervals, after a certain critical strain point which was dependent on impact velocity, the strain rate decreased. As an index to describe the rate of change in strain, the estimated strain rate values along the sample provided information on plastic wave propagation. Although as an approximate analysis for impact deformation, the House method still offered a valuable estimation of the stress / strain rate values changing with strain.

4.3.5 Comparison of Taylor Impact Test Results on PTFE 7A / Ti with Different Impact Velocities, Sample Dimensions and Sample Configurations

Subsections 4.3.1 - 4.3.3 described the impact-initiated deformation and chemical reaction for Batches #1, #2 and #3 composite samples. Most of the observations shared common phenomena for all three batches, e.g., the three-stage deformation process, velocity effect and sample dimension effect, but the sample configuration in each batch exerted different effects on the severity of impact-initiated reaction. In this subsection, the separate influences of impact velocity, sample dimension and sample configuration on the impact-initiated reaction will be discussed.

4.3.5.1 Impact-Initiated Reaction

Either ignition light or ignition fume was observed in all three batches at certain impact velocities for medium, small and even smaller dimension samples in the time scale of microseconds, which proved the impact-initiated reactivity of the PTFE 7A / Ti composite system. Due to the intensity of the combustion-like reaction, post-impact product was too small in mass to be gathered for further analyses. In order to collect

enough post-impact product, an alternative Taylor impact test was conducted with the sample attached onto the anvil (Figure 4.58):

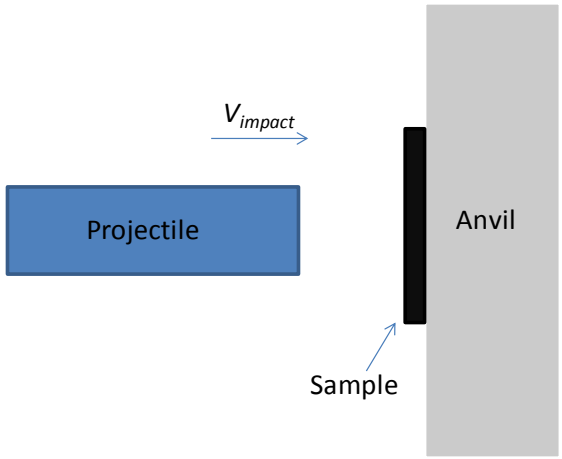

Fig 4.58. The sketch for Taylor impact test setup with sample attached onto anvil

In this manner, some of the reaction debris "stuck" on the hard anvil, and was later scratched off and collected for micro-quantity XRD analyses.

Since the masses of the isolated powders were very small, the *X'Pert PRO MRD diffractometer* was used to accurately measure the existence of any substance in the residue post-impact product (Figure 4.59):

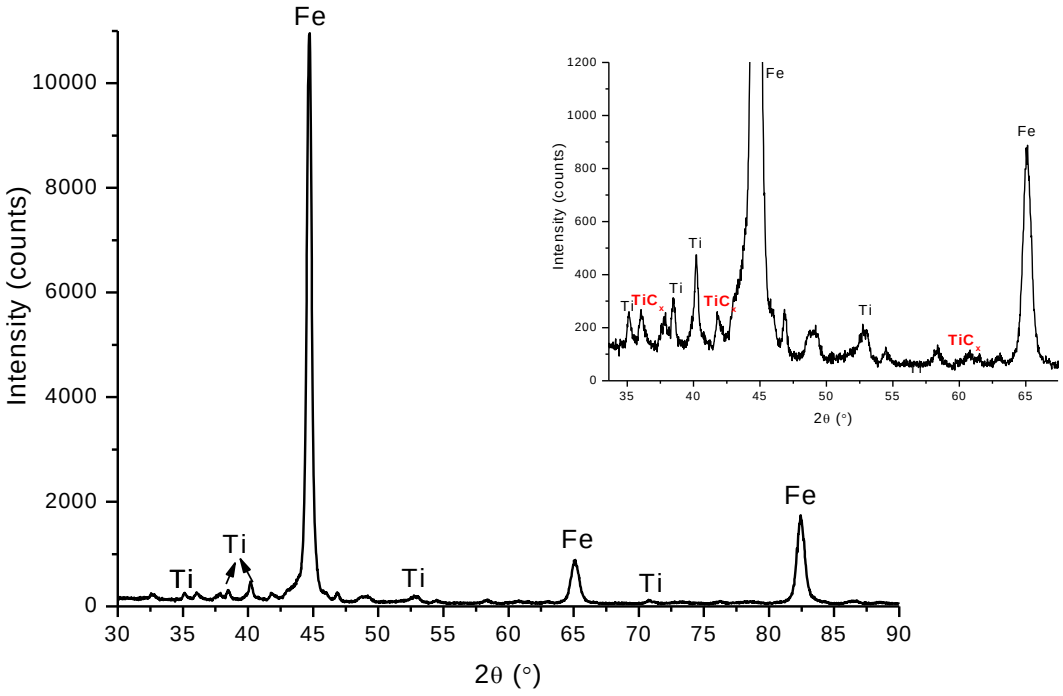

Fig 4.59. XRD patterns of the post-impact product at V_i = ~ 200 m/s (Batch #1)

The most prominent XRD peaks were attributed to the lattice planes from the Ferrum (Fe) substance produced by scratching the anvil, and to the non-reacted Ti. When zooming into the region from 35 ° to 65 °, tiny peaks representing the lattice planes of TiC_x were identified, indicating that TiC_x was indeed one of the main products resulting from the impact-initiated reaction between PTFE 7A and Ti. The detection of TiC_x further confirmed the occurrence of impact-initiated chemical reactions during impact loading and their main product.

Another common phenomenon shared with all three batches was the three-stage deformation for triggering the impact-initiated chemical reactions. For all the medium and small dimension samples with impact-initiated reactions detected, the reaction light /

fume all came from the shear band region. By comparing the critical axial / areal strains in three cases, similar value ranges were found disregarding various impact velocities and sample configurations (Figure 4.6, 4.14 and 4.29). In conclusion, the impact-initiated reaction between PTFE 7A / Ti was shear strain / stress-induced, since the reaction was not triggered immediately once the accelerated sample contacted the anvil, but only after the deformation of the sample reached a certain critical point. The shear (deviatoric) component of stress generated under impact loading has been regarded as the predominant factor to trigger the impact-initiated chemical reaction by the displacement between atoms and a lowering of the activation energy [2, 86]. In this study, the annular shear band region at the rear part of the composite sample had a much higher shear strain due to the "punching" effect produced by the copper projectile, hence providing the sample components in that area the most prominent displacement and intimate atom contact. The first ignition light / fume thus emanated from the shear band region.

4.3.5.2 The Effect of Impact Velocity on the Impact-Initiated Reaction

Impact velocity is a predominant factor for triggering the impact-initiated reaction since it is related to the kinetic energy ($E = \frac{1}{2}mv^2$), which directly determines if the threshold of the initiation energy of the chemical reaction is reached. Figures 4.7, 4.15 and 4.30 showed an increasing rate of ignition time as the kinetic energy decreased. By fitting each plot with the *Dhyperbl* function, a critical value of kinetic energy was obtained for each batch with medium dimensions. In this sense, the impact velocity (or kinetic energy with fixed sample mass) was a necessary condition to determine if the impact-initiated reaction would be able to take place. In other words, once the impact-

initiated reaction was triggered, the impact velocity / kinetic energy had to exceed a certain critical value. However, in the opposite sense, the impact velocity / kinetic energy alone could not determine whether or not the reaction had taken place. As a result, under similar kinetic energy levels, the large dimension samples (Batch #2 and #3 samples) with impact velocity of ~ 500 m/s did not emit any reaction light / fume until the very end of the detection period. Beside the kinetic energy, another necessary condition — shear strain / shear stress-jointly guarantee the occurrence of the impact-initiated reaction.

4.3.5.3 The Effect of Sample Dimension on the Impact-Initiated Reaction

As discussed in Subsections 4.3.1 - 4.3.3, sample dimension had a significant effect on ignition time and severity of the impact-initiated reaction. Figures 4.60 - 4.62 show three series of comparisons among medium, small and even smaller dimension samples with similar impact velocities:

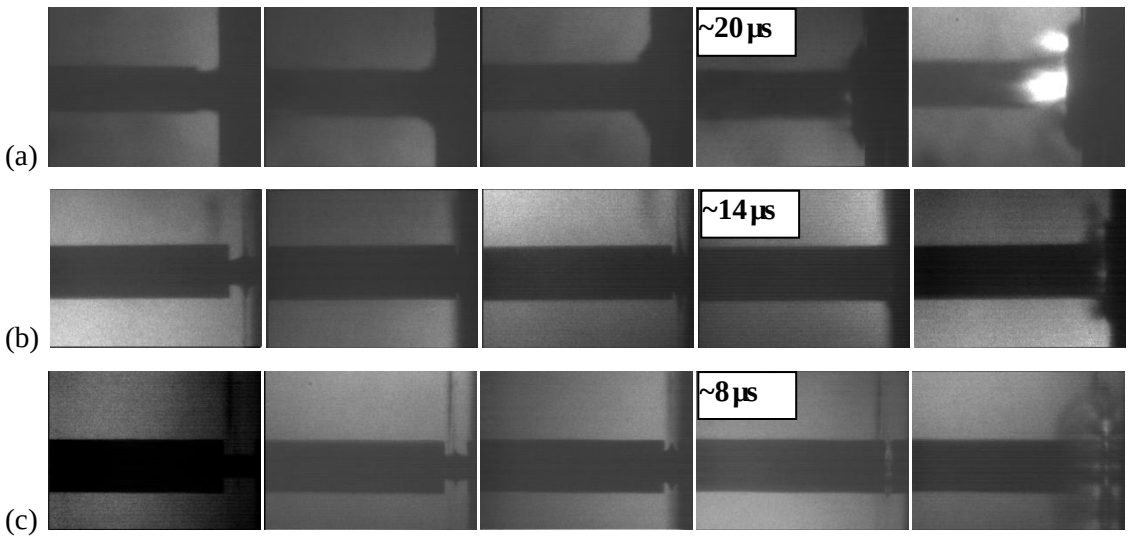

Figure 4.60. Consecutive images of the Taylor impact test on PTFE 7A / Ti composite of Batch #1 (a) medium dimension sample at V_i = 308 m/s; (b) small dimension sample at V_i = 309 m/s; (c) even smaller dimension sample at V_i = ~300 m/s

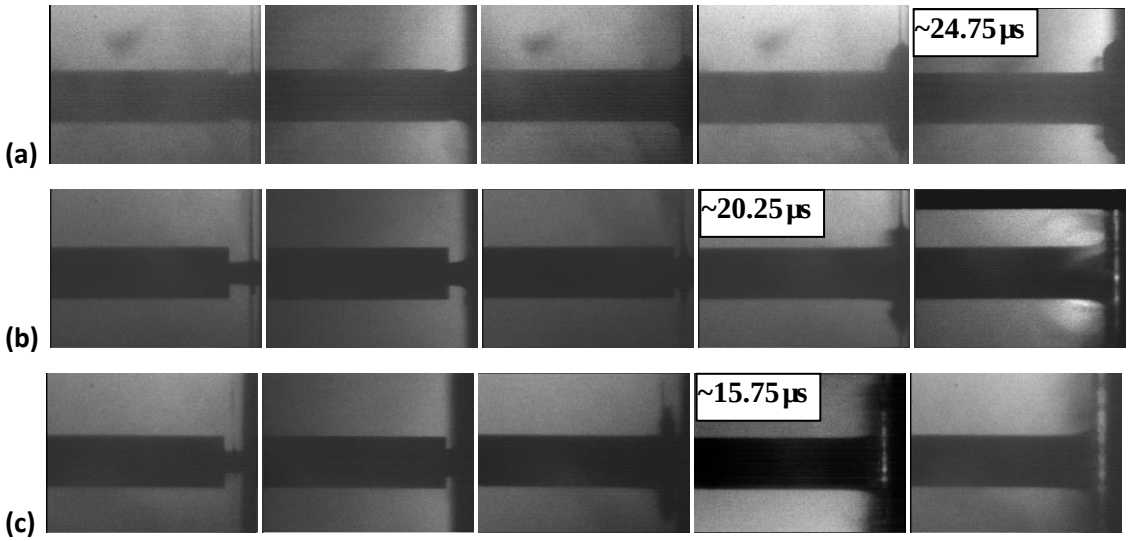

Figure 4.61. Consecutive images of the Taylor impact test on PTFE 7A / Ti composite of Batch #2 (a) medium dimension sample at V_i = 201 m/s, (b) small dimension sample at V_i = 199 m/s, (c) even smaller dimension sample at V_i = 203 m/s

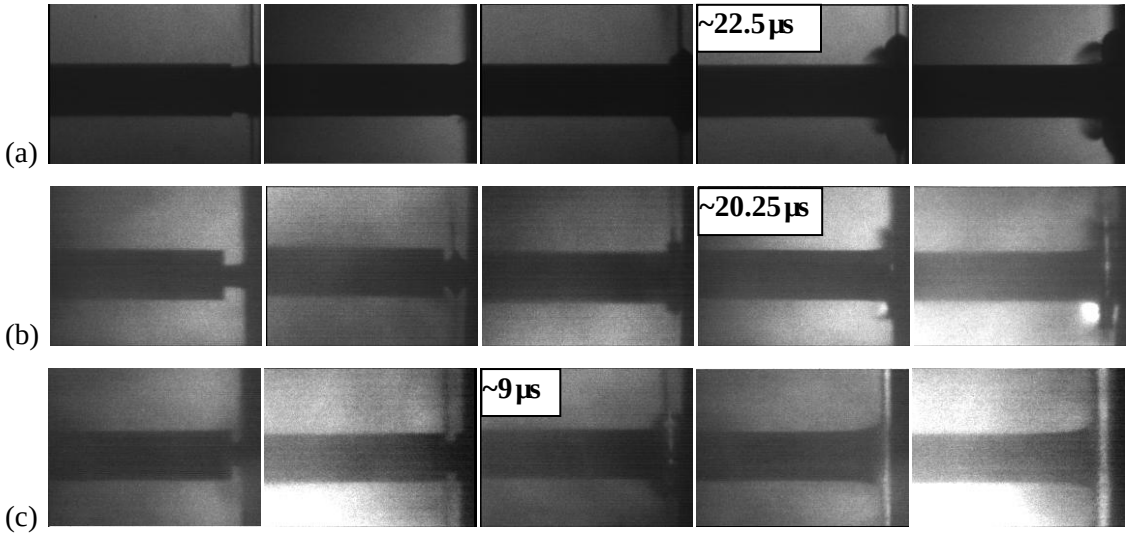

Figure 4.62. Consecutive images of the Taylor impact test on PTFE 7A / Ti composite of Batch #3 (a) medium dimension sample at V_i = 205 m/s; (b) small dimension sample at V_i = 201 m/s; (c) even smaller dimension sample at V_i = 204 m/s

In each sequence, as the sample dimension decreased, the ignition time also decreased.

For the Batch #2, the medium dimension sample only emitted light ignition fume at ~

24.75 μs, while the small dimension sample first showed ignition fume at ~ 20.25 μs, and then evolved into an intense flash of light after several frames during the detection period. The even smaller dimension sample showed ignition light directly at ~ 15.75 μs. For Batch #3, the medium dimension samples only showed ignition fume throughout the detection period, while small and even smaller dimension samples directly showed ignition light at an early stage of impact deformation. The conclusion was reinforced that the smaller the sample dimension, the shorter the ignition time and the more severe the reaction.

The sample dimension effect expected to influence the time scale of impact-initiated reaction. With similar initial kinetic energy, the small dimension sample had a larger impact energy per unit volume, which led to higher shear strain / stress on the same time scale as the large dimension sample, resulting in a shorter ignition time.

4.3.5.4 The Effect of Sample Configuration on the Impact-Initiated Reaction

As presented in Subsections 4.3.1 - 4.3.3, the impact deformation processes were similar in all three batch samples, while the impact-initiated reaction among them showed significant differences. Two comparisons were made at the impact velocity of ~ 300 m/s and ~ 200 m/s for three batches with medium dimension, and the severity of the reaction in each batch was compared (Figure 4.63 - 4.64, Table 4.2).

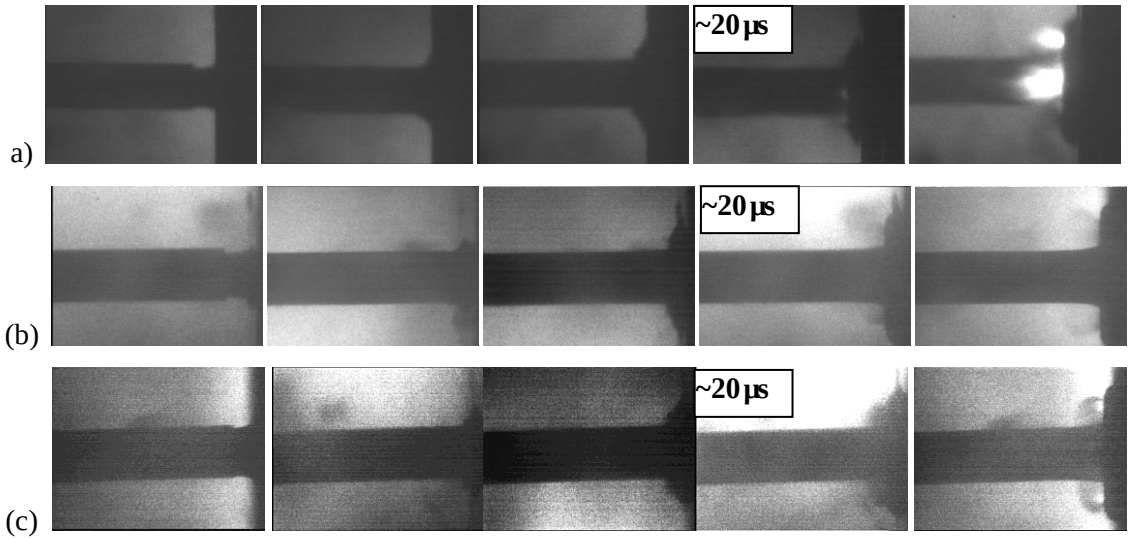

Figure 4.63. Comparison of consecutive images of the Taylor impact test on PTFE 7A / Ti medium dimension composite (a) Batch #1 at V_i = 308 m/s; (b) Batch #2 at V_i = 304 m/s; (c) Batch #3 at V_i = 281 m/s

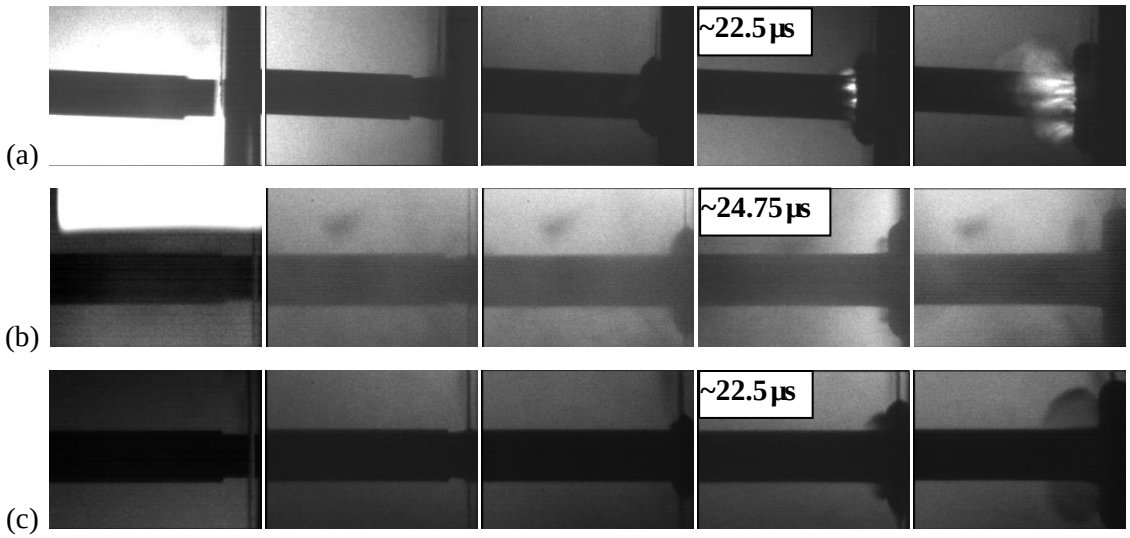

Figure 4.64. Comparison of consecutive images of the Taylor impact test on PTFE 7A / Ti medium dimension composite (a) Batch #1 at V_i = 188.73 m/s; (b) Batch #2 at V_i = 200.96 m/s; (c) Batch #3 at V_i = 204.59 m/s

Table 4.2. Comparison of the reactivity and critical axial / areal strains among three batches of PTFE 7A / Ti composite (medium dimensions) at 200 m/s and 300 m/s impact velocities

PTFE 7A / Ti composite	Ignition time (μs)	Critical axial strain	Critical areal strain	The severity of reaction
~ 200 m/s				
Batch #1	~ 22.5	~ 134%	~ 48%	Severe (reaction light)
Batch #2	~ 24.75	~ 164%	~ 58%	Light (reaction fume)
Batch #3	~ 22.5	~ 170%	~ 59%	Less severe (reaction fume)
~300 m/s				
Batch #1	~ 20	~ 143%	~ 67%	Severe (reaction light)
Batch #2	~ 20	~ 185%	~ 64%	Light (reaction fume)
Batch #3	~ 20	~ 187%	~ 63%	Less severe (reaction fume, then light)

In Figure 4.63, at an impact velocity of ~ 300 m/s, although the ignition time for all three batch samples showed similar values, the severity of each reaction differed substantially: the Batch #1 sample exhibited ignition light directly at ~ 20 μs; the Batch #2 sample showed ignition fume throughout the deformation process; and the Batch #3 sample showed ignition fume first at ~ 20 μs followed by ignition light. In Figure 4.64, at the impact velocity of ~ 200 m/s, the deformation and reaction severity for the three batch samples exhibited similar trends. The Batch #1 sample showed ignition light directly at ~ 20 μs, while the Batch #2 and #3 samples did not show reaction light during the entire detection period, but the reaction fume from Batch #3 was more evident and stronger than with Batch #2. In conclusion, the severity of the reaction followed the order: Batch #1 > Batch #3 > Batch #2.

Recall the differences in constitution and SEM images among the three batches (Figure 3.1): the Batch #1 composite shared the same constitution as Batch #2, but in a

less uniform distribution with Ti particles aggregated in the PTFE 7A matrix; and the Batch #3 composite was a well-dispersed, Ti-rich system, so the local extent of Ti aggregation in Batch #3 was higher than that of Batch #2, but not as high as in Batch #1. In summary, the extent of Ti aggregation also followed the order: Batch #1 > Batch #3 > Batch #2. The effect of composite configuration on impact-initiated reaction was therefore attributed to the localized deformation favored in a Ti-aggregated morphology. In the Ti-aggregated morphology, the PTFE 7A component was more likely to be trapped by the Ti component compared with a uniform morphology. In this case, the soft component PTFE 7A was partially encompassed by the hard segment Ti, which hindered the further deformation of PTFE 7A particles upon impact loading, and thus restricting the deformation and interaction of PTFE 7A and Ti to a localized area.

Similar phenomena were earlier reported by Eakins and Thadhani, where they found that the flake Ni / spherical Al system required a lower shock energy for compound formation compared with the spherical Ni / Al system [9, 87]. The researchers later simulated the shock compression process for both systems and found that the flake Ni / spherical Al system had a larger interface area than that of the spherical Ni / Al system, which resulted in higher localized temperature and pressure generation [8]. The results were explained by the "hard encompassing soft" structure, in which the soft component Al was trapped by the flake shaped, hard component Ni, localizing the deformation, pressure, and temperature. For the effect of sample configuration on the reactivity of impact-initiated reaction, microstructural simulation was conducted to verify the theoretical assumption proposed in this subsection (see Chapter VI).

4.4 Summary

Taylor impact test results on large, medium, small, and even smaller dimension samples from three batches at various impact velocities ranging from ~ 100 to ~ 500 m/s were shown and discussed from different aspects:

(1) Ignition light / fume, an indication of impact-initiated reaction, was observed for medium, small and even smaller dimension samples for all PTFE 7A / Ti composite batches at certain impact velocity ranges. Ignition light confirmed the impact reactivity of the PTFE 7A / Ti composite systems in the time scale of microseconds.

(2) The impact-initiated reactivity was dependent on both the impact velocity (kinetic energy) and the shear strain / stress value. In other words, only when both the impact velocity (kinetic energy) and the shear component of strain / stress exceeded certain threshold values, did the impact-initiated reaction take place.

(3) The sample dimension had a remarkable effect on the ignition time and the severity of reaction. As the sample dimension reduced, the ignition time decreased, and the severity of the reaction increased.

(4) By comparing the configuration and reactivity of three batches, the impact-initiated reaction of the PTFE 7A / Ti composite was concluded to prefer a Ti-aggregated structure. The "hard-encompassing-soft" structure was able to resist the particle deformation in regions, thus localizing the stress and temperature accumulation to accelerate the reaction.

CHAPTER V

COMPUTATIONAL ANALYSIS OF TAYLOR IMPACT TEST ON PTFE 7A / TI COMPOSITE

5.1 Constitutive Modeling

As described in Subsections 2.5.2 and 2.5.5, the constitutive model applied on PTFE 7A / Ti composite system was based on the modified Johnson-Cook strength model developed by Raftenberg et al. [14]. The format of the modified Johnson-Cook model was reviewed in Subsection 2.5.5 and is repeated in Equations 5.1 - 5.4:

$$\sigma\left(\varepsilon^{p},\theta,\dot{\varepsilon}\right)=\left[\hat{A}\left(\dot{\varepsilon}\right)+\hat{B}\left(\dot{\varepsilon}\right)\cdot\left(\varepsilon^{p}\right)^{\hat{N}(\dot{\varepsilon})}\right]\left(\frac{\theta_m-\theta}{\theta_m-\theta_r}\right) \tag{5.1}$$

where,

$$\hat{A}\left(\dot{\varepsilon}\right)=A_0+A_1\sinh^{-1}\left(\frac{\dot{\varepsilon}}{2\dot{\varepsilon}_0}\right) \tag{5.2}$$

$$\hat{B}\left(\dot{\varepsilon}\right)=B_0(B_1)^{\hat{N}(\dot{\varepsilon})} \tag{5.3}$$

$$\hat{N}\left(\dot{\varepsilon}\right)=N_0+N_1\sinh^{-1}\left(\frac{\dot{\varepsilon}}{2\dot{\varepsilon}_0}\right) \tag{5.4}$$

In the above equations, the von Mises effective stress, σ, is a function of the plastic strain ε^p, strain rate $\dot{\varepsilon}$ and temperature θ. This model contains the seven unknown parameters A_0, A_1, B_0, B_1, N_0, N_1 and θ_m, all of which needed to be determined experimentally. The temperature θ_m is defined as that corresponding to zero strength. The normalizing strain

rate $\dot{\varepsilon}_0$ was chosen to be 1.0 s^{-1}. By assuming an adiabatic, constant density and constant strain rate process, while also neglecting the work associated with elastic deformation, First Law of Thermodynamics was applied to the rapid deformation process, so that the change in internal energy per unit mass was equal to the increment in plastic work per unit mass by (Equation 5.5):

$$de = dW_p \tag{5.5}$$

After a sequence of derivations and operations, the final expression of the von Mises effective stress σ is given in Equation 5.6 and 5.7 [14]:

$$\sigma^{adiab}\left(\varepsilon^p, \dot{\varepsilon}_*\right) = \left(\frac{\theta_m - \theta_i}{\theta_m - \theta_r}\right)\left[\hat{A}\left(\dot{\varepsilon}_*\right) + \hat{B}\left(\dot{\varepsilon}_*\right)\cdot\left(\varepsilon^p\right)^{\hat{N}\left(\dot{\varepsilon}_*\right)}\right]\cdot\exp\left[-\phi\left(\varepsilon^p, \dot{\varepsilon}_*\right)\right] \tag{5.6}$$

where,

$$\phi\left(\varepsilon^p, \dot{\varepsilon}_*\right) = \frac{1}{\rho_0 c_\upsilon\left(\theta_m - \theta_r\right)}\left[\hat{A}\left(\dot{\varepsilon}_*\right)\cdot\varepsilon^p + \frac{\hat{B}\left(\dot{\varepsilon}_*\right)}{\hat{N}\left(\dot{\varepsilon}_*\right)+1}\cdot\left(\varepsilon^p\right)^{\hat{N}\left(\dot{\varepsilon}_*\right)+1}\right] \tag{5.7}$$

Results from the Instron and SHPB tests (see Chapter III) were used for fitting in the modified Johnson-Cook model to determine the seven unknown parameters, A_0, A_1, B_0, B_1, N_0, N_1 and θ_m. The detailed fitting process has been elaborated in reference [14], and the four main steps are generalized here:

(1) Estimate Young's modulus E from the elastic regions of the curves from the Instron and SHPB test.

(2) Convert the true strain into the plastic strain in the stress *vs.* strain curves by:

$$\varepsilon_p = \varepsilon - \frac{\sigma}{E} \tag{5.8}$$

(3) Fit the stress *vs.* plastic strain curve with Equation 5.6 by using the *lsqcurvefit* function in the *Matlab* software (Appendix A.1) to obtain four constants, $\hat{A}(\dot{\varepsilon})$, $\hat{B}(\dot{\varepsilon})$, $\hat{N}(\dot{\varepsilon})$ and θ_m at two specific strain rates (Figures 5.1 - 5.2). Two sets of constants were obtained from both the Instron test (0.01 s^{-1}) and the SHPB test (3100 s^{-1}) (Tables 5.1 - 5.2):

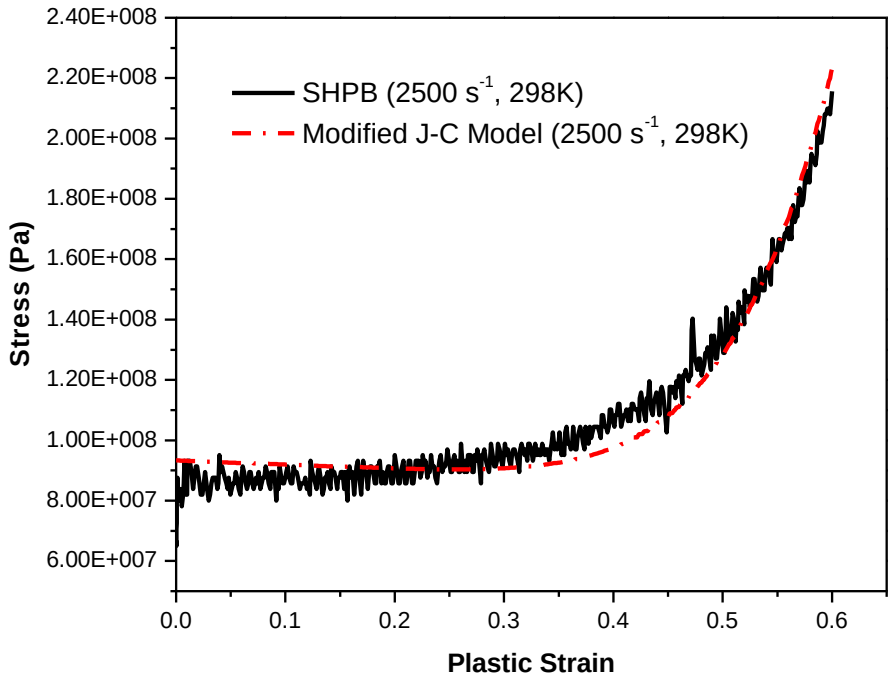

Figure 5.1. The experimental (black line) and fitted (red dot line) stress *vs.* strain curves of the PTFE 7A / Ti composite at the strain rate of 2500 s^{-1}

Table 5.1. Constants obtained from the SHPB test at the strain rate around 2500 s^{-1}

ρ_0 (kg/m^3)	C_v (J/kg-K)	E (2500 s^{-1}) (GPa)	A (2500 s^{-1}) (MPa)	B (2500 s^{-1}) (GPa)	N (2500 s^{-1})	θ_m (K)
2840	768.6	18.14	93.29	4.78	6.72	593

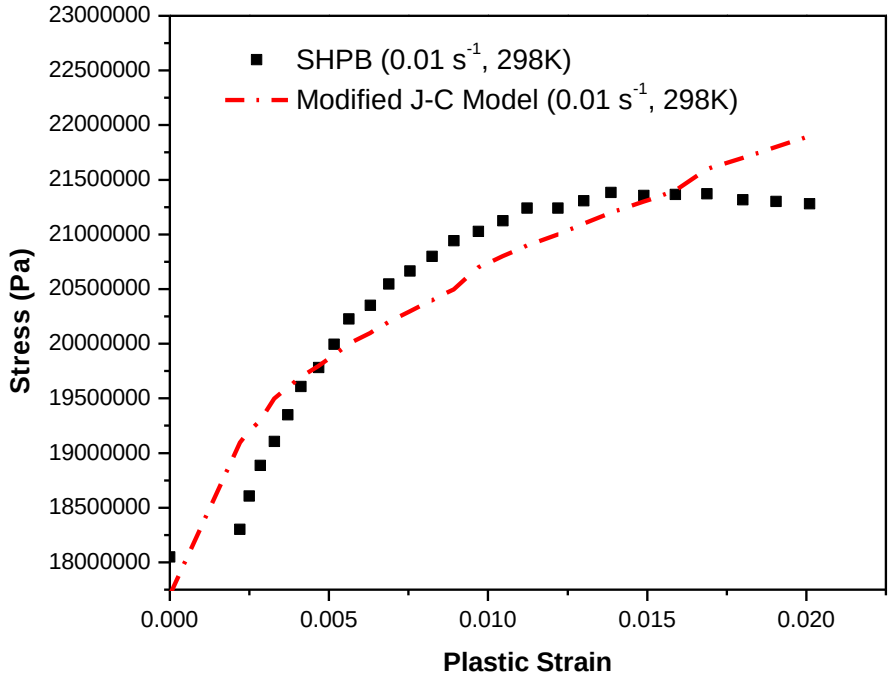

Figure 5.2. The experimental (black dot) and fitted (red dash dot) stress *vs.* strain curves of the PTFE 7A / Ti composite at the strain rate of 0.01 s^{-1}

Table 5.2. Constants obtained from Instron test at the strain rate of 0.01 s^{-1}

ρ_0 (kg/m^3)	C_v (J/kg-K)	E (0.01 s^{-1}) (MPa)	A (0.01 s^{-1}) (MPa)	B (0.01 s^{-1}) (MPa)	N (0.01 s^{-1})	θ_m (K)
2840	768.6	418	17.66	27.07	0.4741	593

(4) Obtain the rest of the parameters A_0, A_1, B_0, B_1, N_0 and N_1 by evaluating Equations 5.2 - 5.4 at the two specific strain rates (Table 5.3):

Table 5.3 Parameters in the modified J-C model for the PTFE 7A / Ti composite

A_0 (MPa)	A_1 (MPa)	B_0 (MPa)	B_1	N_0	N_1	$\dot{\varepsilon}$ (s^{-1})	θ_m (K)
17.61	9.673	18.25	2.290	0.469	0.799	1	593

Samples from Batch #2 (51 wt% PTFE 7A / 49 wt% Ti with uniform distribution) were selected from the data generated with Instron and SHPB tests, and the fitted parameters to the modified Johnson-Cook model were specifically for this particular constitution and configuration.

In order to validate the modified Johnson-Cook model at other strain rates, the fitted model was applied to the SHPB data points at 3600 s^{-1} (Figure 5.3):

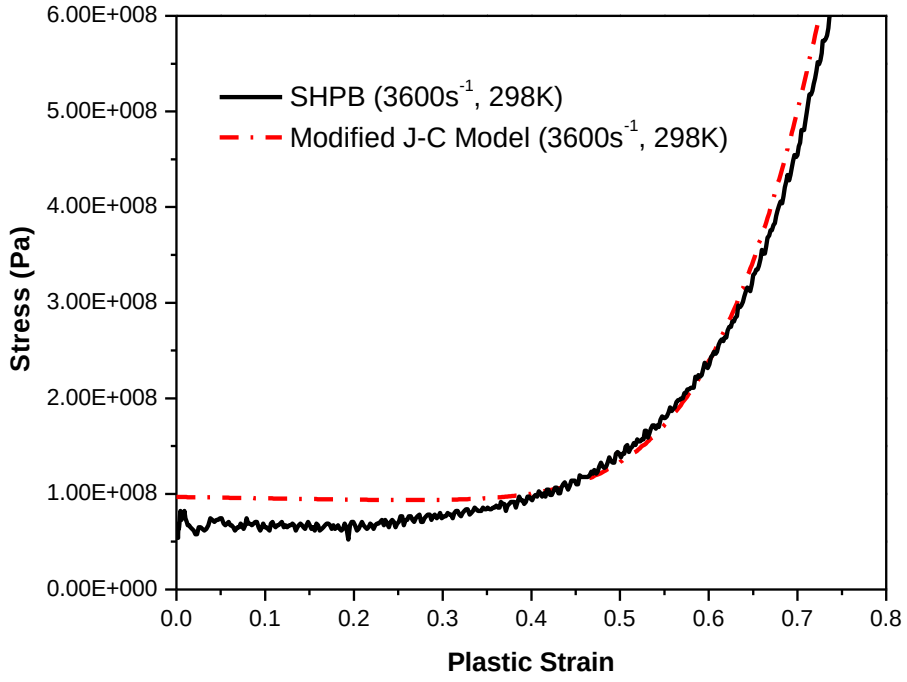

Figure 5.3. The experimental (black line) and fitted (red dash dot) stress *vs.* strain curves of the PTFE 7A / Ti composite at the strain rate of 3600 s^{-1}

Except for the initial deviation from the experimental data, the modified Johnson-Cook model could give reasonably good fitting results at high strain rates. The parameters shown in Table 5.3 were therefore adopted for the modified Johnson-Cook model. The constitutive relationships for Finite Element Analysis (FEA) simulation are shown in Equations 5.9 - 5.13:

$$\sigma_{JCP}^{adiab}\left(\varepsilon^{p},\dot{\varepsilon}_{*}\right)=\left(\frac{593-\theta_{i}}{593-\theta_{r}}\right)\left[\hat{A}\left(\dot{\varepsilon}_{*}\right)+\hat{B}\left(\dot{\varepsilon}_{*}\right)\cdot\left(\varepsilon^{p}\right)^{\hat{N}\left(\dot{\varepsilon}_{*}\right)}\right]\cdot\exp\left[-\phi\left(\varepsilon^{p},\dot{\varepsilon}_{*}\right)\right] \tag{5.9}$$

where,

$$\phi\left(\varepsilon^{p},\dot{\varepsilon}_{*}\right)=\frac{1}{2840\cdot 768.6\cdot\left(593-\theta_{r}\right)}\left[\hat{A}\left(\dot{\varepsilon}_{*}\right)\cdot\varepsilon^{p}+\frac{\hat{B}\left(\dot{\varepsilon}_{*}\right)}{\hat{N}\left(\dot{\varepsilon}_{*}\right)+1}\cdot\left(\varepsilon^{p}\right)^{\hat{N}\left(\dot{\varepsilon}_{*}\right)+1}\right] \tag{5.10}$$

$$\hat{A}\left(\dot{\varepsilon}\right)=17.61+9.673\cdot\sinh^{-1}\left(\dot{\varepsilon}/2\right) \tag{5.11}$$

$$\hat{B}\left(\dot{\varepsilon}\right)=18.25(2.29)^{\hat{N}\left(\dot{\varepsilon}\right)} \tag{5.12}$$

$$\hat{N}\left(\dot{\varepsilon}\right)=0.469+0.799\cdot\sinh^{-1}\left(\dot{\varepsilon}/2\right) \tag{5.13}$$

Based on the fitted constitutive relationship shown in Equations 5.9 - 5.13, the stress-strain-strain rate plane (the plot code is shown in Appendix A.2) of the PTFE 7A / Ti composite is provided in Figure 5.4 for later incorporation into *Abaqus* software to simulate the deformation process during the Taylor impact test:

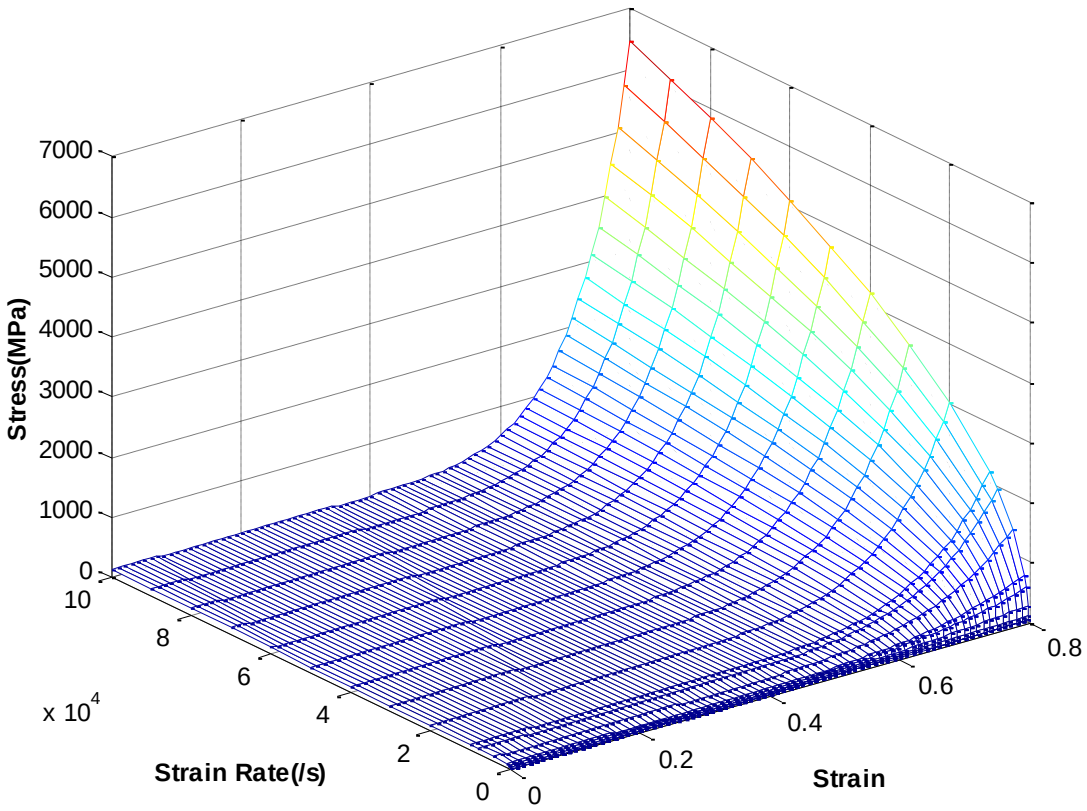

Figure 5.4. The stress-strain-strain rate plane for the PTFE 7A / Ti composite

Simulation results can on the one hand help to validate the constitutive relation, and on the other hand to provide more detailed information such as stress / strain / temperature contours, strain rates scale, etc., to help better understand the initiation and mechanism of the impact-initiated chemical reaction in the PTFE 7A / Ti system.

5.2 Results and Analyses

In this section, simulation results of Taylor impact test on the PTFE 7A / Ti composite (Batch #2, with large, medium, small and even smaller dimensions) were analyzed and compared with the experimental data obtained from the high-speed photography by using the *Abaqus Explicit* program (detailed procedures are shown in Appendix B.2). Table 5.4 displays the input material parameters of the Batch #2 PTFE 7A / Ti composite:

Table 5.4. Input material parameters for the Batch #2 PTFE 7A / Ti composite

Density (t/mm^3)	Young's modulus (MPa)	Poisson's ratio	Expansion coefficient (1/℃)	Specific heat (mJ/t·℃)	Inelastic heat fraction
2.81×10^{-9}	519	0.37	1.4×10^{-5}	7.686×10^{8}	0.5

5.2.1 Simulation Results of Large Dimension Samples

The simulation model setups for large dimension Batch #2 samples are shown in Table 5.5:

Table 5.5. Input sample dimensions for the PTFE 7A / Ti Batch #2 composite, large dimension

Simulation Setups / Velocity (m/s)	Sample diameter (mm)	Sample length (mm)	Sample mass (g)	Anvil diameter (mm)
112.38	7.48	21.00	2.7276	50
201.01	7.48	21.45	2.7877	50
282.56	7.48	20.98	2.7221	50
406.44	7.48	20.74	2.7038	50

Taylor impact tests with four different impact velocities ranging from ~ 100 m/s to ~ 400 m/s were simulated in *Abaqus* to validate the modified Johnson-Cook constitutive model.

Figure 5.5 shows the stress contours of Batch #2 large dimension sample's cross-section at each impact stage with the time interval of 2.5 μs at the impact velocity of 112.38 m/s:

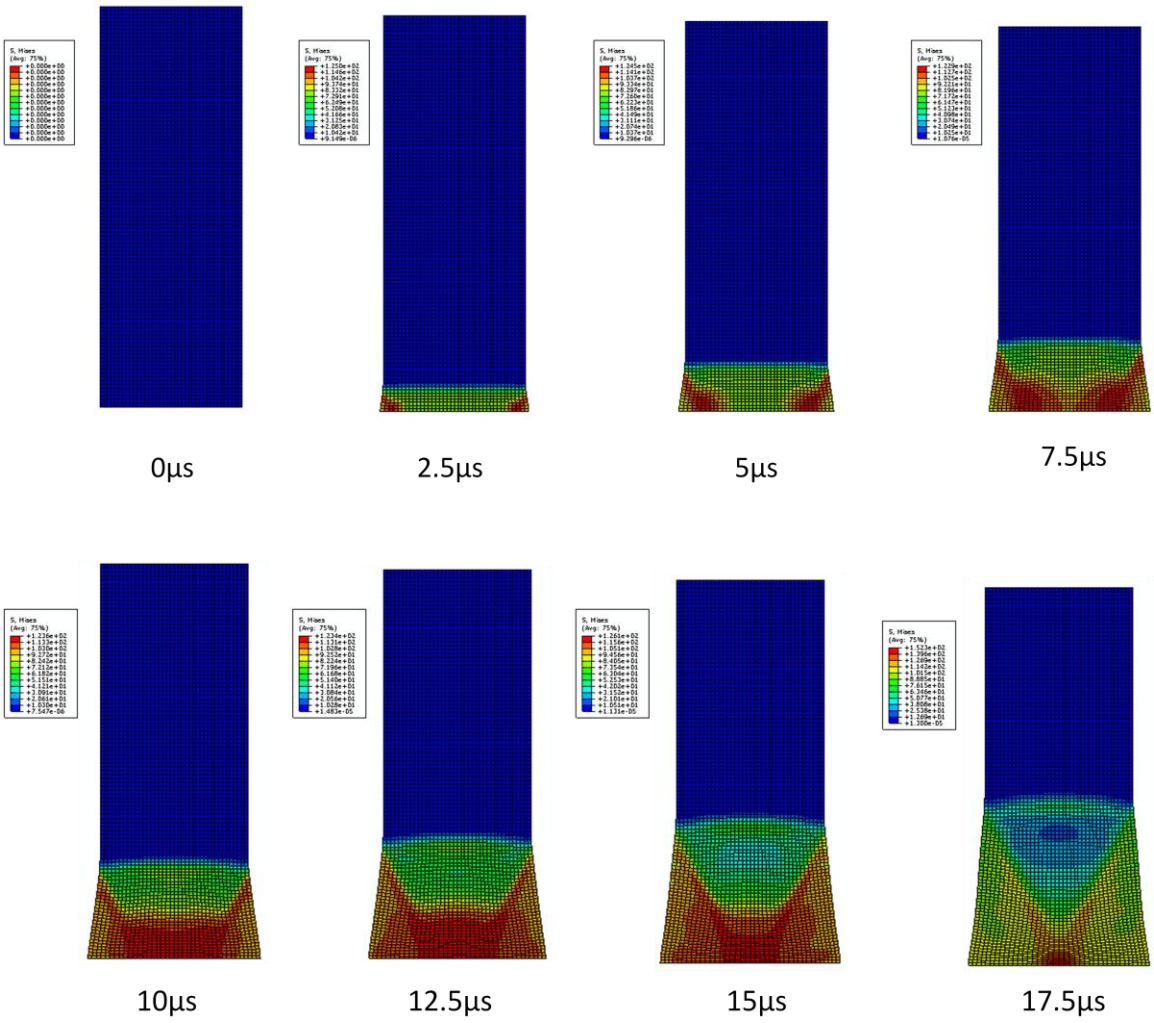

Figure 5.5. Simulation results of the Taylor impact test at V_i = 112.38 m/s (Batch #2)

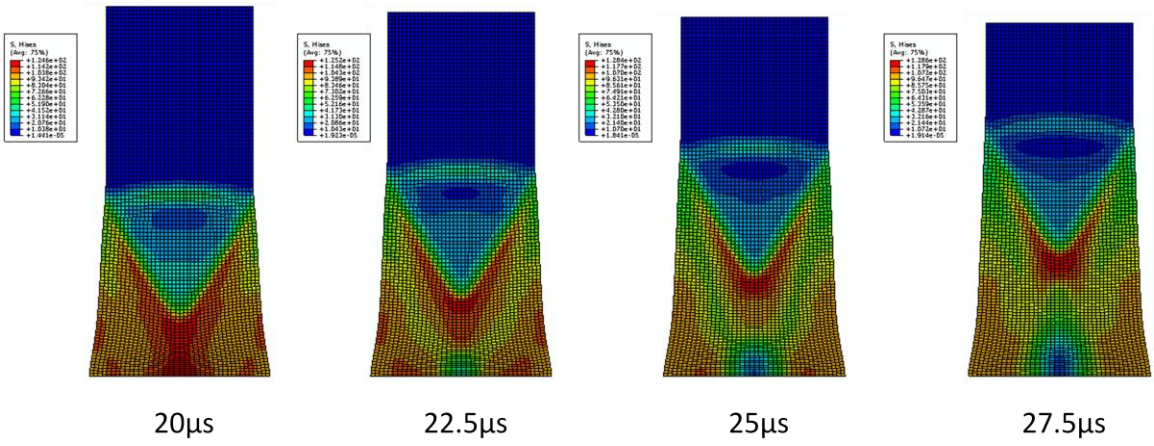

Figure 5.5. Continued

Examining the stress contours in Figure 5.5, the maximum internal stress at 2.5 µs (red areas) took place at the circumference of the front impact surface. As the impact process proceeded, the maximum internal stress moved to the central area of the cylindrical sample, while also traveling towards the rear end of the sample. The values of the maximum internal stresses were in the range of 124 to 152 MPa, varying little during the impact process.

Figures 5.6 - 5.8 compare the simulation results with experimental images by measuring sample radii at certain axial intervals in *Photoshop* at 5 µs, 15 µs and 22.5 µs:

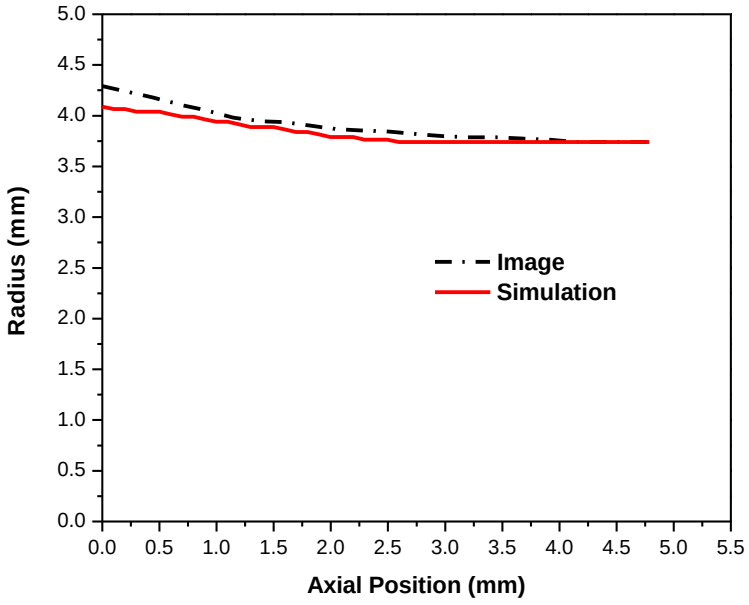

Figure 5.6. Comparison plots of radius *vs.* axial position between the experimental image and simulation results at 5 μs, V_i = 112.38 m/s

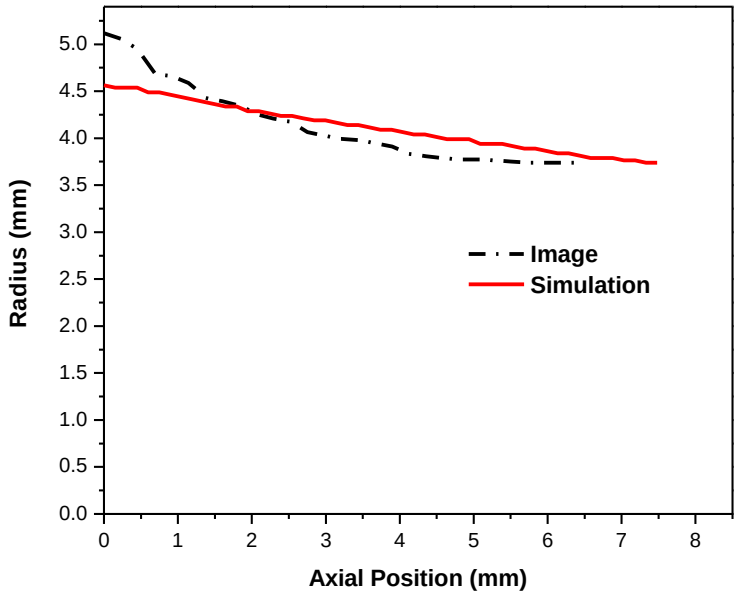

Figure 5.7. Comparison plots of radius *vs.* axial position between the experimental image and simulation results at 15 μs, V_i = 112.38 m/s

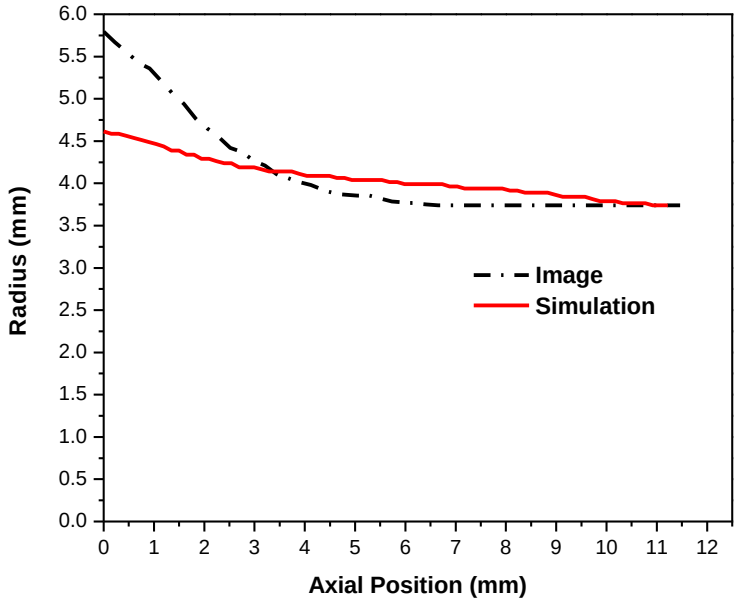

Figure 5.8. Comparison plots of radius *vs.* axial position between the experimental image and simulation results at 22.5 μs, V_i = 112.38 m/s

At 5 μs, simulation results of the sample radius were a slightly smaller than the values measured from images. The maximum difference between simulation results and experimental data at the front impact surface was about 6%. At 15 μs, the simulation radius profile started deviating from experimental data points, especially at the front impact surface where the radius difference was as much as 10%. The simulation radius profile also showed bulge at the rear part of the sample compared with the experimental profile. At 22.5 μs, the disagreements with experimental profile were more evident, and the radius difference at the front surface reached 20%. The bulge also moved towards the rear part of the sample. Taking into account the pixel observation error in the image measurement, the simulation radius profile can reasonably describe the deformation behavior of the PTFE 7A / Ti composite at early stages of the impact process at 112.38

m/s. As time went on, the disagreements on radius profiles became more and more obvious, especially at the front impact surface. A bulge appeared after a certain impact period at the rear part of the sample, and it moved towards the back part of sample as impact proceeded.

Figure 5.9 shows the stress contours of large dimension sample's cross-section at each impact stage with the time interval of 2 μs at the impact velocity of 201.01 m/s:

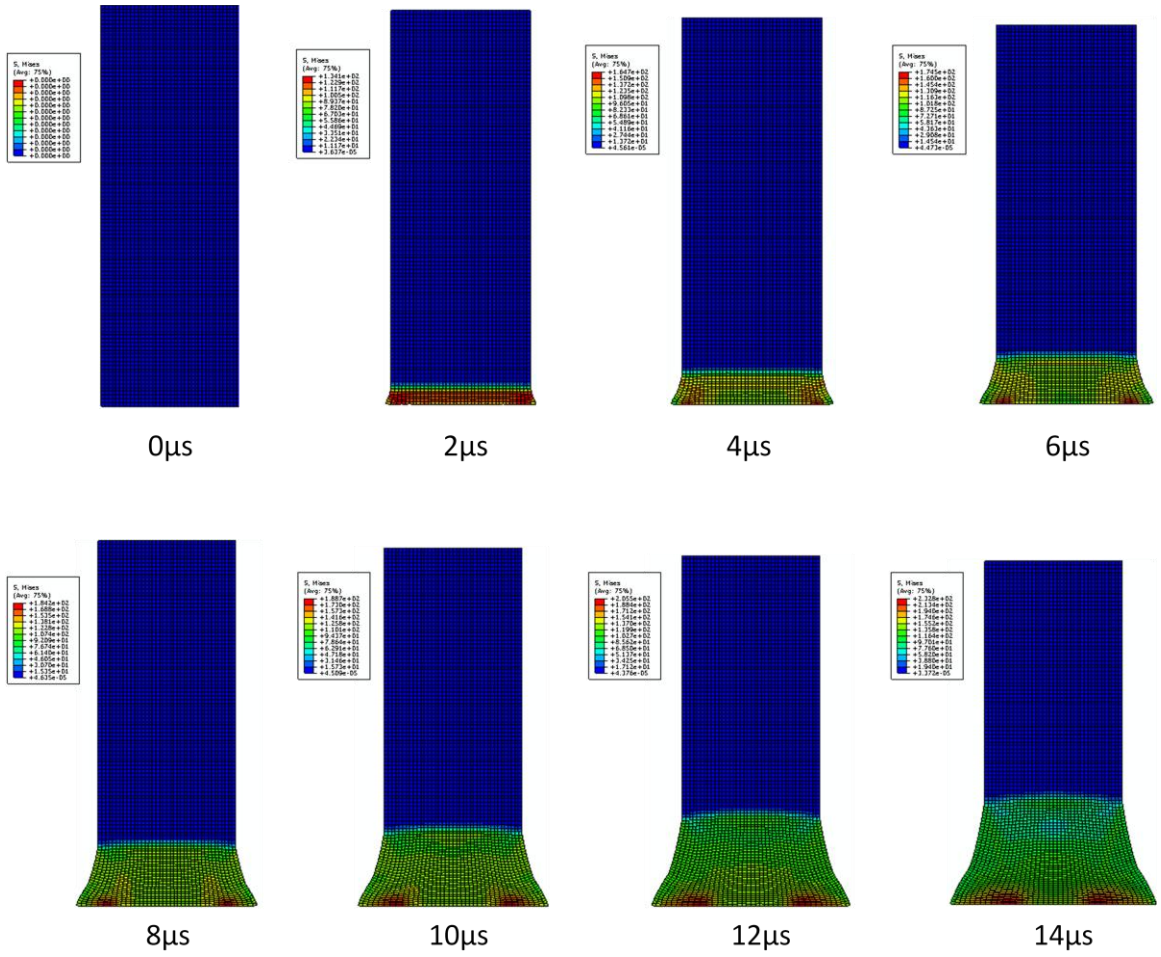

Figure 5.9. Simulation results of the Taylor impact test at V_i = 201.01 m/s (Batch #2)

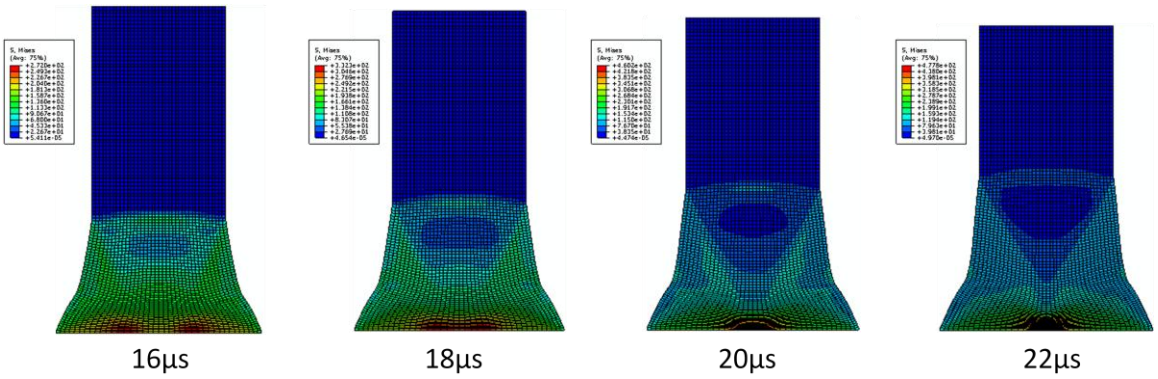

Figure 5.9. Continued

Stress contours in Figure 5.9 demonstrated the maximum internal stresses in the sample ranging from 134 to 478 MPa from 2 to 22 µs with its position moving from the circumference of the front impact surface to the central area of the front impact surface.

Figures 5.10 - 5.12 compare the simulation results with experimental images by measuring sample radius at certain axial intervals in *Photoshop* at 6 µs, 10 µs and 18 µs:

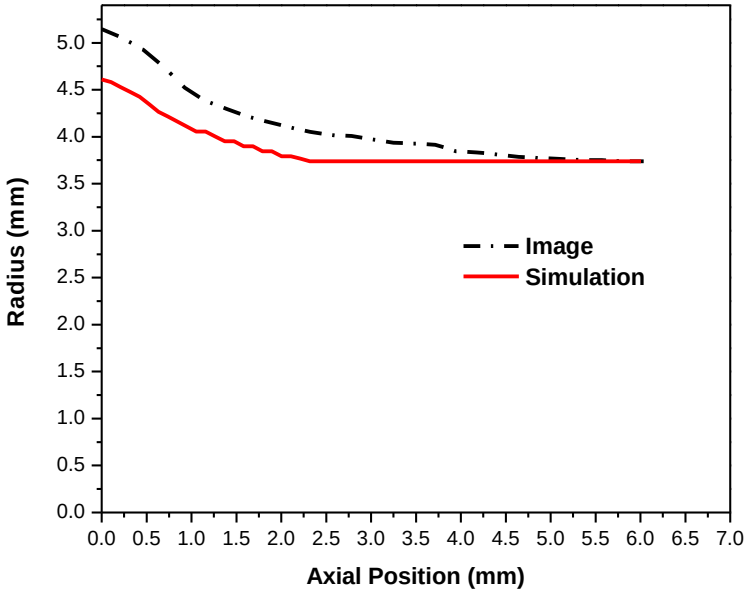

Figure 5.10. Comparison plots of radius *vs.* axial position between the experimental image and simulation results at 6 μs, V_i = 201.01 m/s

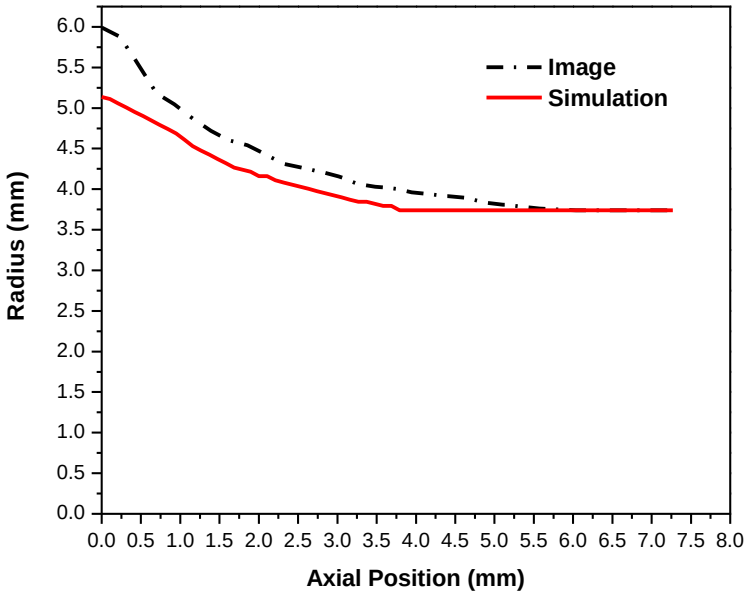

Figure 5.11. Comparison plots of radius *vs.* axial position between the experimental image and simulation results at 10 μs, V_i = 201.01 m/s

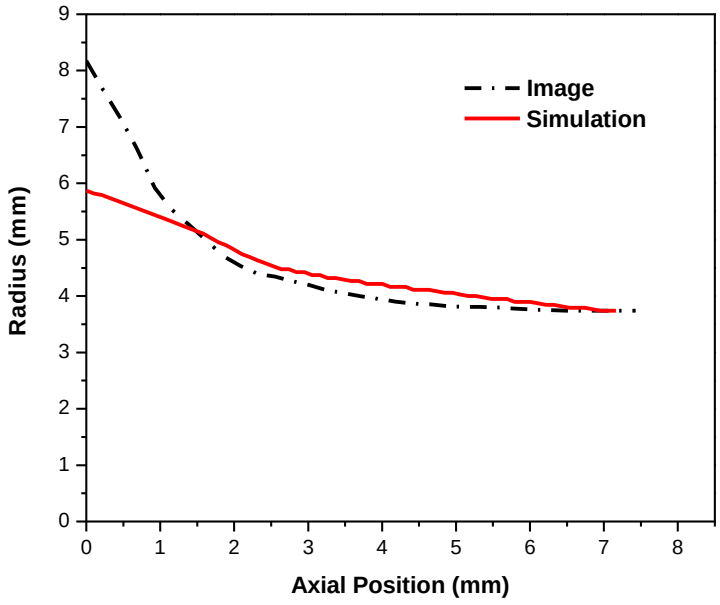

Figure 5.12. Comparison plots of radius *vs.* axial position between the experimental image and simulation results at 18 μs, V_i = 201.01 m/s

At 6 μs, the simulation radius profile overall was undersized compared to the experimental radius profile, and the maximum difference between them at the front impact surface was about 10%. At 10 μs, the simulation profile was still smaller than the experimental profile but with reasonable agreements in dimension, and the maximum radius difference at the front impact surface was around 12%. At 18 μs, the discrepancy increased dramatically, especially at the front impact segment where the maximum radius difference reached 29%. The simulation radius profile of the rear part did not show much difference with the experimental one, but a small bulge was still evident in the simulation results.

Figure 5.13 shows the stress contours of the large dimension sample's cross-section at each impact stage with the time interval of 2 μs at the impact velocity of 282.56 m/s:

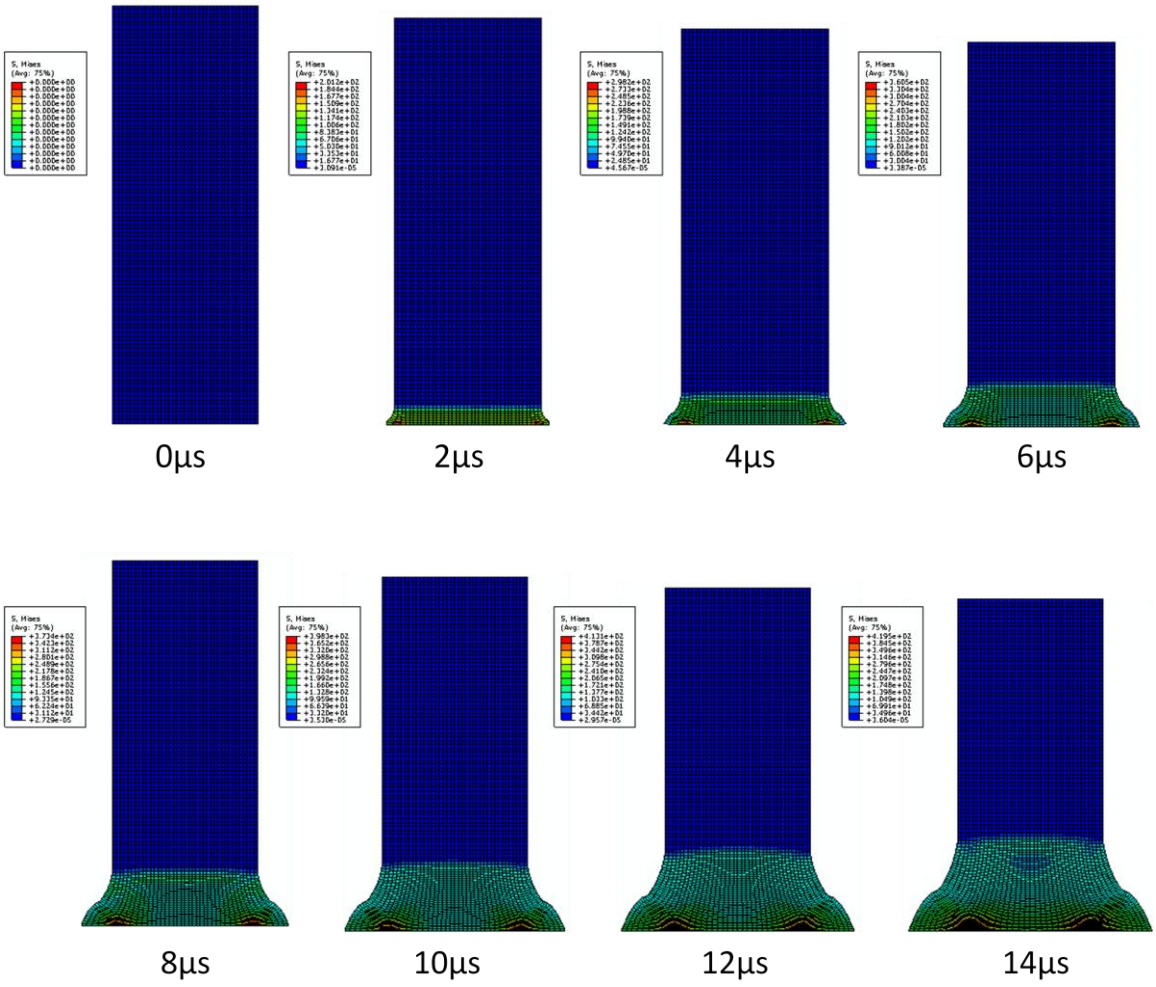

Figure 5.13. Simulation results of the Taylor impact test at V_i = 282.56 m/s (Batch #2)

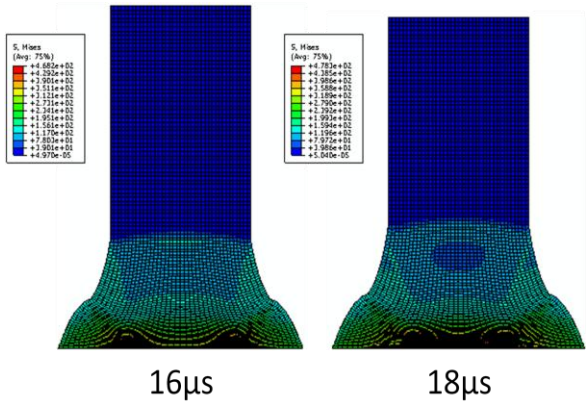

Figure 5.13. Continued

The maximum internal stresses in the sample varied from 201 to 478 MPa from 2 to 18 µs, and its position also moved from the circumference of the front impact surface to the central area of the front impact surface like described before.

Figures 5.14 - 5.15 compare the simulation results with experimental images by measuring sample radii at certain axial intervals in *Photoshop* at 6 µs and 10 µs:

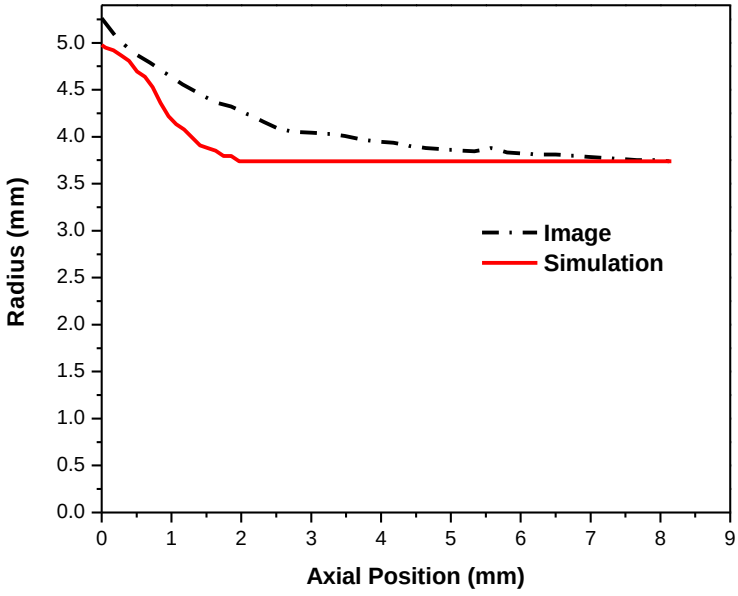

Figure 5.14. Comparison plots of radius *vs.* axial position between the experimental image and simulation results at 6 μs, V_i = 282.56 m/s

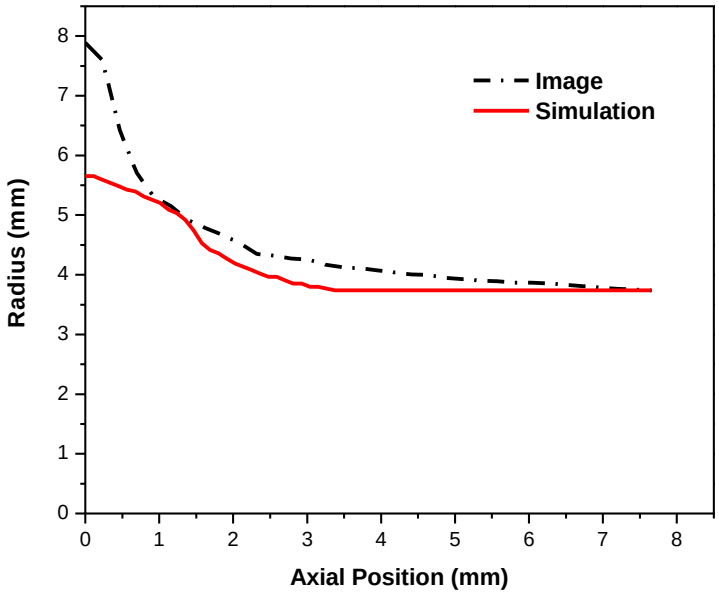

Figure 5.15. Comparison plots of radius *vs.* axial position between the experimental image and simulation results at 10 μs, V_i = 282.56 m/s

At 6 μs, the simulation radius profile was undersized compared with the experimental radius profile, but the maximum difference between them took place at the root area where radius changed abruptly. The maximum radius difference at the critical point was about 12%, beyond which the simulation radius profile changed little. At 10 μs the radius difference enlarged further, and the maximum difference at the front impact surface reached as much as 29%. Unlike the previous simulation results, bulge did not appear in the rear part of the sample.

Figure 5.16 shows the stress contours of the large dimension sample's cross-section at each impact stage with the time interval of 2.5 μs at the impact velocity of 406.44 m/s:

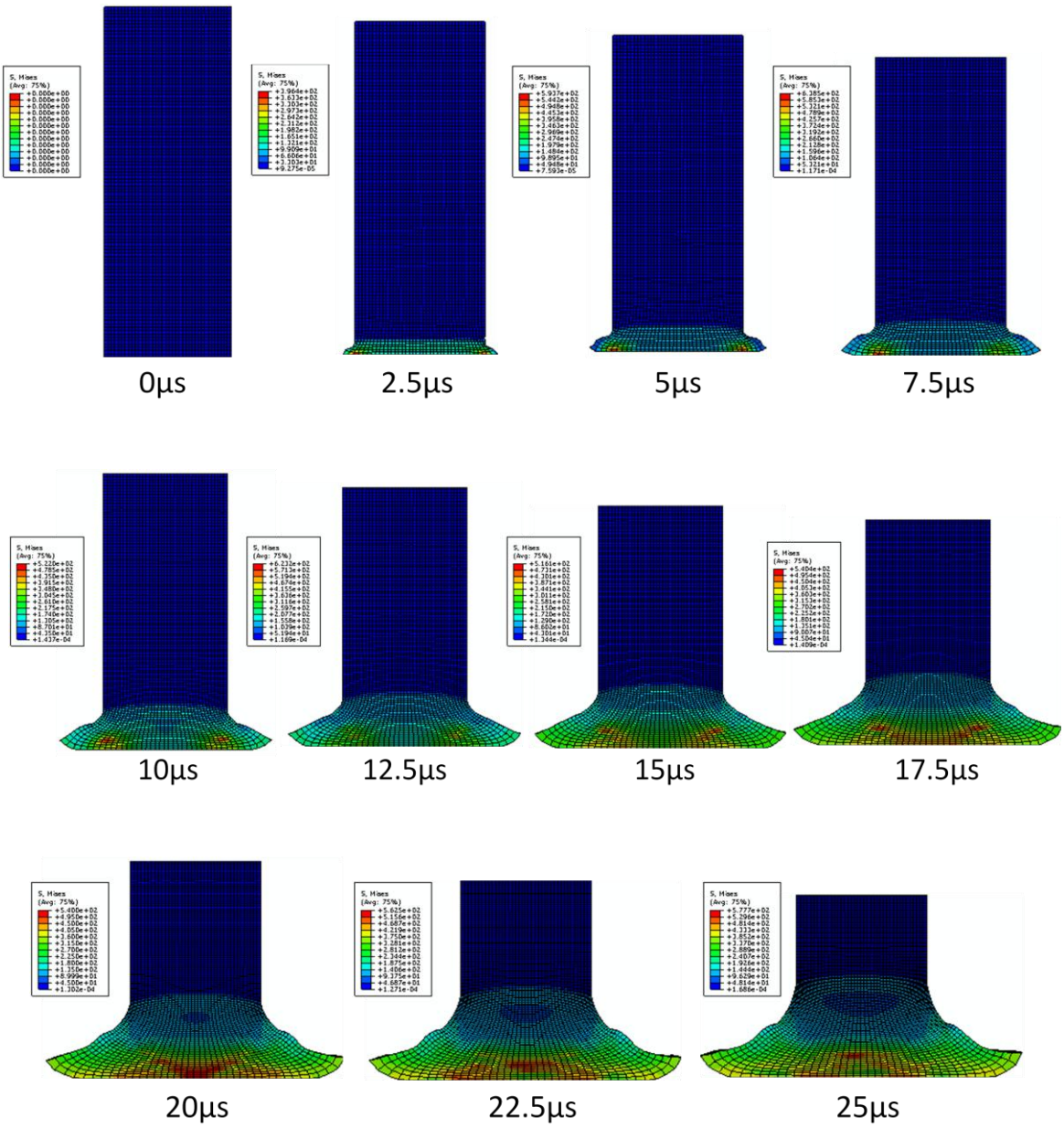

Figure 5.16. Simulation results of the Taylor impact test at V_i = 406.44 m/s (Batch #2)

The maximum internal stresses in the sample increased from 396 to 639 MPa during the period of 2.5 to 7.5 μs, it then vibrated around 550 MPa throughout the rest of the images.

Figures 5.17 - 5.19 compare the simulation results with experimental images by measuring sample radius at certain axial intervals in *Photoshop* at 2.5 μs, 5 μs and 7.5 μs:

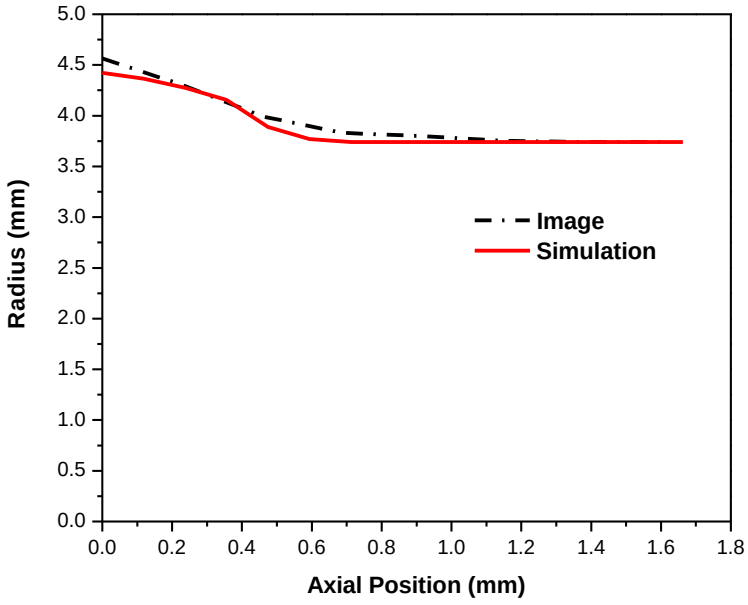

Figure 5.17. Comparison plots of radius *vs.* axial position between the experimental image and simulation results at 2.5 μs, V_i = 406.44 m/s

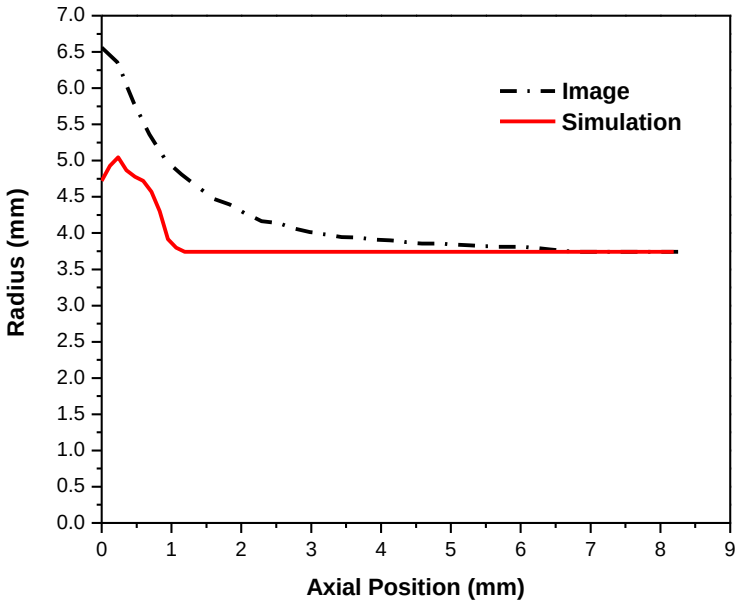

Figure 5.18. Comparison plots of radius *vs.* axial position between the experimental image and simulation results at 5 μs, V_i = 406.44 m/s

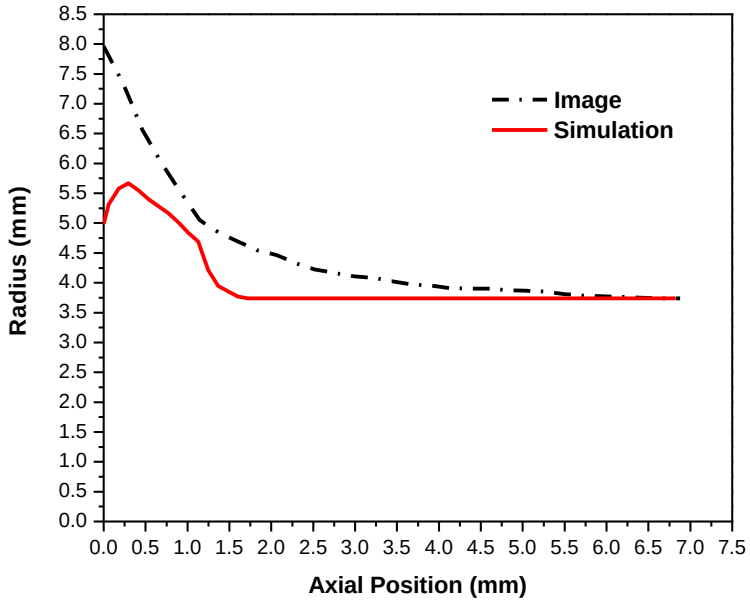

Figure 5.19. Comparison plots of radius *vs.* axial position between the experimental image and simulation results at 7.5 μs, V_i = 406.44 m/s

At 2.5 μs, the simulation radius profile well fit the experimental results, and the maximum radius difference at the front impact surface was less than 3%. At 5 μs and 7.5 μs, the disagreements became so evident that simulation results no longer properly reflected the deformation behavior of the sample, especially at the front impact area.

5.2.2 Discussions

Based on the simulation results and comparisons between simulation radius profile and image radius profile, the observations on the simulation output were: (1) in the impact velocity range from ~ 100 to ~ 400 m/s, the maximum internal stresses inside the sample increased from 152 to 639 MPa, and the location of the maximum stress in each frame at one impact velocity moved from the circumference of the front impact surface to

the central area of the front impact surface; (2) as the impact velocity increased, the deformation behavior at the front impact area became more and more intense so that the radical deformation exhibited a mushroom shape at the impact velocity of 282.56 m/s and 406.44 m/s; (3) comparing the simulation radius profiles with image radius profiles taken during Taylor impact test, reasonable agreements were found at the early stage of impact deformation for low impact velocities by taking into account of the pixel observation error in image measurement, i.e., at 112.38 m/s until 15 μs and 201.01 m/s until 10 μs. At later stages, differences between those profiles became evident, especially at the front impact surface, and a small bulge appeared in the rear part of the simulation radius profile. For high impact velocities, i.e., 282.56 m/s and 406.44 m/s, differences were observed even at the early stages, and the simulation results only described the deformation behavior during very short impact time, i.e., 6 μs at 282.56 m/s and 2.5 μs at 406.22 m/s; and (4) the failure of the modified Johnson-Cook constitutive model in describing the dynamic deformation behavior for the PTFE 7A / Ti composite at high impact velocities and late stages at low impact velocities could be attributed to several possibilities disregarding the intrinsic defects in the constitutive model, (e.g., no fracture criteria assigned to predict the crack formation for the PTFE 7A / Ti composite): (a) A solid-to-solid phase transition in the PTFE 7A component; (b) Change in internal porosity between particles; and (c) Possible light chemical reaction between PTFE 7A and Ti components.

5.3 Summary

A modified Johonson-Cook constitutive model was developed for the PTFE 7A / Ti composite by fitting with the stress *vs.* strain data points obtained from the Instron and SHPB tests at two different strain rates. The built constitutive model was then incorporated into *Abaqus* software for simulating the Taylor impact test process for large dimension samples at different impact velocities. By comparing the simulation results with images taken during Taylor impact test, it was found that: (1) the modified Johnson-Cook model was able to reasonably describe the deformation behavior of the PTFE 7A / Ti composite at the early stage of low impact velocities; (2) the modified Johnson-Cook model failed to depict the dynamic deformation process of the composite at high impact velocities and at the late stage of low impact velocities. Several possible reasons to explain the fact could be ascribed to: (1) a solid-to-solid phase transition in the PTFE 7A component; (2) changes in the internal porosity between particles; (3) possible light chemical reaction between PTFE 7A and Ti components.

CHAPTER VI

MICROSTRUCTURAL COMPUTATIONAL ANALYSIS OF THE EFFECT OF CONFIGURATION ON PTFE 7A / TI IMPACT-INITIATED REACTION

6.1 Overview

The transient images obtained from the Taylor impact test on medium dimension samples for the three batches of composites provided clear evidence of the effect of sample configuration on the reactivity of impact-initiated chemical reaction between the PTFE 7A and Ti components. The numerical simulation of microstructural deformation inside the composites during high-speed loading offered insights into understanding the mechanism of particle deformation, mixing and ultimately, reaction initiation.

In this chapter, real SEM images of the PTFE 7A / Ti composites from three batches were imported into *Abaqus* software to perform Taylor impact test simulation by attaching the composite with miscrostructural patterns onto the copper projectile under the same impact velocity. The approach for image conversion will also be discussed.

6.2 Approach

Importing SEM images into *Abaqus* followed the four-step procedures generalized below:

1. Converted SEM images into binary images by *Photoshop* software: first changed the RGB images to grey-scale images in *Photoshop*; used the "color range" function in "option" menu to separate PTFE 7A and Ti phases by choosing one component color and selecting appropriate color tolerance; then set the Ti component as white and the PTFE 7A component as black to make them binary images. Some parts of the image required manual threshold to separate the two phases.

2. Constructed vectorized images by *Adobe Illustrator* software: used the "live trace" function in "object" menu to delineate particle boundaries and save as vecortized images in *.dxf format.

3. Converted vectorized images as *.iges format: identified by *Abaqus* in *Rhinoceros* software.

4. Imported *.iges images in *Abaqus* for simulation setup.

The original SEM images, binary images, and vectorized images of the three composite batches are exhibited in Figure 6.1:

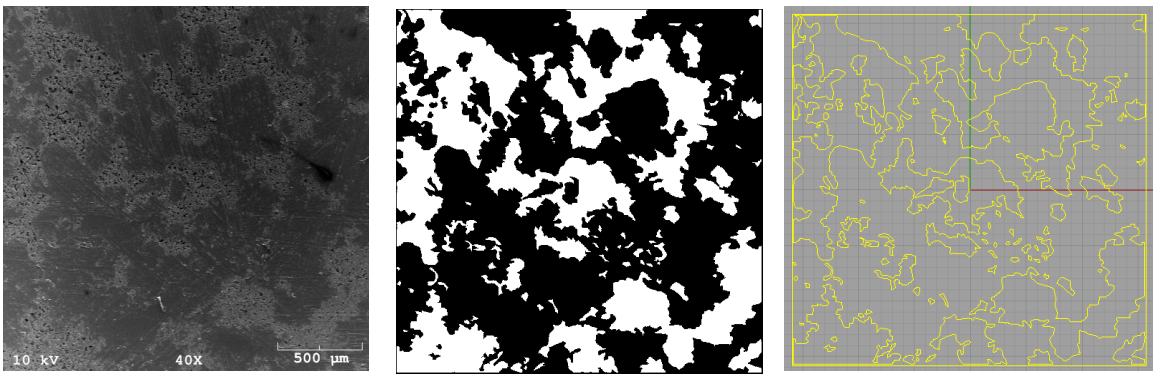

(a)

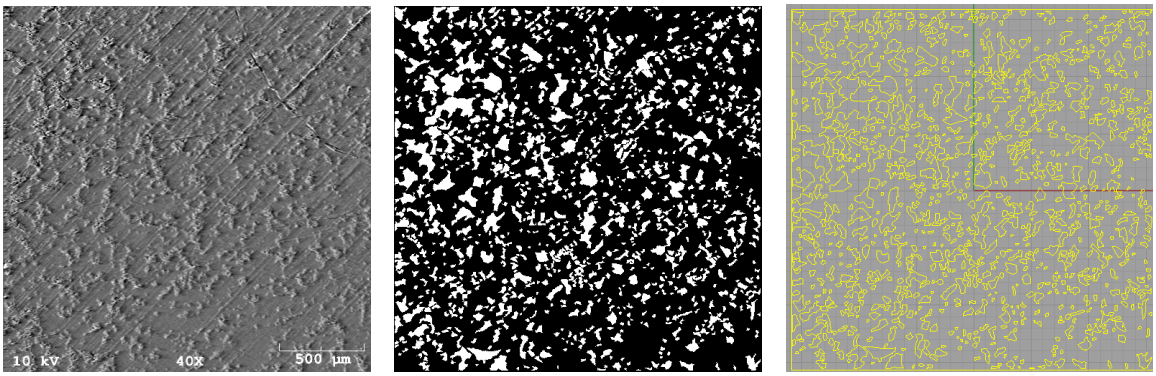

(b)

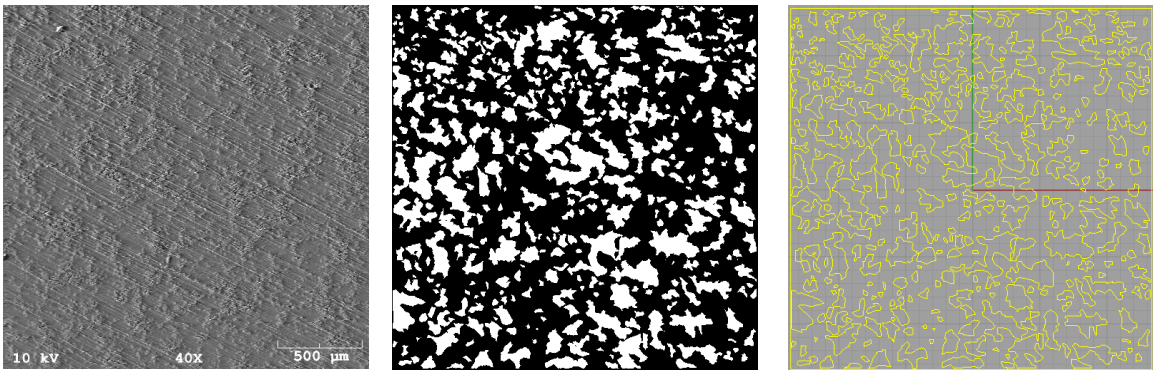

(c)

Figure 6.1. SEM image, binary image and vectorized image (from left to right in each line) of (a) Batch #1, (b) Batch #2, and (c) Batch #3

6.3 Constitutive Models and Input Parameters

The input material parameters for PTFE 7A are listed in Table 6.1:

Table 6.1. Input material parameters for PTFE 7A

Density (t/mm^3)	Young's modulus (MPa)	Poisson's ratio	Expansion coefficient (1/℃)	Specific heat (mJ/t ·℃)	Inelastic heat fraction
2.2×10^{-9}	516	0.4	1.6×10^{-5}	1.0×10^{9}	0.5

Figure 6.2 shows the stress *vs.* strain curves at different strain rate for PTFE at room temperature copied from the data points in the literature study by adopting the Zerilli-Armstrong model [73]:

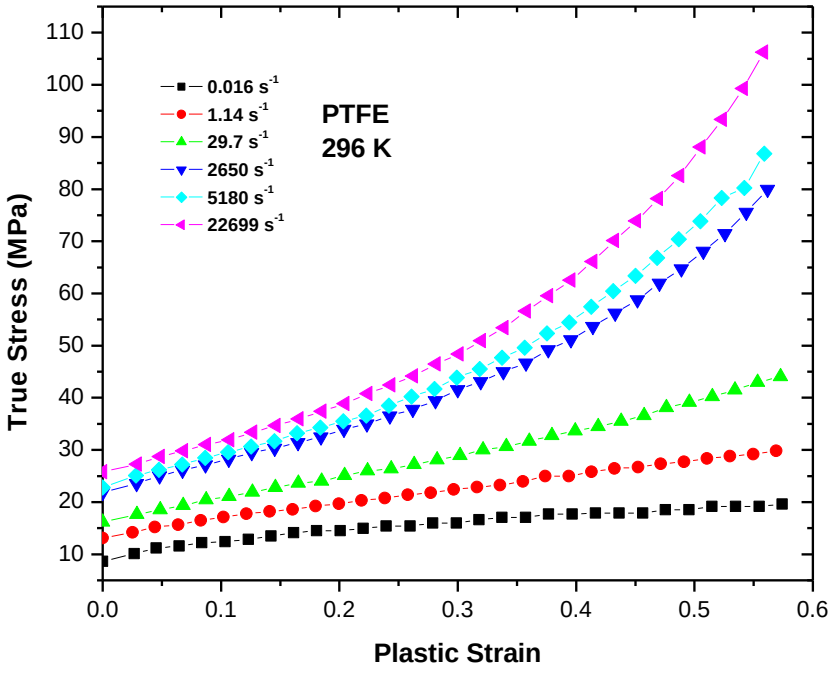

Figure 6.2. Stress vs. strain plots at various strain rates for PTFE material at 296 K [73]

The stress-strain-strain rate data sheet was then incorporated into *Abaqus* for material properties input.

The input material parameters for Ti are listed in Table 6.2:

Table 6.2. Input material parameters for Ti

Density (t/mm^3)	Young's modulus (MPa)	Poisson's ratio	Expansion coefficient (1/℃)	Specific heat (mJ/t ·℃)	Inelastic heat fraction
4.51×10^{-9}	116000	0.32	9.7×10^{-6}	5.15×10^{8}	0.9

The constitutive relation for Ti was referred to the study by Holt et al., in which the Zerilli-Armstrong model was applied with the consideration of the twinning effect of Ti [52]. Figure 6.3 plots the stress-strain-strain rate plane for the Ti material:

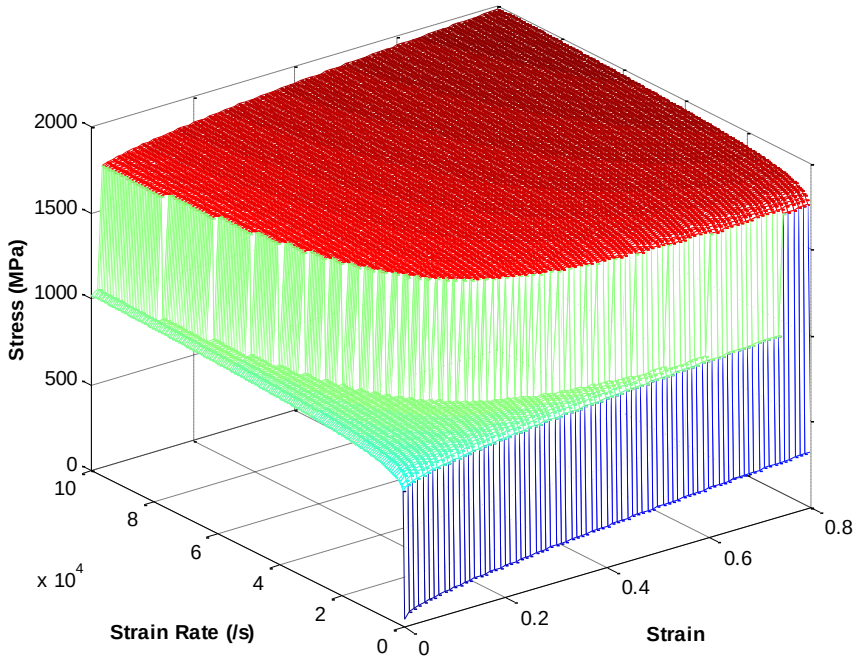

Figure 6.3. The stress-strain-strain rate plan for the Ti material with twinning effect at 296 K

The input material parameters for Copper are listed in Table 6.3, and the material constants of the Johnson-Cook constitutive model for Copper are shown in Table 6.4 [70]:

Table 6.3. Input material parameters for the Copper projectile

Density (t/mm^3)	Young's modulus (MPa)	Poisson's ratio	Expansion coefficient (1/℃)	Specific heat (mJ/t ·℃)	Inelastic heat fraction
8.94×10^{-9}	124000	0.34	5×10^{-5}	3.83×10^{8}	0.9

Table 6.4. Material constants of Johnson-Cook constitutive model for the Copper projectile [70]

A (MPa)	B (MPa)	n	m	C	$\dot{\varepsilon}$ (s^{-1})	Melting temperature (K)	Transition Temperature (K)
90	292	0.31	1.09	0.025	1	1356	298

6.4 Results and Analysis

The procedures of two dimensional microstructural simulation were similar to those described in Appendix B.2 except for defining all the interactions between PTFE 7A and Ti particle surfaces, which were discussed in detail in Appendix C. As for the simulation setup, microstructural images of similar sizes from three batches were directly attached onto the copper rod with the same impact velocity of 200 m/s. The model dimension and setup information is provided in Table 6.5:

Table 6.5. Model setups for the PTFE 7A / Ti microstructrual simulation

Simulation Setup / Batch #	Microstructural image width (mm)	Microstructural image length (mm)	Projectile width (mm)	Projectile Length (mm)	Anvil width (mm)	Impact velocity (m/s)
1	31.62	31.62	39.1	37.77	200	200
2	31.48	31.48	39.1	37.77	200	200
3	26.94	26.94	39.1	37.77	200	200

The length of the copper projectile was set at a quarter of its original length to save the simulation memory, so the corresponding density was four times that of the original.

6.4.1 Simulation Results of Batch #1 Samples

Figure 6.4 shows the simulation results of the deformation process of Batch #1 composite samples from 0 to 45 μs with a time interval of 9 μs. The microstructural deformation image and stress contour image are presented at each time frame.

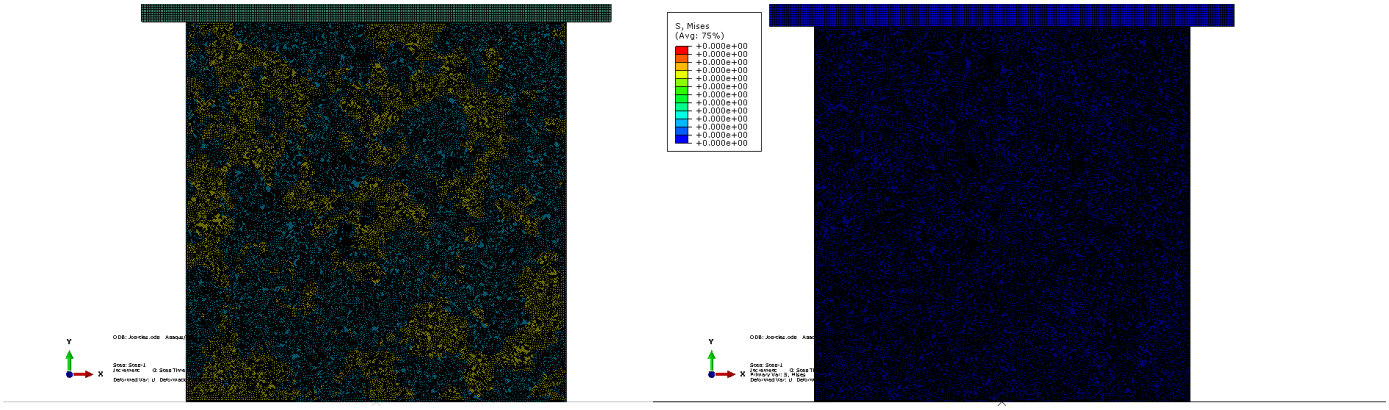

Figure 6.4. Microstructural simulation results of the Taylor impact test at V_i = 200 m/s (Batch #1). Left side: deformed shape; right side: deformed contour plots

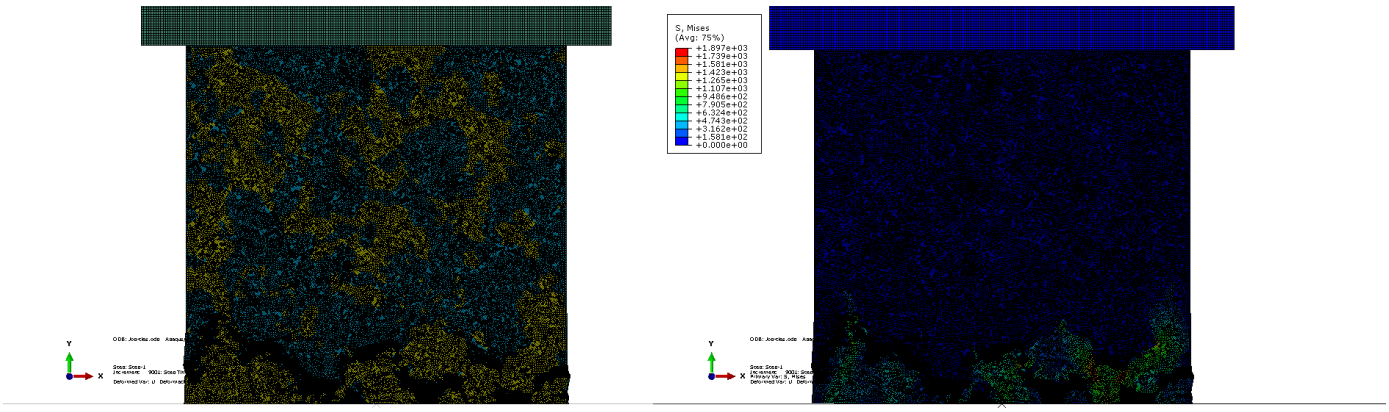

9 μs

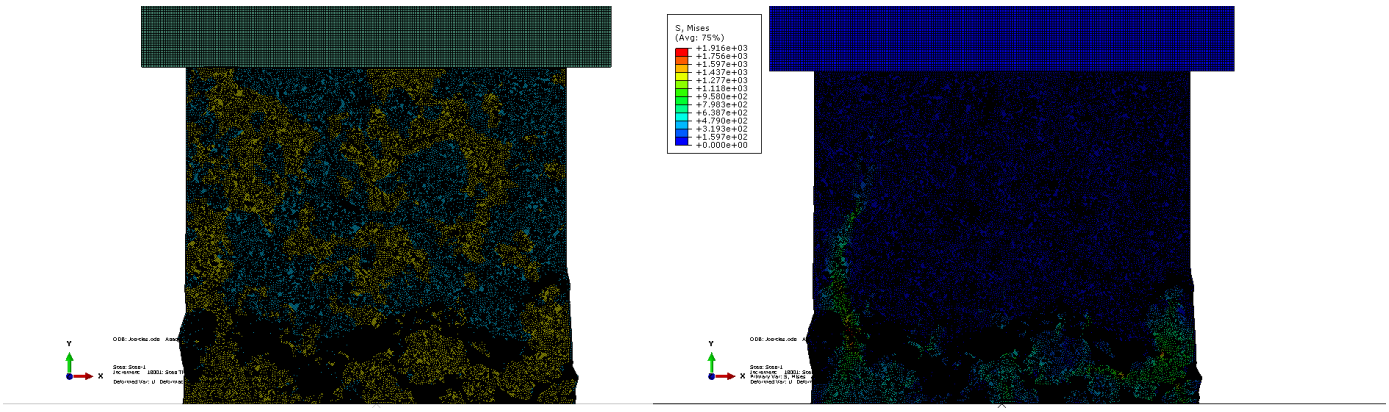

18 μs

Figure 6.4. Continued

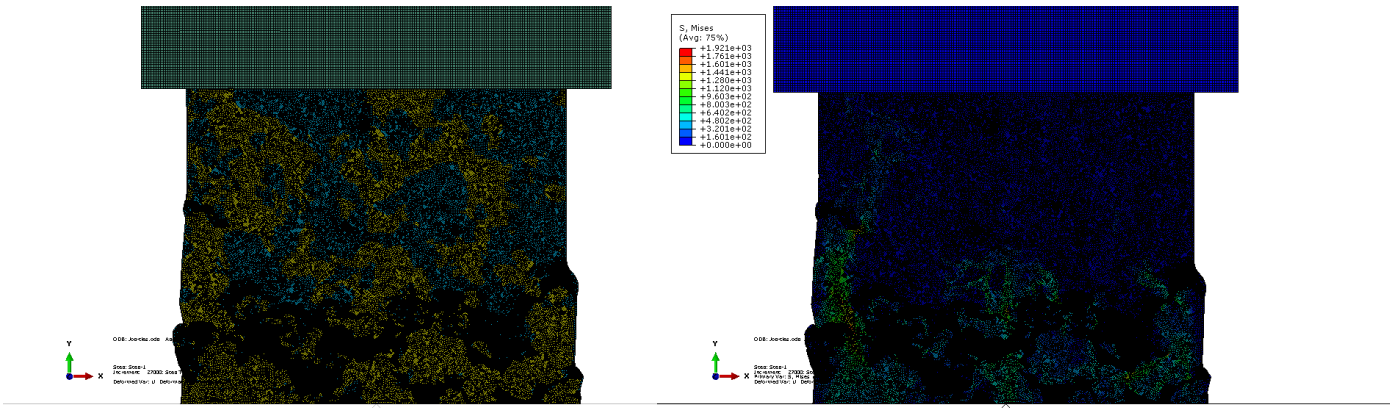

27 μs

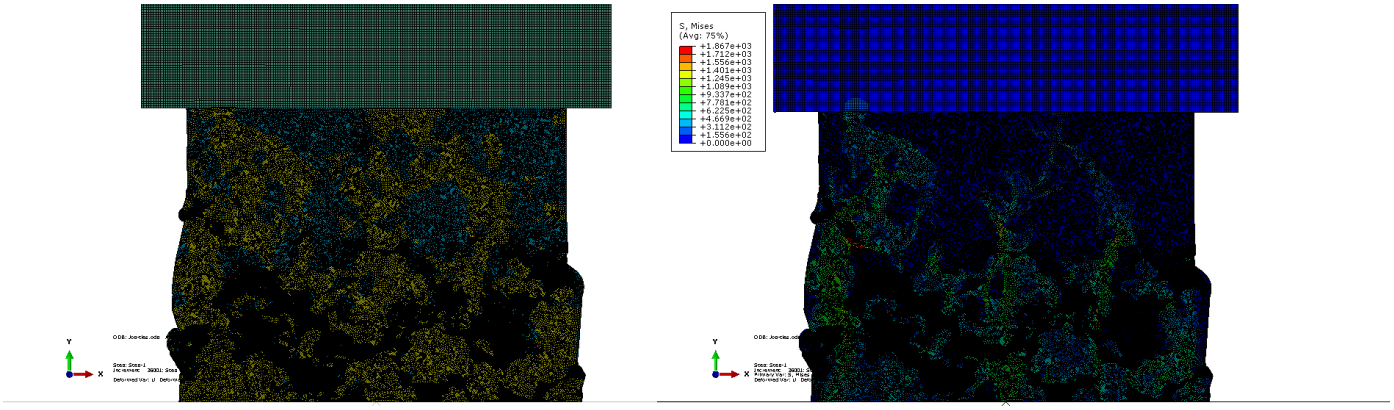

36 μs

Figure 6.4. Continued

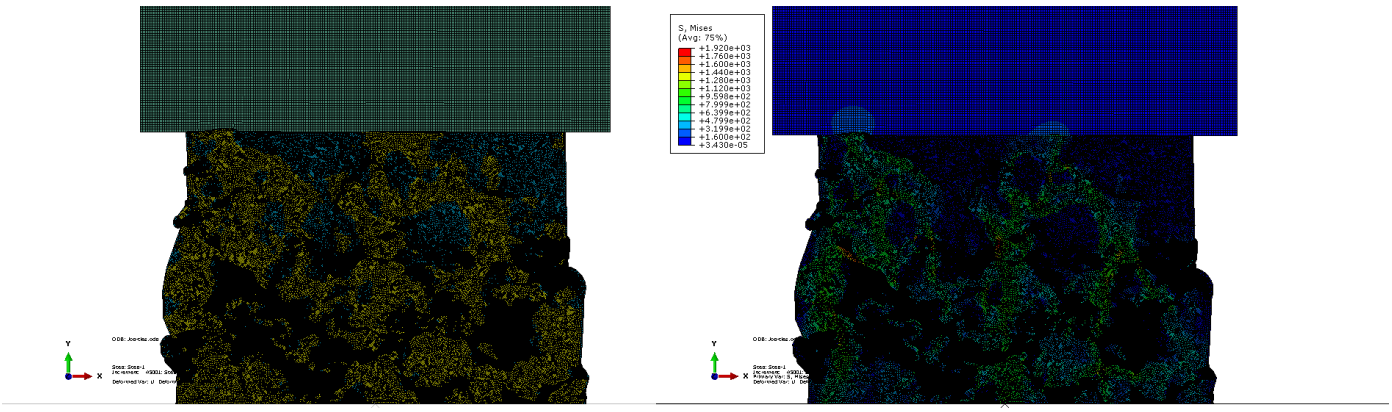

45 μs

Figure 6.4. Continued

The yellow region in the deformation images referred to Ti particles, while the blue region refers to PTFE 7A particles. By looking at the deformation behaviors in the composite structure, PTFE 7A regions were compressed intensely into the surrounding of hard Ti regions, which only exhibited limited deformation, so the overall composite showed irregular deformation behavior as impact went on. Contour images indicated the average Von Mises stress in each element. Compared with Ti particles, the stress variation in PTFE 7A particles was not evident, since the pressure scale was much smaller in the "soft" region with large deformation than in the "hard" region with limited shape changes. For Ti regions, the isolated Ti particles had lower average stresses which were less than 800 MPa, yet the bulk Ti areas had larger average stresses around 1200 MPa and some reached 1900 MPa in the most stress concentrated regions as indicated in red. For PTFE 7A regions, the average stress varied from 50 to 100MPa in most of the deformed regions except for the free moving areas on two sides.

6.4.2 Simulation Results of Batch #2 Samples

Similarly, Figure 6.5 shows the simulation results of the deformation process on the Batch #2 composite samples from 0 to 45 μs with a time interval of 9 μs. The microstructural deformation image and stress contour image are presented at each time frame:

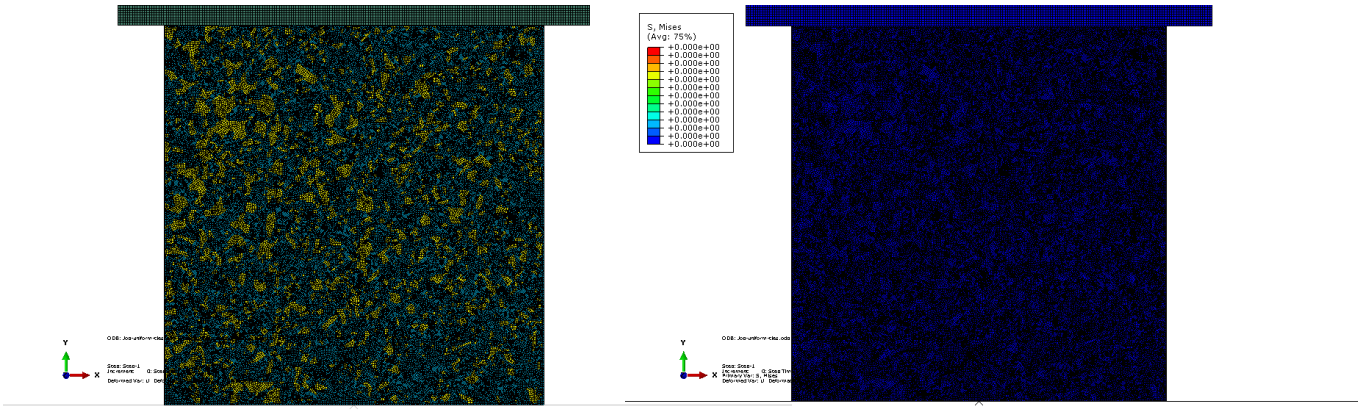

0 μs

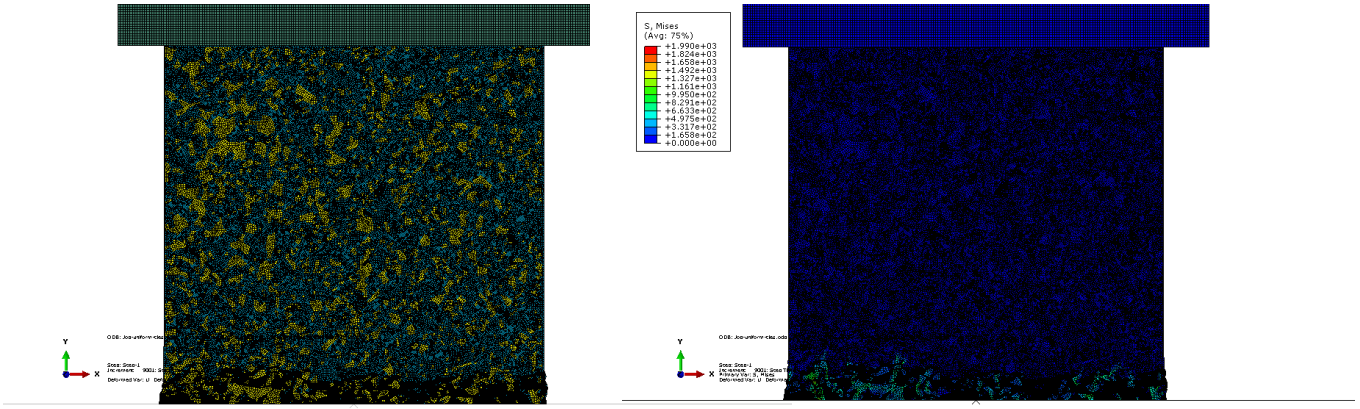

9 μs

Figure 6.5. Microstructural simulation results of the Taylor impact test at V_i = 200 m/s (Batch #2). Left side: deformed shape; right side: deformed contour plots

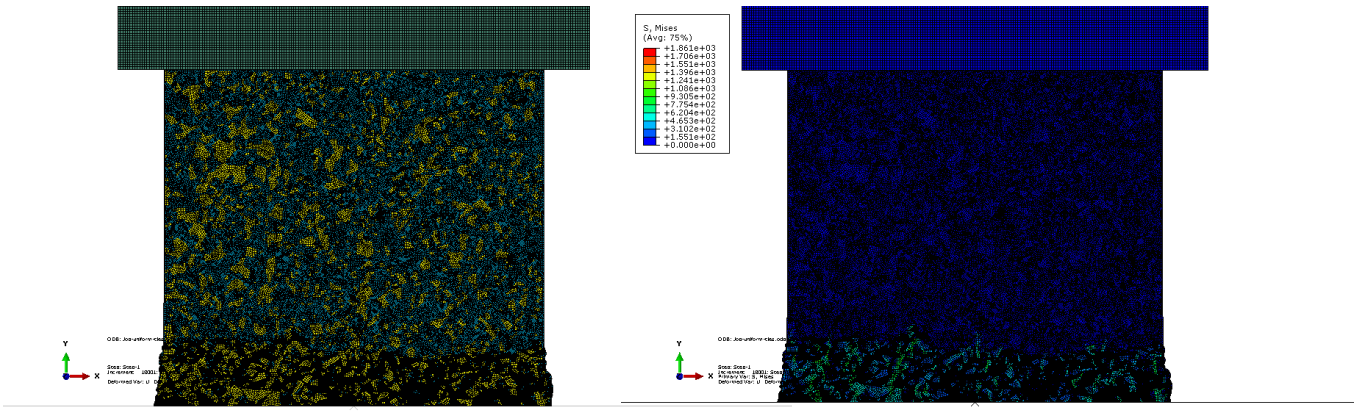

18 μs

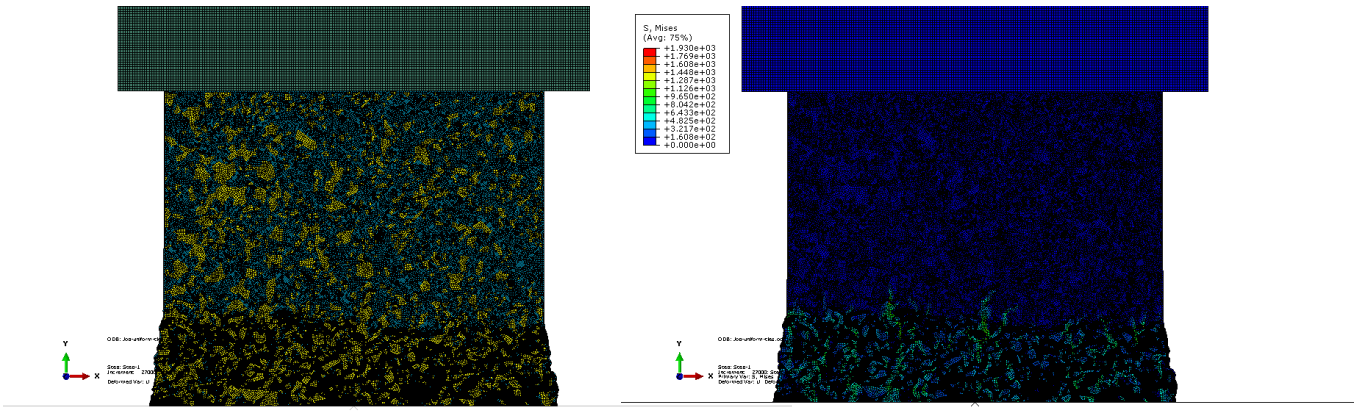

27 μs

Figure 6.5. Continued

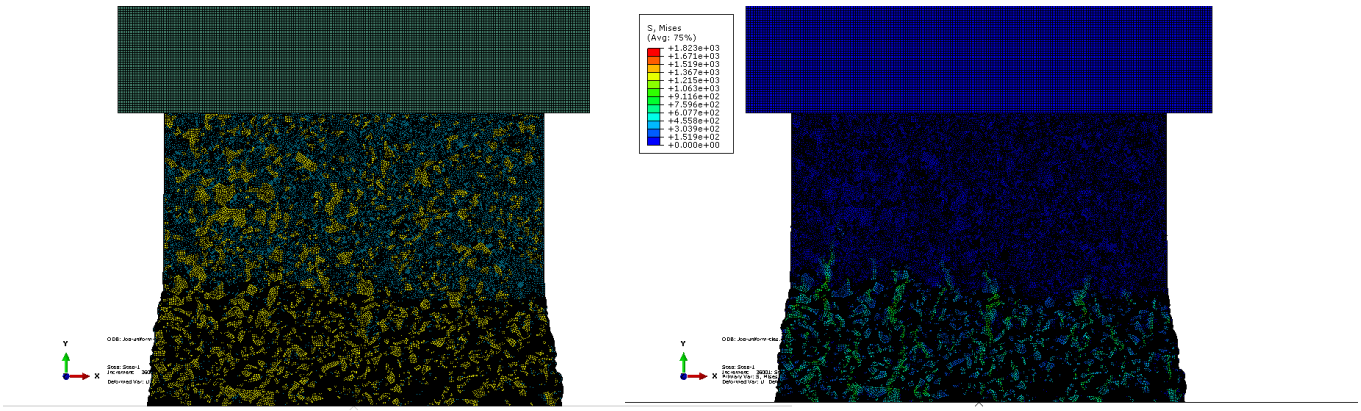

36 μs

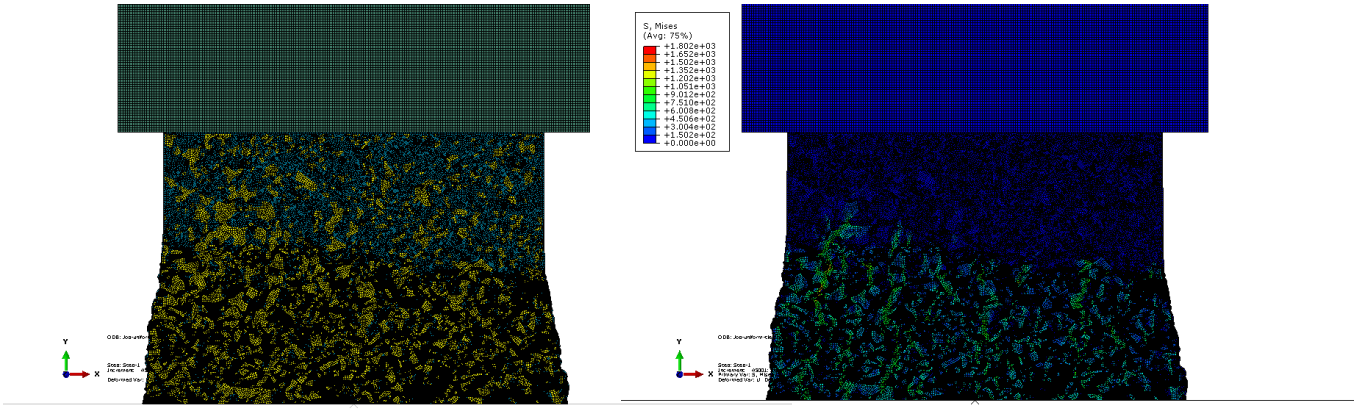

45 μs

Figure 6.5. Continued

Although with the same constitution as in Batch #1, the impact process of Batch #2 sample exhibited a quite uniform deformation behavior due to the even distribution of Ti particles in the PTFE 7A matrix. In this case, almost all of the Ti particles were isolated inside the PTFE 7A regions, and in very few examples did the Ti regions encompass the PTFE 7A areas. As for the stress value, the Ti regions had an average stress variation from 100 to 1200 MPa for most part, and the PTFE 7A regions had a similar stress variation as in Batch #1, which was in the range of 50 - 100 MPa.

6.4.3 Simulation Results of Batch #3 Samples

Figure 6.6 shows the simulation results of the deformation process on the Batch #3 composite samples from 0 to 45 μs with a time interval of 9 μs:

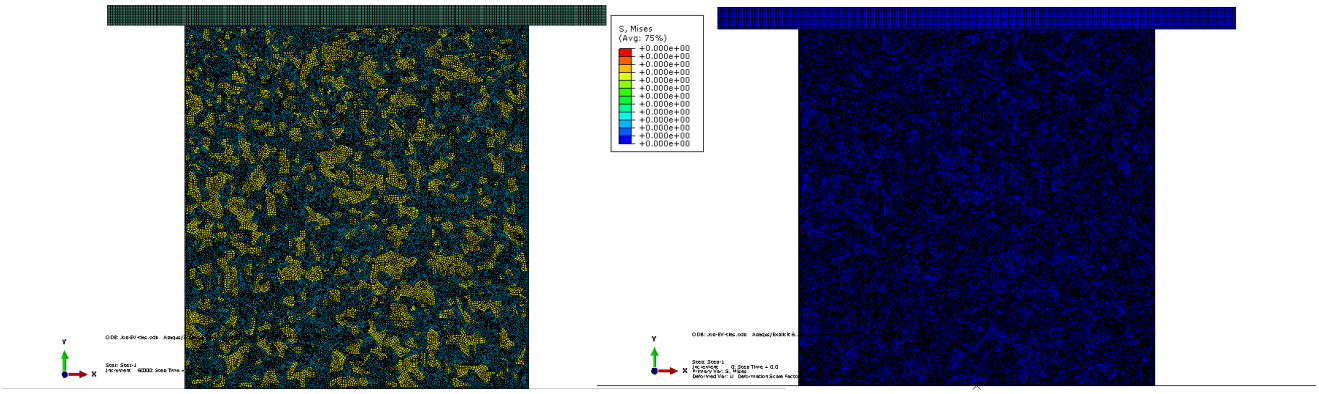

0 μs

Figure 6.6. Microstructural simulation results of the Taylor impact test at V_i = 200 m/s (Batch #3). Left side: deformed shape; right side: deformed contour plots

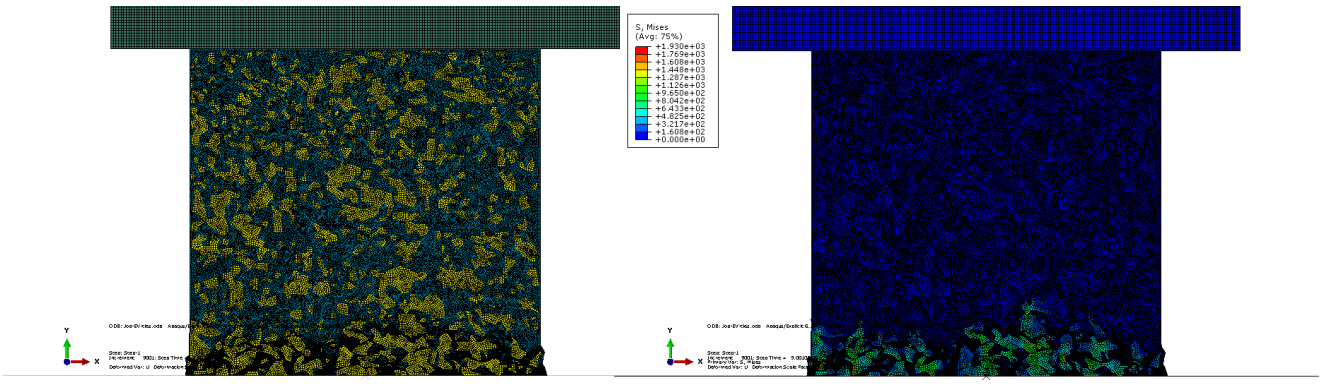

9 μs

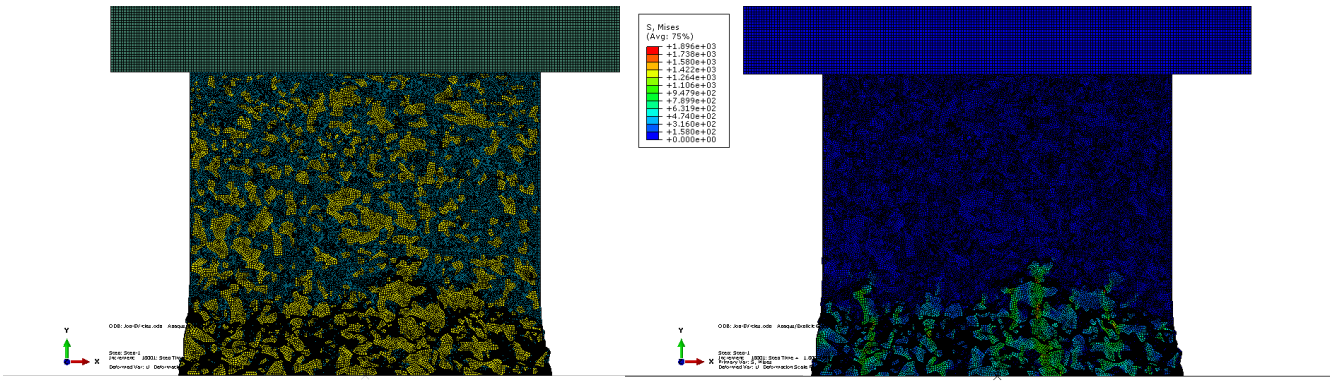

18 μs

Figure 6.6. Continued

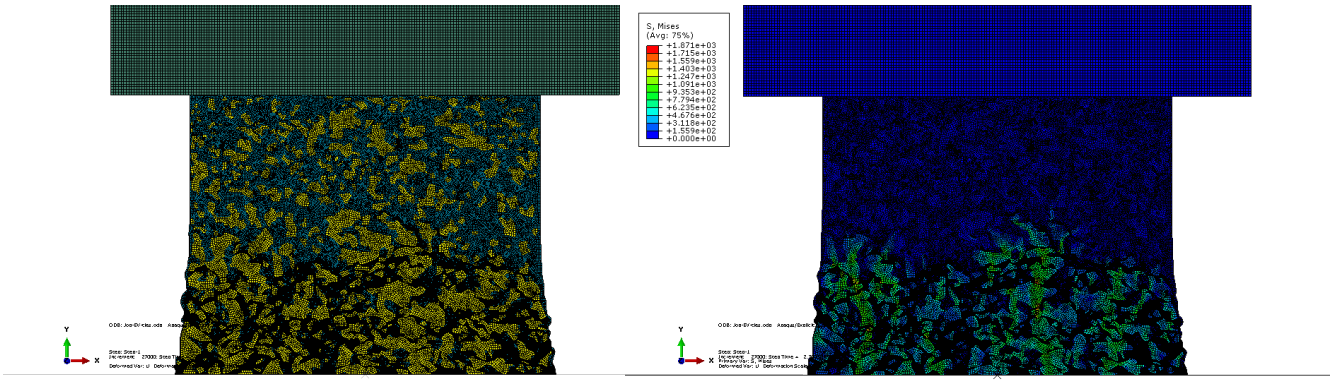

27 μs

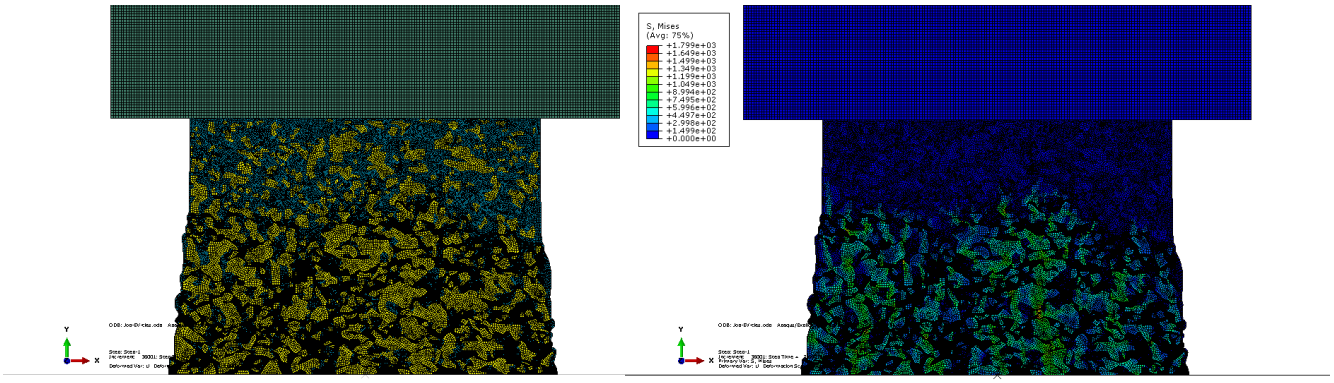

36 μs

Figure 6.6. Continued

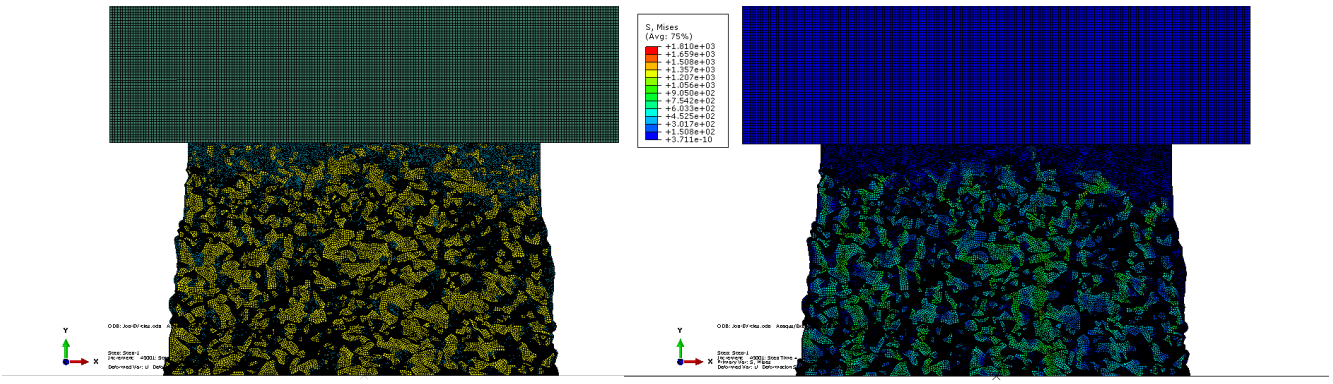

45 μs

Figure 6.6. Continued

Since the Batch #3 composite shared a similar configuration as batch #2 but with more Ti content (67.6 wt% in Batch #3 and 49 wt% in Batch #2), Batch #3 samples demonstrated a uniform deformation process but with less shape change compared to Batch #2 samples due to the stronger Ti reinforcement effect. Although Ti particles in this case were evenly isolated in the PTFE 7A matrix, some of the Ti enriched regions could still trap PTFE 7A particles inside as the impact process proceeded, similar to the phenomenon observed with Batch #1. The Ti regions had an average stress varying from 100 to 1300 MPa for the most part, and some of the stress-concentrated regions reached an average stress of 1900 MPa. The PTFE 7A regions had a similar stress variation as in Batch #1 and Batch #2, which was in the range of 50 to 100 MPa.

6.4.4 Discussions

Experimental results and analyses in Subsection 4.3.4.4 highlighted the differences in the impact-initiated reaction among three batches. The “hard encompassing soft”

structure was proposed for the order of the severity in reaction as Batch #1 > Batch #2 > Batch #3. Without considering the temperature involvement during miscrostructural impact simulation, the expected higher local stresses in the encompassed PTFE 7A regions were not observed. However, higher stresses appeared on several spots of the Ti enriched regions for the "hard encompassing soft" structure.

Since the dimension of the microstructural image of the Batch #3 component was smaller than the other two (Table 6.5), only the simulation results of stress contours from Batch #1 and Batch #2 were compared here at each time frame (Figure 6.7):

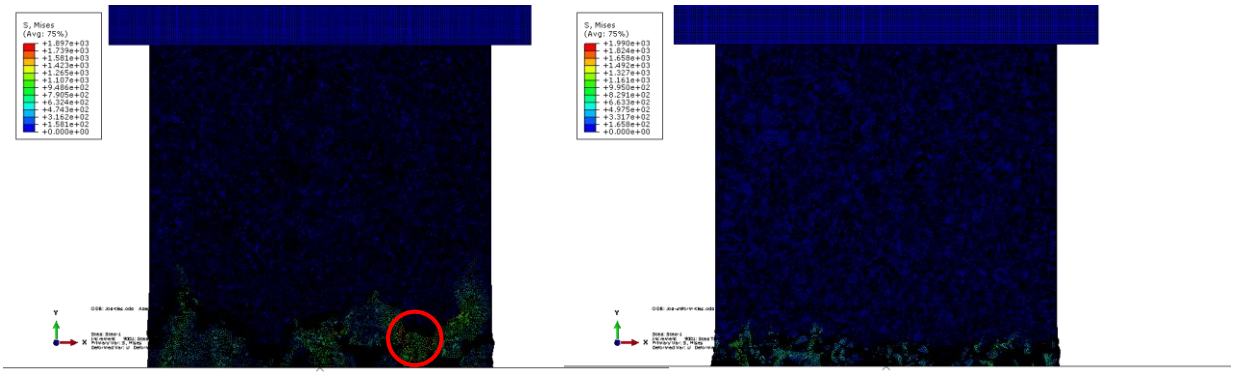

9 µs

Figure 6.7. Comparison of microstructural simulation results on Batch #1 (left) and Batch #2 (right)

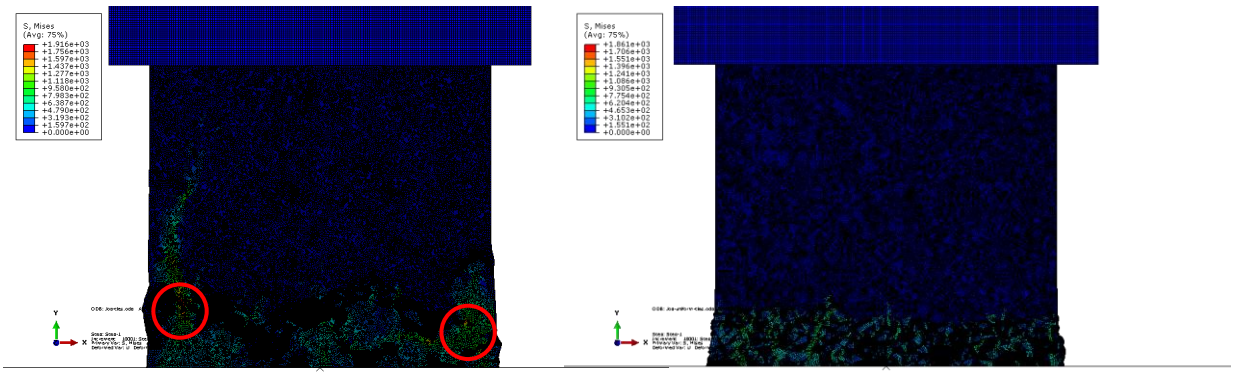

18 µs

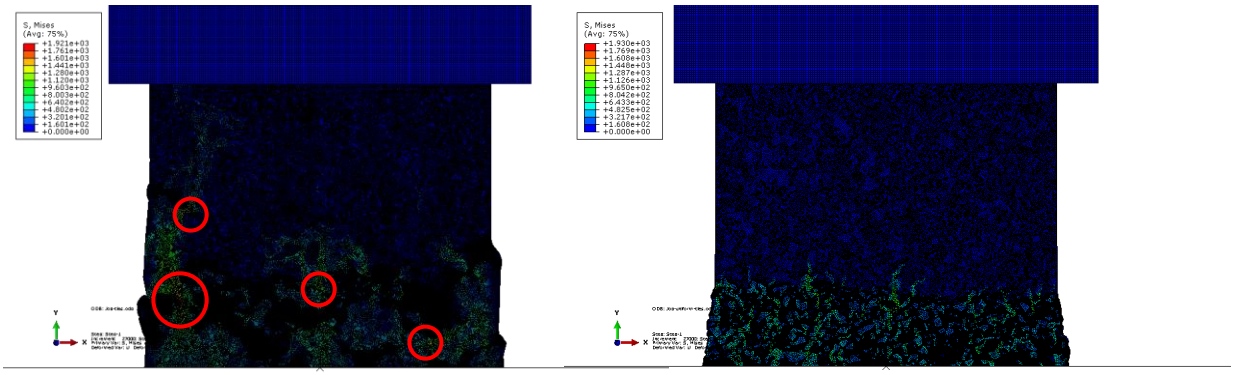

27 µs

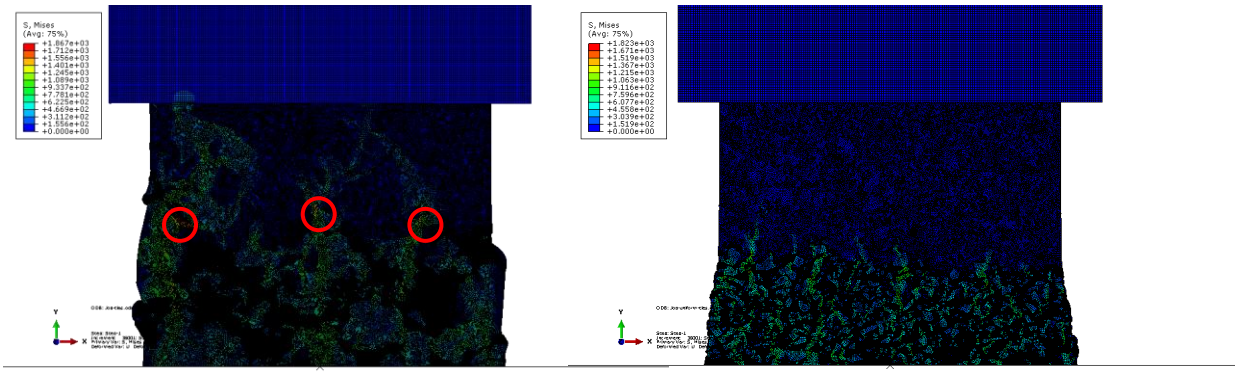

36 µs

Figure 6.7. Continued

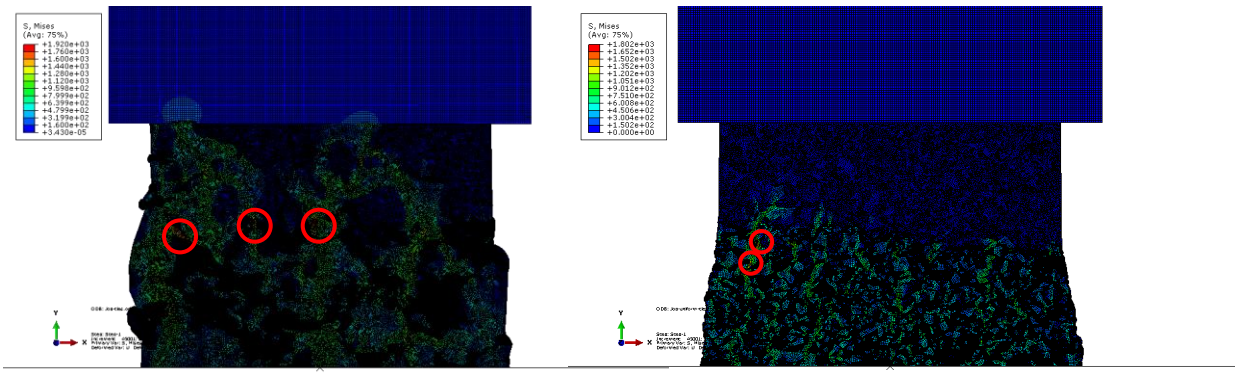

45 μs

Figure 6.7. Continued

Batch #1 and Batch #2 shared the same constitution, but with different configurations in the Ti distribution, so it was effective to compare the microstructural deformation in these two cases to study the influence of configuration on the impact-initiated reaction. Besides the differences in the evolvement of sample shapes, the Batch #1 sample had obviously higher local average stresses in certain stress concentrated regions in the Ti enriched areas (spots circled in red, Figure 6.7), where the highest local stress reaching 1900 MPa appeared from the beginning of the impact process. Compared with Batch #1, the Batch #2 sample exhibited a much more uniform distribution of the local stress in Ti regions, which was in the range of 100 to 1200 MPa. Until the very end of the simulation process, several spots in Ti regions showed high local stress around 1900 MPa for the Batch #2 sample. The large amount of Ti-aggregated regions in Batch #1 was accounted for the higher local stress in Ti areas since the hard component-aggregated region could undertake more compressive pressure than other parts, resulting in the stress concentration in certain spots. Even if the simulation results showed similar local stress

contours in PTFE 7A regions for both the Batch #1 and Batch #2 samples, the higher local stress in the Ti regions was also an important factor for triggering the impact-initiated reaction. Assuming the deformation in the PTFE 7A regions were comparable in these two batches, the diffusion path of the degradation products from PTFE 7A would be favorable in the areas with higher local stress like the ones circled in red in Figure 6.7, where the defects in the Ti crystal structure would provide vacancies for Carbon or other atoms flowing inside. Albeit the assumptions and simplifications applied during simulation, the detailed microstructural deformation behavior and stress contours provided a valuable insight into the internal evolvement between the two composite components, further leading to a possible impact-initiated reaction mechanism for polymer / reactive metal composite systems.

6.5 Summary

Microstructural Taylor impact simulations were conducted on Batch #1, Batch #2 and Batch #3 composite samples by importing real SEM images into *Abaqus* software. Simulation results revealed the internal deformation behaviors of the PTFE 7A and Ti components with detailed stress contours. Some of the stress concentrated regions in the Ti-aggregated areas in Batch #1 samples showed much higher average stresses at early stages of impact loading than the other two batches, while the PTFE 7A regions shared similar stress contours in all three batches. Although the expected higher local stresses in PTFE 7A regions with a "hard encompassing soft" structure was not observed, the

concentrated local stress in some of the Ti-aggregated regions provided a possible explanation for the favor of impact-initiated reaction in Batch #1 samples.

CHAPTER VII

CONCLUSIONS

7.1 Summary of Work

The chemical and mechanical properties of the PTFE 7A / Ti composite system were studied through high strain rates tests, thermal analyses and numerical simulations. The PTFE 7A / Ti composite with different constitutions and configurations were produced and tested under a wide range of impact velocities to determine the factors influencing the reactivity of the system: (1) PTFE 7A (51 wt%) / Ti (49 wt%) composite with non-uniform distribution; (2) PTFE 7A (51 wt%) / Ti (49 wt%) composite with uniform distribution; (3) PTFE 7A (32.4 wt%) / Ti (67.6 wt%) composite (equal volume composition) with uniform distribution.

The PTFE 7A / Ti composite systems were characterized through thermal analyses and mechanical tests at a wide range of strain rates by the Instron and SHPB tests:

- Thermal analyses of the composite by DTA and XRD analyses provided evidence that the reaction was between the elemental Ti powder and the products from PTFE 7A decomposition, with TiC_x one of the main reaction products.
- The *x* value in TiC_x increased dramatically to ~ 1 as the heating rate decreased, suggesting that a slow heating rate led to a more thorough reaction and a product with improved crystalline structure.

- Compared with the pure PTFE 7A sample, the yield stresses and Young's modulus of the PTFE 7A / Ti composites exhibited higher values due to the incorporation of Ti particles. The yield stress increased as the strain rate increased for both PTFE 7A and the PTFE 7A / Ti composite.
- Post-SHPB samples (both with PTFE 7A and the PTFE 7A / Ti composites) under different compression pressures were analyzed by XRD. For PTFE 7A, a new crystalline peak formed at around 28 ° as the compression pressure increased to 60 psi, which was assumed to be a strain-induced crystallization process. For the PTFE 7A / Ti composite, only a stronger PTFE 7A (110) crystalline peak was observed as the compression pressure increased, i.e., no other new crystalline peak was found in this system.

Taylor impact tests with impact velocities ranging from ~ 100 to 500 m/s were then applied on three batches of formed PTFE 7A / Ti composites with large, medium, small and even smaller dimensions to investigate the factors impacting the reactivity of the system:

- Either ignition light or fume, which are indicators of impact-initiated reaction, were observed for medium, small and even smaller dimension samples from all batches at certain impact velocity ranges. The impact-reactivity of the PTFE 7A / Ti composite systems was in the time scale of microseconds.
- The impact-initiated reactivity was dependent on both the impact velocity (kinetic energy) and the shear strain / stress value. Only when both the impact velocity (kinetic energy) and the shear component of strain / stress exceed certain threshold values did the impact-initiated reaction occur.

- Sample dimension had a remarkable effect on the ignition time and the severity of reaction. As the sample dimension was reduced, the ignition time decreased and the reaction severity increased.
- The impact-initiated reaction of the PTFE 7A / Ti composites preferred a Ti-aggregated structure. A "hard-encompassing-soft" structure resisted the particle deformation in regions, thus localizing the stress and temperature accumulation to accelerate the reaction.

A modified Johnson-Cook constitutive model was developed for the PTFE 7A / Ti composites by fitting with the stress *vs.* strain data plots obtained from the Instron and SHPB tests at two different strain rates. The built constitutive model was then incorporated into *Abaqus* software for simulating the Taylor impact test process for large dimension samples at different impact velocities:

- The modified Johnson-Cook model was able to reasonably describe the deformation behavior of PTFE 7A / Ti composite at the early stage of low impact velocities.
- The modified Johnson-Cook model failed to depict the dynamic deformation process of the composite at high impact velocities and at the late stages of low impact velocities, attributed to: (1) A solid-to-solid phase transition in the PTFE 7A component; (2) A change in internal porosity between particles; (3) A possible light-emitting chemical reaction between the PTFE 7A and Ti components.

Finally, microstructural simulations were conducted on the three PTFE 7A / Ti composite batches by importing real SEM images into the *Abaqus* software:

- Some of the stress concentrated regions in the Ti-aggregated areas in Batch #1 showed much higher average stresses at early stages of impact loading than the

other two batches, while the PTFE 7A regions shared similar stress contours in all three batches.

- Although the expected higher local stress in the PTFE 7A regions in a "hard-encompassing-soft" structure was not observed, the concentrated local stress in some of the Ti-aggregated regions provided a possible explanation for the preference of impact-initiated reaction in the Batch #1 samples.

7.2 Work Significance

The PTFE 7A / Ti composite systems studied by the Taylor impact test equipped with high speed camera provided the evidence of impact-initiated chemical reaction between the two components. Either reaction light or reaction fume was observed in images taken during impact processes in the time scale of tens of microseconds. The impact deformation analyses before chemical reaction taking place determined two important factors for triggering the impact-initiated reaction: impact velocity (kinetic energy) and the degree of deformation (shear strain / stress). Experimental results from three batches with different configurations indicated that an aggregation of the "hard" component - Ti encompassing "soft" component - PTFE 7A triggered a much severe chemical reaction compared to other configurations.

The constitutive model for PTFE 7A / Ti composite was developed based on the modified Johnson-Cook model by fitting it with stress *vs.* strain relations in a wide range of strain rates. Simulation results on Taylor impact test with comparison to the high speed images showed reasonable agreements at the early stages of low velocity impact.

Microstructural simulation by importing real SEM images provided an insight of the internal deformation behavior between two components and proposed that the diffusion path of the degradation products from PTFE 7A would be favorable in the areas with higher local stress, i.e. the Ti-aggregated regions to account for the higher reactivity of Ti-aggregated configuration structures.

All of the above fundamental results provided a thorough understanding of the chemical and mechanical behaviors of the PTFE 7A / Ti composite system under high strain rate loading. These results also provide further insight into understanding the reaction mechanism between the polymer and reactive metal component, ultimately leading to control of the reaction for potential applications.

7.3 Recommendations for Future Work

Since the post-shock products from the reactive Taylor impact test could not be recovered due to the severity of the combustion-like reaction, attempts should be made to collect the recovered materials, e.g., by mounting a transparent plastic tube between the entrance of the chamber and the impact surface of the anvil. The recovered material could then be characterized by XRD and SEM for identifying its constitution and morphology.

For microstructural simulation, the chemical reaction was not considered during the impact process. Understanding the initiation of reaction by establishing certain reaction conditions and incorporating the new compound at determined stages would be useful.

Other polymeric materials with simple structures or containing fluorine atoms, e.g., PE, PVDF, PFA, FEP, etc., also need to be tested under high strain rates with or without

the presence of reactive metals in order to investigate the dynamic behavior of polymers with simple structures. Such structures should lead to a understanding of the mechanisms of impact-initiated chemical reactions between the polymer / reactive metal system.

As one of the most important material parameters under high strain rate compression, the EOS of PTFE 7A / Ti composite should be determined by the Hugoniot experiment with VISAR technology. The obtained P-V and U_s-U_p curves would also indicate the phase transformation / chemical reaction during high velocity impact.

APPENDIX A

GENERATE CONSTITUTIVE DATA SHEET

This chapter shows the *Matlab* code for generating constitutive data sheet for the PTFE 7A / Ti composite and Ti, which were used to incorporate into *Abaqus* software for simulation purpose.

A.1 Data Fitting of Modified Johnson-Cook Model for Instron and SHPB Test

The SHPB and Instron test data at 2500 and 0.01 s^{-1} were fitted with the modified Johnson-Cook model by using the *lsqcurvefit* function in *Matlab*.

A.1.1 Data Fitting Code of Modified Johnson-Cook Model for the SHPB Test

```
>>load('SHPB_2500.txt');
>>y=SHPB_2500(1:506);
>>x=SHPB_2500(507:(507+505));
>>initialconditions=[100000000 5000000000 1.5 450];
>>[newparameters1,error1]=lsqcurvefit(@mypolycurveSHPB,initialconditions,x,y);
>>y1=mypolycurveSHPB(newparameters1,x);
>>options=optimset('lsqcurvefit');
>>options.MaxFunEvals=500;
>>lb=[1000000 1000000 0.1 298];
>>ub=[1000000000 10000000000 10 593];
>>[newparameters2,error2]=lsqcurvefit(@mypolycurveSHPB,initialconditions,x,y,lb,ub,
options);
```

```
>>y2=mypolycurveSHPB(newparameters2,x);
>>options=optimset('lsqcurvefit');
>>options.MaxFunEvals=10000;
>>lb=[1000000 2000000 0.1 298];
>>ub=[1000000000 20000000000 10 593];
>>[newparameters3,error3]=lsqcurvefit(@mypolycurveSHPB,initialconditions,x,y,lb,ub,
options);
>>y3=mypolycurveSHPB(newparameters3,x);
>>figure
>>scatter(x,y)
>>hold
>>plot(x,y1,'r')
>>plot(x,y2,'g')
>>plot(x,y3,'b')
```

A.1.1 Data Fitting Code of Modified Johnson-Cook Model for the Instron Test

```
>>load('Instron_001.txt')
>>y=Instron_001(1:27);
>>x=Instron_001(28:(28+26));
>>initialconditions=[20000000 50000000 0.7];
>>options=optimset('lsqcurvefit');
>>options.MaxFunEvals=500;
>>lb=[1000000 1000000 0.1];
>>ub=[1000000000 10000000000 10];
>>[newparameters1,error1]=lsqcurvefit(@mypolycurveInstron,initialconditions,x,y,lb,ub
,options);
>>y1=mypolycurveInstron(newparameters1,x);
>>options=optimset('lsqcurvefit');
>>options.MaxFunEvals=10000;
```

```
>>[newparameters2,error2]=lsqcurvefit(@mypolycurveInstron,initialconditions,x,y,lb,ub
,options);
>>y2=mypolycurveInstron(newparameters2,x);
>>figure
>>scatter(x,y)
>>hold
>>plot(x,y1,'r')
>>plot(x,y2,'g')
```

A.2 Generate Stress-Strain-Strain Rate Planes

The stress-strain-strain rate data sheet for the PTFE 7A / Ti composite and Ti were generated based on the constitutive model built by fitting in the modified Johnson-Cook model for the PTFE 7A / Ti composite, and literature study on the constitutive relationship describing by the Zerilli-Armstrong model for Ti [52].

A.2.1 Stress-Strain-Strain Rate Plane for the PTFE 7A / Ti Composite

```
>>e=[0,1,10,100,500,1000,4000,8000,10000,20000,30000,40000,50000,60000,70000,80
000,90000,100000];
>>sp=[0:0.01:0.8];
>>for n=1:length(e)
>>for m=1:length(sp)
>>A(n,m)=17.61+9.673*asinh(e(n)/2);
>>N(n,m)=0.469+0.799*asinh(e(n)/2);
>>B(n,m)=18.25*2.29^N(n,m);
>>phi(n,m)=(1/(2840*768.6*(593-
298)))*(A(n,m)*sp(m)+(B(n,m)/(N(n,m)+1))*sp(m)^(N(n,m)+1));
>>s(n,m)=(A(n,m)+B(n,m)*sp(m)^N(n,m))*exp(-phi(n,m));
```

```
>>end
>>end
>>[x,y]=meshgrid(sp,e);
>>mesh(x,y,s)
>>st=s';
>>stress=st(:);
>>ssp=repmat(sp,length(e),1);
>>sssp=ssp'
>>strain=sssp(:);
>>for m=1:length(e);
>>for n=1:length(sp);
>>p=n+length(sp)*(m-1);
>>strainrate(p)=e(m);
>>end
>>end
>>srate=strainrate'
>>data=[stress,strain,srate]
>>save('data_1.xls', 'stress','-ASCII','-double','-tabs')
>>save('data_2.xls', 'strain','-ASCII','-double','-tabs')
>>save('data_3.xls', 'srate','-ASCII','-double','-tabs')
```

A.2.1 Stress-Strain-Strain Rate Plane for Ti

```
>>e=[0,1,10,100,500,1000,4000,8000,10000,40000,80000,100000]
>>sp=[0:0.01:0.8];
>>for n=1:length(e)
>>for m=1:length(sp)
>>b(n,m)=0.0024-0.00017*log(e(n));
>>st(n,m)=54+1100*exp(-b(n,m)*298)+300*sp(m)^0.5;
>>if st(n,m)>1050
>>s(n,m)=st(n,m)+700
```

```
>>else
>>s(n,m)=st(n,m)
>>end
>>end
>>end
>>[x,y]=meshgrid(sp,e);
>>mesh(x,y,s)
>>st=s';
>>stress=st(:);
>>ssp=repmat(sp,length(e),1);
>>sssp=ssp'
>>strain=sssp(:);
>>for m=1:length(e);
>>for n=1:length(sp);
>>p=n+length(sp)*(m-1);
>>strainrate(p)=e(m);
>>end
>>end
>>srate=strainrate'
>>data=[stress,strain,srate]
>>save('data_1.xls', 'stress','-ASCII','-double','-tabs')
>>save('data_2.xls', 'strain','-ASCII','-double','-tabs')
>>save('data_3.xls', 'srate','-ASCII','-double','-tabs')
```

APPENDIX B

ABAQUS EXPLICIT PROGRAM

B.1 Overview

Abaqus is a powerful suite of software for FEA and computer-aided engineering. It has been widely used in the field of automotive, aerospace and industrial products industries to solve complicated non-linear physical problems. Due to its wide material modeling and multiphysics capability, *Abaqus* is also popular in academic research to study a wide range of materials, e.g., metal, rubber, concrete, composite and general polymeric materials in terms of their structural properties, thermal conduction, vibration and acoustic problems, rock mechanics, etc.

Abaqus consists of three separate stages to deal with any FEA problems: pre-processing (modeling) by *Abaqus* / *CAE* or other products; evaluation and simulation by *Abaqus* / *Standard* or *Abaqus* / *Explicit*; and post-processing (visualization) by *Abaqus* / *CAE* or other products. The two main solver modules – *Abaqus / Standard* and *Abaqus / Explicit* are designed for different FEA situations. The former one is a general analysis module for a variety of linear and non-linear problems, like statics, dynamics, thermal study and electro responses; the latter one uses "central difference explicit time integration method" to get direct solution from equations instead of iteration in implicit algorithm, applicable to transient or instantaneous situation, like high-velocity impact or explosion.

Since the dynamic study of PTFE 7A / Ti composite in this thesis was in the time scale of tens of microseconds, *Abaqus / Explicit* program was applied for the Taylor impact simulation. The general procedures for modeling and setting up will be discussed in B.2.

B.2 Procedures

The finite element dynamic simulation of the Taylor impact test by *Abaqus Explicit* program followed the procedures as generalized below:

1. Create parts

Create the geometry of sample and anvil in the **Part Module**. Since the geometry of the whole setup is axisymmetric, only half of the sample was drawn in order to avoid the "stress hole" in the center of the impact surface. The sample was three dimensional deformable solid, and the anvil was three dimensonal analytical rigid shell with reference point in the middle of it.

2. Assign material properties

Input material properties for each material type in the **Property Module**; then create sections for each material type; finally assign the material properties into corresponding sections.

3. Assemble parts

Assemble all parts together in the **Assembly Module**. Create essential sets / surfaces which will be used in later steps.

4. Mesh parts

Mesh each part in the **Mesh Module**. Select global and edge seed sizes and mesh type appropriately, then create mesh for each part. To improve the mesh property of composite sample and simulation results, set the kinematic split as “Orthogonal”, hourglass control as “Enhanced”, and element deletion as “Yes”.

5. Create steps

Create analysis step after the default initial step in the **Step Module**. Set the simulation time period (0.00006) and increment size (2E-008) in this part; set the ALE adaptive mesh options in terms of frequency (set as 1) and remeshing sweeps per increment (set as 10) for keeping the mesh property as simulation goes on; set the field output and history output parameters to visualize the expected output results after simulation, and the interval option for output request was set based on the image interval (the image interval equals to exposure time plus interval time, so the interval option was set to the value equal to the time period set in the step dividing the image interval).

6. Interaction

Create interaction property and interaction pairs in the **Interaction Module**. Define interaction type as surface-to-surface contact, and select the first surface (master surface) and second surface (slave surface) pair as encountered in the simulation process, e.g., in this case, the anvil / sample surface pair needs to be created. The steps in which the interactions will be identified also need to be specified.

7. Boundary conditions and predefined fields

Set the boundary conditions and initial conditions in the **Load Module**. In this case, the anvil analytical shell was defined as a fixed boundary condition in the "Displacement / Rotation" type with all velocities / rotational velocities set as zero; the vertical central surface of sample was defined as "Symmetry / Antisymmetry / Encastre" type with velocity in z-direction, rotational velocities of x and y-direction set as zero; the initial temperature of the whole system was set as room temperature 298 K, and the initial velocity in y-direction of sample was set as value of the impact velocity.

8. Job

Create and submit job in the **Job Module** for simulation.

9. Visualization

Analyze and plot the simulation data in the **Visualization Module**.

APPENDIX C

PTFE 7A / TI INTERFACES DEFINITION IN *MATLAB*

The conversion of SEM image with RGB format into binary image with coordinate information for each node requires massive image processing. Based on the language of matrix and array, *Matlab* software possesses an unique advantage for image processing. In this chapter, the basics of the two dimensional image processing by using *Matlab* will be briefly introduced. The method to define outlines for each component region will be discussed, and the *Matlab* code to extract interfaces will also be presented here.

C.1 Two Dimensional Image Processing by Using Matlab

A two dimensional binary image with two components could be read in *Matlab* as a matrix with "1" denoting one component and "0" denoting the other. The coordinate of each element in the matrix represents the coordinate position of the center in each pixel. As represented in Figure C.1, suppose that the circle element refers to Ti particle and the triangle element refers PTFE 7A particle, then the matrix coordinate of each element equals to the center position of each pixel, and the corresponding four nodes for each pixel element could be obtained too.

Having all of the coordinate information for each pixel element and its four nodes, it will be of great importance to identify the interfaces between PTFE 7A regions and Ti regions in order to simulate their microstructrual deformation behavior. The basic idea to

extract those boundary nodes was to remove all of the inside nodes of certain PTFE 7A or Ti region. Take Figure C.1 for example, the interface between PTFE 7A and Ti was delineated in bold green line. The only difference between the interface nodes and the internal nodes is that the internal nodes are shared with neighbor elements four times. The *Matlab* code to eliminate internal nodes and obtain the outline for each component region will be presented in the next section.

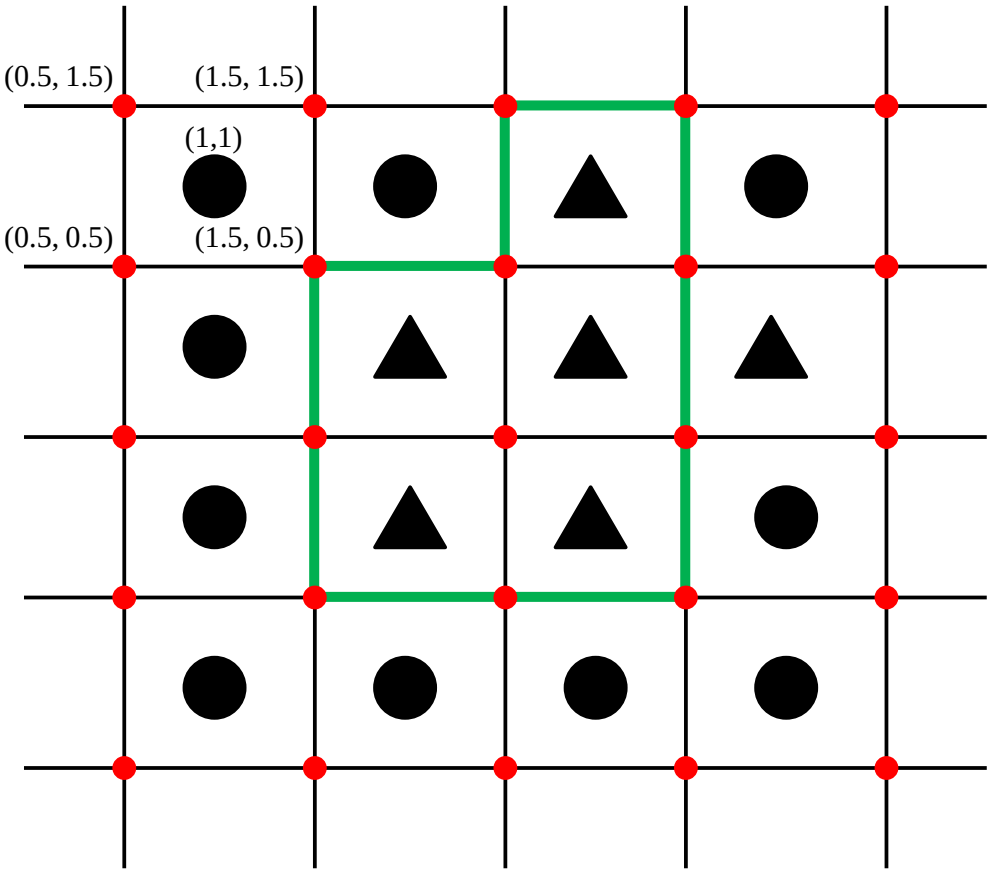

Figure C.1. The schematic diagram of binary image and the relation between pixel coordinate and node coordinate

C.2 The Matlab Code to Extract Interfaces Nodes

```
% Read the pixel information from binary image
>>A=imread('Aggregated_Binary image_Corrected.tif');
>>size(A);
%  Label all the objects (8 connected) in sequence
>>I=bwlabel(A);
%  An overall information for each connected component in I
>>B=regionprops(I,'PixelList');
%  Give the location of all pixels of B(1), object one
>>C=B(1).PixelList;
% Find four corner coordinates for each pixel in object one
>>for i=1:length(C)
>>for j=1:2
>>c1(i,j)=C(i,j)+0.5;
>>c2(i,j)=C(i,j)-0.5;
>>c3(i,j)=C(i,j)+(-1)^j*0.5;
>>c4(i,j)=C(i,j)+(-1)^(j+1)*0.5;
>>end
>>end
>>c5=[c1;c2;c3;c4];
% Find repeating rows and then rows repeating 4 times
>> [c,m,n]=unique(c5,'rows');
>>t=1;
>>for i=1:length(m)
>>ss=sum(ismember(c5,c5(m(i),:),'rows'));
>>if ss==4
>>s(t,:)=c5(m(i),:);
>>t=t+1;
>>end
>>end
```

```
% Delete rows repeating 4 times
>>c6=c5;
>>for i=1:(t-1)
>>for j=1:4
>> [int,ia,ib]=intersect(s(i,:),c6,'rows');
>>c6(ib,:)=[];
>>end
>>end
% Make other repeating rows identity
>>c7=unique(c6,'rows');
% Plot boundary lines to check
>>imshow(A)
>>hold on
>>scatter(c7(:,1),c7(:,2),3,'filled')
% Add sequence number in front of each row
>>for i=1:length(c7)
>>c8(i)=i;
>>end
>>c8=[c8' c7];
% Add comma
>>fid=fopen('T1.txt','wt');
>>fprintf(fid,'%f,%f,%f\n',c8');
>>fclose(fid);
```

REFERENCES

1. *An introduction to energetic materials*. 2005.

2. Eakins, D.E. and N.N. Thadhani, *Shock compression of reactive powder mixtures.* International Materials Reviews, 2009. **54**(4): p. 181-213.

3. Lee, J.H. and N.N. Thadhani, *X-ray diffraction and mechanical property studies of TiCx synthesized by shock-assisted reaction sintering.* Journal of Materials Processing Technology, 1999. **85**(1-3): p. 83-86.

4. Lee, J.H. and N.N. Thadhani, *Enhanced solid-state reaction kinetics of shock-compressed titanium and carbon powder mixtures.* Journal of Materials Research, 1998. **13**(11): p. 3160-3173.

5. Lee, J.H. and N.N. Thadhani, *Diffusion controlled process in shock-densified Ti+0.95C green compacts.* Metals and Materials-Korea, 1998. **4**(4): p. 676-679.

6. Lee, J.H. and N.N. Thadhani, *Reaction synthesis mechanism in dynamically densified Ti+C powder compacts.* Scripta Materialia, 1997. **37**(12): p. 1979-1985.

7. Lee, J.H., N.N. Thadhani, and H.A. Grebe, *Reaction sintering of shock-compressed Ti+C powder mixtures.* Metallurgical and Materials Transactions a-Physical Metallurgy and Materials Science, 1996. **27**(7): p. 1749-1759.

8. Eakins, D.E. and N.N. Thadhani, *Mesoscale simulation of the configuration-dependent shock-compression response of Ni plus Al powder mixtures.* Acta Materialia, 2008. **56**(7): p. 1496-1510.

9. Eakins, D. and N.N. Thadhani, *Shock-induced reaction in a flake nickel plus spherical aluminum powder mixture.* Journal of Applied Physics, 2006. **100**(11).

10. Thadhani, N.N., et al., *Shock-induced reaction synthesis (SRS) of nickel aluminides.* Journal of Materials Research, 1992. **7**(5): p. 1063-1075.

11. Jordan, J.L., et al., *High pressure behavior of titanium-silicon carbide (Ti3SiC2).* Journal of Applied Physics, 2003. **93**(12): p. 9639-9643.

12. Namjoshi, S.A. and N.N. Thadhani, *Modeling the reaction synthesis of shock-densified titanium-silicon powder mixture compacts.* Metallurgical and Materials

Transactions B-Process Metallurgy and Materials Processing Science, 2000. **31**(2): p. 307-316.

13. Thadhani, N.N., et al., *Shock-induced chemical reactions in titanium-silicon powder mixtures of different morphologies: Time-resolved pressure measurements and materials analysis.* Journal of Applied Physics, 1997. **82**(3): p. 1113-1128.

14. Raftenberg, M.N., W. Mock, and G.C. Kirby, *Modeling the impact deformation of rods of a pressed PTFE/Al composite mixture.* International Journal of Impact Engineering, 2008. **35**(12): p. 1735-1744.

15. Mock, J.W. and W.H. Holt, *Impact initiation of rods of pressed polytetrafluoroethylene (PTFE) and aluminum powders.* AIP Conference Proceedings, 2006. **845**(1): p. 1097-1100.

16. Lee, R.J., et al., *Reactive materials studies.* AIP Conference Proceedings, 2006. **845**(1): p. 169-174.

17. Licheri, R., R. Orru, and G.C. Cao, *Chemically-activated combustion synthesis of TiC-Ti composites.* Materials Science and Engineering a-Structural Materials Properties Microstructure and Processing, 2004. **367**(1-2): p. 185-197.

18. Millett, J.C.F., N.K. Bourne, and G.S. Stevens, *Taylor impact of polyether ether ketone.* International Journal of Impact Engineering, 2006. **32**(7): p. 1086-1094.

19. Meyers, M.A., *Dynamic behavior of materials*. 1994: John Wiley & Sons, Inc.

20. Thadhani, N.N., *Shock-induced and shock-assisted solid-state chemical-reactions in powder mixtures.* Journal of Applied Physics, 1994. **76**(4): p. 2129-2138.

21. Carter, W.J. and S.P. Marsh, *Hugoniot equation of state of polymers*. 1995, Los Alamos National Laboratory: New Mexico.

22. Decarli, P.S. and J.C. Jamieson, *Formation of diamond by explosive shock.* Science, 1961. **133**(346): p. 1821-+.

23. Carrington, W.E. and M.L.V. Gayler, *The use of flat-ended projectiles for determining dynamic yield stress .3. changes in microstructure caused by deformation under impact at high-striking velocities.* Proceedings of the Royal Society of London Series a-Mathematical and Physical Sciences, 1948. **194**(1038): p. 323-331.

24. Whiffin, A.C., *The use of flat-ended projectiles for determining dynamic yield stress .2. tests on various metallic materials.* Proceedings of the Royal Society of London Series a-Mathematical and Physical Sciences, 1948. **194**(1038): p. 300-322.

25. Taylor, G., *The use of flat-ended projectiles for determining dynamic yield stress .1. theoretical considerations.* Proceedings of the Royal Society of London Series a-Mathematical and Physical Sciences, 1948. **194**(1038): p. 289-299.

26. Hutchings, I.M., *Estimation of yield stress in polymers at high strain-rates using g. i. Taylors impact technique.* Journal of the Mechanics and Physics of Solids, 1978. **26**(5): p. 289-301.

27. House, J.W., et al., *Film data reduction from Taylor impact tests.* Journal of Strain Analysis for Engineering Design, 1999. **34**(5): p. 337-345.

28. Field, J.E., et al., *Experimental methods at high-rates of strain.* Journal De Physique IV, 1994. **4**(C8): p. 3-22.

29. Walley, S.M., et al., *The rapid deformation behaviour of various polymers.* Journal De Physique III, 1991. **1**: p. 1889-1925.

30. Sivoiur, C.R., et al., *Mechanical behaviour of polymers at high rates of strain.* Journal De Physique IV, 2006. **134**: p. 949-955.

31. Sivoiur, C.R., et al., *The high strain rate compressive behaviour of polyercarbonate and polyvinylidene difluoride.* Polymer, 2005. **46**: p. 12546-12555.

32. Fernandez, J.O. and G.M. Swallowe, *Crystallisation of PET with strain, strain rate and temperature.* Journal of Material Science, 2000. **35**.

33. Swallowe, G.M., J.O. Fernandez, and S. Hamdan, *Crystallinity increases in semi crystalline polymers during high rate testing.* Journal De Physique IV, 1997. **7**: p. C3-453-458.

34. Richeton, J., et al., *Influence of temperature and strain rate on the mechanical behavior of three amorphous polymers: Characterization and modeling of the compressive yield stress.* International Journal of Solids and Structures, 2006. **43**: p. 2318-2334.

35. Al-Maliky, N., et al., *Drops in the flow stress of semi-crystalline polymers at very high rates of strain.* Journal of Material Science Letters, 1998. **17**: p. 1141-1143.

36. Briscoe, B.J. and I.M. Hutchings, *Impact yielding of high density polyethylene.* Polymer, 1976. **17**: p. 1099-1102.

37. Briscoe, B.J. and R.W. Nosker, *The influence of interfacial friction on the deformation of high density polyethylenen in a split Hopkinson pressure bar.* Wear, 1984. **95**: p. 241-262.

38. Briscoe, B.J. and R.W. Nosker, *The flow-stress of high-density polyethylene at high-rates of strain.* Polymer Communications, 1985. **26**: p. 307-308.

39. Ree, T. and H. Eyring, *Theory of non-Newtonian flow. I. Solid plastic system.* Journal of Applied Physics, 1955. **26**(7): p. 793-800.

40. Bauwens, J.C., *Relation between compression yield stress and mechanical loss peak of bisphenol-a-polycarbonate in beta-transition range.* Journal of Materials Science, 1972. **7**(5): p. 577-&.

41. Richeton, J., et al., *A formulation of the cooperative model for the yield stress of amorphous polymers for a wide range of strain rates and temperatures.* Polymer, 2005. **46**: p. 6035-6043.

42. Rietsch, F. and B. Bouette, *The compression yield behaviour of polycarbonate over a wide range of strain rates and temperatures.* European Polymer Journal, 1990. **26**(10): p. 1071-1075.

43. Xiao, C.D., J.Y. Jho, and A.F. Yee, *Correlation between the shear yielding behavior and secondary relaxation of bisphenol-a-polycarbonate and related copolymers.* Macromolecules, 1994. **27**: p. 2761-2768.

44. Spruiell, J.E., D.E. Mccord, and R.A. Beuerlein, *The effect of strain history on the crystallization beehavior of bulk poly(ethylene terephthalate).* Transactions of the Society of Rheology, 1972. **16**: p. 535-555.

45. Swallowe, G.M. and S.F. Lee, *A study of the mechanical properties of PMMA and PS at strain rates of 10^{-4} to 10^{3} over the temperature range 193-363 K.* Journal De Physique IV, 2003. **110**: p. 33-38.

46. Hamdan, S. and G.M. Swallowe, *The strain-rate and temperature dependence of the mechanical properties of polyetherketone and polyetheretherketone.* Journal of Material Science, 1996. **31**: p. 1415-1423.

47. Bancroft, D., E.L. Peterson, and S. Minshall, *Polymorphism of iron at high pressure.* Journal of Applied Physics, 1956. **27**(3): p. 291-298.

48. Riter, J.R., *Discussion of shock-induced graphite- wurtzite phase-transformation in BN and implications for stacking in graphitic BN.* Journal of Chemical Physics, 1973. **59**(3): p. 1538-1538.

49. Larson, D.B., *A shock-induced phase transformation in bismuth.* Journal of Applied Physics, 1967. **38**(4): p. 1541-&.

50. Duval, G.E. and R.A. Graham, *Phase-transitions under shock-wave loading.* Reviews of Modern Physics, 1977. **49**(3): p. 523-579.

51. Brown, E.N., et al., *A new strain path to inducing phase transitions in semi-crystalline polymers.* Polymer, 2007. **48**(9): p. 2531-2536.

52. Holt, W.H., et al., *Experimental and computational study of the impact deformation of titanium Taylor cylinder specimens.* Mechanics of Materials, 1994. **17**(2-3): p. 195-201.

53. Abovyan, L.S., et al., *The effect of degassing modes on the self-propagating reactions for the SiO2-Al-C system in the presence of reaction promoters.* Ceramics International, 2003. **29**(2): p. 175-182.

54. Huang, W., et al., *Influence of temperature and strain rate on deformation twinning of polycrystalline titanium.* The Chinese Journal of Nonferrous Metals, 2008. **18**(8): p. 1440-1445.

55. Christman, D.R., et al., *Measurements of dynamic properties of materials*. 1972: General Motor Technical Center, Warren, MI, Februray.

56. Grebe, H.A. and N.N. Thadhani, *Influence of dynamic densification on microstructure and properties of reaction synthesized TiC ceramic.* Journal of Materials Synthesis and Processing, 1999. **7**(1): p. 49-61.

57. Lebrat, J.P. and A. Varma, *Self-propagating reactions in finite pellets - synthesis of titanium carbide.* Aiche Journal, 1993. **39**(10): p. 1732-1734.

58. Holt, J.B. and Z.A. Munir, *Combustion synthesis of titanium carbide: theory and experiment.* Journal of Materials Science, 1986. **21**: p. 251-250.

59. Armstrong, R.W., L. Ferranti, and N.N. Thadhani, *Elastic/plastic/cracking indentation behavior of hard materials.* International Journal of Refractory Metals & Hard Materials, 2006. **24**(1-2): p. 11-16.

60. Joshi, V.S., N.N. Thadhani, and R.A. Graham, *Mechanistic study of shock-induced solid-state chemistry in Ti-based and Ta-based carbide and boride systems*. High-Pressure Science and Technology - 1993, Pts 1 and 2, ed. S.C. Schmidt, et al. 1994. 1299-1302.

61. Thadhani, N.N., N. Chawla, and W. Kibbe, *Explosive shock-compression processing of titanium aluminide titanium diboride composites.* Journal of Materials Science, 1991. **26**(1): p. 232-240.

62. Chen, T., J.M. Hampikian, and N.N. Thadhani, *Synthesis and characterization of mechanically alloyed and shock-consolidated nanocrystalline NiAl intermetallic.* Acta Materialia, 1999. **47**(8): p. 2567-2579.

63. Ferreira, A., et al., *Dynamic compaction of titanium aluminides by explosively generated shock-waves - experimental and materials systems.* Metallurgical Transactions a-Physical Metallurgy and Materials Science, 1991. **22**(3): p. 685-695.

64. Bowden, D.M., et al., *Synthesis of novel aluminide-based materials.* Journal of Metals, 1988. **40**(9): p. 18-20.

65. Vandersall, K.S. and N.N. Thadhani, *Time-resolved measurements of the shock-compression response of Mo+2Si elemental powder mixtures.* Journal of Applied Physics, 2003. **94**(3): p. 1575-1583.

66. Deevi, S.C. and N.N. Thadhani, *Reaction synthesis of high-temperature silicides.* Materials Science and Engineering a-Structural Materials Properties Microstructure and Processing, 1995. **193**: p. 604-611.

67. Yu, L.H. and M.A. Meyers, *Shock synthesis and synthesis-assisted shock consolidation of silicides.* Journal of Materials Science, 1991. **26**(3): p. 601-611.

68. Eyring, H., *Viscosity, plasticity and diffusion as examples of absolute reaction rates.* Journal of Chemical Physics, 1936. **4**: p. 283-291.

69. Bauwensc.C, J.C. Bauwens, and G. Homes, *Temperature dependence of yield of polycarbonate in uniaxial compression and tensile tests.* Journal of Materials Science, 1972. **7**(2): p. 176-&.

70. Johnson, G.R. and W.H. Cook. *A constitutive model and data for metals subjected to large strains, high strain rates, and high temperatures*. in *Seventh International Symposium on Ballistics*. 1983.

71. Zerilli, F.J. and R.W. Armstrong, *Dislocation-mechanics-based constitutive relations for material dynamics calculations.* Journal of Applied Physics, 1987. **61**(5): p. 1816-1825.

72. Armstrong, R.W. and F.J. Zerilli, *Dislocation mechanics aspects of plastic instability and shear banding.* Mechanics of Materials, 1994. **17**(2-3): p. 319-327.

73. Zerilli, F.J. and R.W. Armstrong, *A constitutive equation for the dynamic deformation behavior of polymers.* Journal of Materials Science, 2007. **42**(12): p. 4562-4574.

74. Jordan, J.L., et al., *Compressive properties of extruded polytetrafluoroethylene.* Polymer, 2007. **48**(14): p. 4184-4195.

75. Mulliken, A.D. and M.C. Boyce, *Mechanics of the rate-dependent elastic-plastic deformation of glassy polymers from low to high strain rates.* International Journal of Solids and Structures, 2006. **43**: p. 1331-1356.

76. Ksiazczak, A., H. Boniuk, and S. Cudzilo, *Thermal decomposition of PTFE in the presence of silicon, calcium silicide, ferrosilicon and iron.* Journal of Thermal Analysis and Calorimetry, 2003. **74**(2): p. 569-574.

77. Rae, P.J. and D.M. Dattelbaum, *The properties of poly (tetrafluoroethylene) (PTFE) in compression.* Polymer, 2004. **45**(22): p. 7615-7625.

78. Sarva, S., A.D. Mulliken, and M.C. Boyce, *Mechanics of Taylor impact testing of polycarbonate.* International Journal of Solids and Structures, 2007. **44**: p. 2381-2400.

79. Shin, H.S., et al., *Deformation behavior of sleeved polymer core projectiles during Taylor impact*. Dymat 2009: 9th International Conference on the Mechanical and Physical Behaviour of Materials under Dynamic Loading, Vol 1. 2009. 655-661.

80. Ferranti, L. and N. Thadhani, *Dynamic mechanical behavior characterization of epoxy-cast Al+Fe2O3 thermite mixture composites.* Metallurgical and Materials Transactions a-Physical Metallurgy and Materials Science, 2007. **38A**(11): p. 2697-2715.

81. Martin, M., S. Hanagud, and N.N. Thadhani, *Mechanical behavior of nickel plus aluminum powder-reinforced epoxy composites.* Materials Science and Engineering a-Structural Materials Properties Microstructure and Processing, 2007. **443**(1-2): p. 209-218.

82. Eakins, D. and N.N. Thadhani, *Analysis of dynamic mechanical behavior in reverse Taylor anvil-on-rod impact tests.* International Journal of Impact Engineering, 2007. **34**(11): p. 1821-1834.

83. Bourne, N.K., et al., *Shock, release and Taylor impact of the semicrystalline thermoplastic polytetrafluoroethylene.* Journal of Applied Physics, 2008. **103**(7).

84. Brown, E.N., et al., *Soft recovery of polytetrafluoroethylene shocked through the crystalline phase II-III transition.* Journal of Applied Physics, 2007. **101**(2).

85. Rae, P.J., et al., *Pressure-induced phase change in poly(tetrafluoroethylene) at modest impact velocities.* Journal of Applied Physics, 2005. **98**(6).

86. Teller, E., *Speed of reactions at high pressures.* Journal of Chemical Physics, 1962. **36**(4): p. 901-&.

87. Eakins, D.E. and N.N. Thadhani, *The shock-densification behavior of three distinct Ni+Al powder mixtures.* Applied Physics Letters, 2008. **92**(11).